

**Performance Modeling and Efficiency Analysis for a
Piezohydraulic Pump with Active Valves**

by

Honghui Tan

Thesis submitted to the Faculty of the
Virginia Polytechnic Institute and State University
in partial fulfillment of the requirements for the degree of

Master of Science

in

Mechanical Engineering

Dr. Donald J. Leo
Dr. Harry H. Robertshaw
Dr. Clinton L. Dancey

November 2002

Blacksburg, Virginia

Keywords: Piezohydraulic actuation, fluid flow, power efficiency

Copyright 2002, Honghui Tan

Performance Modeling and Efficiency Analysis for a Piezohydraulic Pump with Active Valves

Honghui Tan, M.S.

Virginia Polytechnic Institute and State University, 2002

Advisor: Dr. Donald J. Leo

ABSTRACT

Piezoelectric actuation is an expanding field that makes use of piezoelectric material that have high power density as actuators. These actuation systems have the potential higher power density than the traditional servo motor technology.

However, due to tiny strain of the piezoelectric materials, displacement amplification mechanism should be incorporated into design for most commercial applications. Piezohydraulic actuation provides an ideal amplification that can achieve any combination of stroke and force, which is superior than most other amplification technologies. The concept of piezohydraulic actuation takes advantage of the high force capabilities that piezoceramics have and combines it with the operation at high frequencies, in order to achieve the hydraulic actuation of a system under a specified stroke and force.

In this research, a compact piezohydraulic pump with active valves has been developed, tested and characterized. Furthermore, theoretical models are developed based on different levels of approximation of the hydraulic fluid. The first model, which assumes an incompressible and inviscid fluid, provides us views of the basic features of piezohydraulic actuation. The second model which takes into account the viscosity of the fluid and the third model which takes into account both viscosity and compressibility of the fluid are then presented. Then, their simulation results are compared with experimental data, which shows the compressibility of the fluid is important to system performance. At last, a power and efficiency analysis based on experimental results is presented.

Contents

Abstract	ii
List of Tables	vi
List of Figures	vii
Chapter 1 Introduction	1
1.1 Motivation	1
1.2 Background	2
1.3 Literature Review	2
1.3.1 Piezoelectric Actuation	2
1.3.2 Piezohydraulic Actuation	4
1.3.3 Power efficiency of piezoelectric actuation	5
1.4 Objectives and Contribution	7
1.5 Approach	8
Chapter 2 Piezo-Hydraulic Actuation System	9
2.1 Introduction	9
2.2 The Four-Stage Operation Model	11
2.3 The Piezoceramic Stack Actuator	13
2.3.1 Piezoelectricity and Piezoceramic Stack	13
2.3.2 Electromechanical coupling of the piezoceramic stack	14
2.3.3 Power efficiency of a piezoceramic stack	17
2.4 Definition of Efficiency Metrics	19
2.5 The Hydraulic Unit	19
2.6 Effective Bulk Modulus of Fluid	21

2.7	Inviscid Flow in the Hydraulic System	22
2.8	Viscous Flow in the Hydraulic Unit	23
2.8.1	Energy Analysis for A Control Volume	24
2.8.2	Determination of Velocity Profile Coefficient α	27
2.8.3	Determination of Head Losses	30
2.9	Summary	34
Chapter 3 Model of Piezo-Hydraulic Actuation System		36
3.1	Introduction	36
3.2	The Incompressible Inviscid Fluid (IIF) Model	37
3.2.1	Four-Stage Operation	37
3.2.2	Work and Efficiency	41
3.2.3	Summary	45
3.3	The Incompressible Viscous Fluid (IVF) Model	46
3.3.1	Calculation of the Reynolds Number	46
3.3.2	Flow Equations	48
3.3.3	Summary	57
3.4	The Compressible Viscous Fluid (CVF) Model	57
3.4.1	Equations for The Exhaustion Stage	57
3.4.2	Equations for The Intake Stage	65
3.5	Summary	67
Chapter 4 Experimental Results And Simulations		68
4.1	Introduction	68
4.2	Experimental Setup	68
4.3	Bulk Modulus Measurement	70
4.4	Simulation Parameters	75
4.5	Single-ended Cylinder	75
4.5.1	Characteristics of Power Amplifier	75
4.5.2	Performance Measurements and Simulation	76
4.6	Double-ended Cylinder	91
4.6.1	Characteristics of Power Amplifier	91
4.6.2	Performance Measurements and Simulation	91

4.7	Power Efficiency Analysis	101
4.7.1	Power Efficiency Measurements	101
4.8	Summary	105
Chapter 5 Conclusions		106
5.1	recommendation and Future Work	108
Appendix A		110
Bibliography		122
Vita		125

List of Tables

3.1 Parameters of the system. 48

4.1 Energy and actuation efficiency at 100 Hz operating frequency. 104

List of Figures

1.1	Piezoceramic stack actuators[Physik Instrumente]	3
1.2	Piezoceramic sensors[PCB]	3
2.1	Diagram of a piezohydraulic pump	10
2.2	Diagram of four phases in one period of operation	11
2.3	Diagram of four phases in one period of operation	12
2.4	Piezoceramic materials	13
2.5	Force-displacement characteristic curve	16
2.6	Charge-voltage characteristic curve	16
2.7	System setup	20
2.8	Parts of the active valve assembly [Kinetic Ceramics]	21
2.9	Diagram of cross section of an active valve [Kinetic Ceramics]	21
2.10	Streamlines in flow through a duct	23
2.11	A control volume in the flow	25
2.12	Control volume for flow through a pipe	26
2.13	Velocity profile of flow through a pipe	26
2.14	Velocity profiles for laminar and turbulent flow in a pipe at $Re = 4 \times 10^3$ [Fox and McDonald (1978)]	28
2.15	Velocity profile for different value of power n	30
2.16	Moody diagram for fully developed flow in circular pipes [Tullis (1989)] . .	32
2.17	Loss coefficient for different entrance types. (a) Reentrant, $K = 0.8$, (b) sharp-edged, $K = 0.5$, (c) slightly rounded, $K = 0.2$, (d) well-rounded, $K =$ 0.04. [Munson and Young (1998)]	33
2.18	Loss factor of sudden expansion and contraction	34

3.1	Setup diagrams and parameters	38
3.2	Free body diagram of piston in the cylinder	39
3.3	Mechanical work of the stack and load	42
3.4	Efficiency of a single-ended cylinder	44
3.5	Diagram of fluid flow	47
3.6	Diagram of compression stage	49
3.7	Control volumes of the flow	51
3.8	Free body diagram of piston in the cylinder	54
3.9	Control volume in the intake stage	55
3.10	IVF Simulation at 100 Hz under 6.84 Kg load	57
3.11	Diagram of system used to develop CVF model.	58
3.12	Diagram of chamber for CVF model.	60
3.13	Diagram of hydraulic cylinder for CVF model.	62
3.14	Diagram of intake stage for CVF model.	66
3.15	CVF Simulation at 100 Hz under 6.84 Kg load	67
4.1	Experimental setup diagram for velocity measurement	69
4.2	Experiment setup	70
4.3	Components of stack unit	71
4.4	Closed chamber test setup	71
4.5	Force vs displacement	72
4.6	Peak pressure	73
4.7	Linearly fitted bulk modulus with pressure	73
4.8	Experimental and approximated force-displacement	73
4.9	Voltage at 100 Hz frequency under different loads	77
4.10	Current at 100 Hz frequency under different loads	78
4.11	Peak voltage for different frequency	79
4.12	Peak current for different frequency	79
4.13	Current and voltage model of input of stack	79
4.14	Performance measurements at 100 Hz under 0Kg load	81
4.15	Average measurements at 100 Hz under 0Kg load	82
4.16	Four stage timing at 100 Hz	82

4.17	Pressure in chamber in four stages at 100 Hz	82
4.18	Simulation results at 100 Hz under 0 Kg load	84
4.19	Simulation results at 200 Hz under 0 Kg load	85
4.20	Measurements compare of the single-ended cylinder at 50 Hz under 6.84 Kg load	86
4.21	Measurements compare of the single-ended cylinder at 50 Hz under 12.82 Kg load	86
4.22	Measurements compare of the single-ended cylinder at 50 Hz under 17.45 Kg load	87
4.23	Measurements compare of the single-ended cylinder at 100 Hz under 6.84 Kg load	87
4.24	Measurements compare of the single-ended cylinder at 100 Hz under 12.82 Kg load	88
4.25	Measurements compare of the single-ended cylinder at 100 Hz under 17.45 Kg load	88
4.26	Velocity comparison at 50 Hz	89
4.27	Power comparison at 50 Hz	89
4.28	Velocity comparison at 80 Hz	90
4.29	Power comparison at 80 Hz	90
4.30	Velocity compare at 100 Hz	90
4.31	Power compare at 100 Hz	90
4.32	Load displacement at 50 Hz	91
4.33	Load displacement at 100 Hz	91
4.34	Measurements of stack current at 200 Hz under no load	92
4.35	Measurements at 100V peak voltage under no load at 100 Hz	93
4.36	Measurements at 100V peak voltage under 17.452 Kg load at 100 Hz	93
4.37	Measurements at 100V peak voltage under no load at 200 Hz	94
4.38	Measurements at 100V peak voltage under 17.452 Kg load at 200 Hz	94
4.39	Measurements at 130V peak voltage under no load at 100 Hz	95
4.40	Velocity comparison at 100 V	97
4.41	Power comparison at 100 V	98
4.42	Velocity measurements at 130 V	99

4.43	Power comparison at 130 V	100
4.44	Output power at different operating frequency and load	101
4.45	Electrical power under different load	102
4.46	Electrical work and mechanical work without load and with light load . . .	103
4.47	Power measurements at 100 V excitation	105
4.48	Power measurements at 130 V excitation	105

Chapter 1

Introduction

A compact piezo-hydraulic pump with active valves is designed and characterized. Different models are presented to model the performance of the system based on different approximations of hydraulic fluid properties. The performance and power efficiency of the system is simulated and compared to experimental results.

1.1 Motivation

Hydraulic power systems have long been used by human-beings before the invention of electric motors. Hydraulic systems can provide a wide range of force and work reliably for long durations. However, by using hydraulic fluid as the media to transfer power, these hydraulic systems normally need to consider extra problems, such as sealing and wear, which results in more hardware and increases weight. Since the invention of the electric motor, many applications of hydraulic power systems have been replaced by servo-motor systems because they can generate power reliably at reduced weight and thus achieve higher power output per unit mass.

Piezoelectric materials have enjoyed a great level of study in the last ten years. They can generate force and displacement under electrical excitation. Because their bandwidth of operation is higher than traditional servo-motors, higher power can be achieved when operating in high frequencies. The high energy density of the piezoelectric materials can potentially lead to a higher energy density of the actuator than traditional servo-motor technology. However, the small achievable strain of piezoelectric materials keeps this technology from being adopted in many industry applications.

The focus of this study is to develop Piezo-hydraulic actuation systems that amplify the small displacement of the piezoceramic material while maintaining large forces. This technology transfers the high frequency, small stroke of the piezoelectric materials into desired frequency and velocity at the load. The central feature of the piezo-hydraulic pump is that the stroke and output force of system can be varied at different operation conditions which makes it more desirable than other amplification techniques, such as bending and lever amplification(Wise (1998), Kar et al. (1998)).

A piezo-hydraulic pump consists of a piezoceramic actuator, a hydraulic cylinder and valves to control the flow. Most of the researches have used passive valves, which are limited at low operation frequencies. In order to explore the broad bandwidth of the piezoelectric materials, a compact piezo-hydraulic pump with active valves that enable high frequency operation is designed, characterized and modeled. Different models are presented to model the performance of the system based on different approximations of hydraulic fluid properties. Power and efficiency of the pump is analyzed and compared with experimental data.

1.2 Background

Piezoceramics are one kind of piezoelectric materials that exhibit electromechanical coupling. When it is stressed by an external force, it generates an electric charge and voltage. Conversely, when an electric field applied to it, its dimensions change and mechanical force is generated. In general, there are two typical kinds of applications: sensors or actuators. For the former case, piezoelectric materials are used to give electric output resulted from mechanical input. On the other hand, they can be used in a number of actuator applications, including precision positioning, vibration suppression and meso scale actuator devices. Figure 1.1 and Figure 1.2 show some commercial piezoceramic actuators and sensors.

1.3 Literature Review

1.3.1 Piezoelectric Actuation

Due to the tiny strain of piezoelectric materials, many researches have been done in order to amplify the deflection of the materials. Some reliable and low cost piezoelectric



Figure 1.1: Piezoceramic stack actuators[Physik Instrumente]



Figure 1.2: Piezoceramic sensors[PCB]

actuators have been developed, including Unimorphs, Bimorphs, Rainbows, Thunder and patch actuators (Near (1996)). These kinds of actuators take advantage of the strain in the direction that perpendicular to the polarized direction of the piezoelectric materials. The force and deflection of various bimorph configurations has been studied thoroughly by C. P. Germano (1995). The typical performance ranges for bimorph actuators are displacement of less than 500 microns and force less than 2.5N. Rainbow actuators are produced by chemically reducing one side of a lead-containing piezoelectric ceramic at an elevated temperature. The resulted structure can exhibit large axial displacements due to the difference of thermal-expansion coefficients between the ceramic and reduced layers. G. H. Heartling (1994) reported a Rainbow actuator with typical displacement of less than 1000 microns and force less than 500N. The maximum mechanical power output is in the order of thousandth of Watt. Wise (1998) showed that there are strong similarities in the performance capabilities of RAINBOW and THUNDER actuators. The RAINBOW devices exhibited displacements that were 10-25% greater than those of comparable THUNDER actuators. The patch actuators utilize the high length-to-thickness ratio in order to increase the displacement. These actuators do amplify the stroke to the order of one millimeter by utilizing a lever-like mechanism, in the expense of reducing stiffness, but the stroke is still not enough for many applications.

Different from the above actuators, piezoelectric stacks take advantage of strain in

the polarized direction directly. Piezoelectric stacks can utilize the piezoelectricity most efficiently. Piezoelectric stacks consist of multiple piezoelectric ceramics and the total displacement of the stack is the sum of displacement of each layer. The piezoelectric stack can produce displacement proportional to the thickness, typically in the order of 100 microns and is as stiff as piezoelectric materials, which means it can generate large forces. Typical force generation is on the order of several thousand Newton for commercial stacks. Now several commercial piezoelectric stack actuators are available, some of which work in voltage of thousands of volts and some work in hundreds of volts.

Although the stack actuator can produce large force, the displacement is limited. Several researchers have focused at amplifying the displacement of the stack actuator. A piezoelectric stack actuator with a lever of ten times of displacement amplification was developed by Kar et al. (1998). Displacement of seven hundred microns and maximum of 200N force was achieved in that design. The limit of the lever amplification is the difficulty of manufacturing a lever with high stiffness and large amplification.

Another different approach is to use step and repeat actuators. This type of actuators converts the reciprocal motion of piezoelectric actuator into uni-directional motion. The piezoelectric actuator can produce only a limited displacement and work in each stroke, but due to the wide band property of piezoelectric materials, they can work in high frequency and then generate large displacement and work in a specific time. Inchworm motors designed by Bexell et al. (1994) use piezoelectric bimorph as actuator elements and quasi static positioning in combination with amplification to produce the rotation. Maximum operational frequency is 30Hz and maximum power is 6.8 mW are achieved. In these designs, the output power is at the order of 1 Watt, which is much lower than traditional motors.

1.3.2 Piezohydraulic Actuation

Piezo-hydraulic actuation is the concept that hydraulic fluid is used to transmit the power of the piezoelectric actuators. Hydraulic fluid is used to fill the gap between the large displacement desired and small displacement of piezoelectric materials.

In Gerlach and Wurmus (1995), a piezoelectrically driven micropump of the reciprocating type is developed. In this design a pump pressures of up to 7kPa and upper frequency limit of 10 Khz is achieved. In Jung-Ho Park et al. (1999), a piezoelectric micropump with the size of 9-10mm that drove the bellow at its resonant frequency in order

to get large periodic volume change is fabricated and a maximum flow rate of $80 \text{ mm}^3/\text{s}$, maximum pumping pressure of 0.32 Mpa and maximum power of 8.7 mW are obtained at the driving frequency of 2 kHz. Smits (1990) developed a piezoelectric micropump that achieved pumping rate of 100ul/min at zero back pressure.

In order to increase the output power, a piezoceramic pump with passive valves was design by Mauck and Lynch (1999). The actuation system consists of an outlet valve, an inlet valve, a reservoir, an output cylinder and a 4-way valve to control the flow. In this design, a dynamic pressure of 1000 psi and a flow rate of 45 ccm has been achieved in low frequency operation. The performance decreases as working frequency increases to 10Hz above. Another piezohydraulic pump was developed by Nasser and Leo (2000a). In this design, the 4-way valve and the hydraulic accumulator are not needed, and thus the system is more compact. Different from the design of Mauck and Lynch (1999), solenoid valves are used to control the timing in order to optimize performance. In this design, the work frequency is limited to the transition of the solenoid valves. A maximum working frequency of 10 Hz was reported, which is much lower than the maximum operating frequency of piezoceramic stack. Sirohi and Chopra (2002) developed a system with smaller pump with passive valves that make it possible to run into kilo Hertz range. Their results also show that the transition of the valve could limit the performance of the system in high frequency operations.

1.3.3 Power efficiency of piezoelectric actuation

Power density and efficiency are two important considerations when evaluating actuation systems. Power density is the output power divided by mass of the actuator. Efficiency of actuator is the output power divided by input power of the actuator system.

One fundamental advantage of piezoelectric materials over other transducers of actuation, such as motors and shakers, is the high specific power density. Specific power density on the order of 50 to 100 KW/kg is achievable by driving the piezoelectric actuator in the order of kHz frequency range. The electro-mechanical coupling coefficient, which denotes the ratio of output mechanical power to the input electrical power, also named efficiency, can be as much as 0.5. Electro-mechanical coupling coefficients as high as 0.8 are achievable in new single-crystal piezoelectric materials. The power density and conversion efficiency of piezoelectric actuators are dependent of various working conditions, such as pre load, load,

temperature and driving frequency.

Several researches have been involved with the analysis the efficiency of system with piezoceramic actuators. Based on the comparative tests on five different piezoelectric stack, Mitrovic et al. (1994) showed strong dependence of both elastic and piezoelectric properties on the operation conditions (mechanical and electrical). Young's modulus changes significantly as a function of pre load and then results in the change of the equivalent stiffness of the stack, which will then change the energy conversion efficiency at a specific load. It is observed that piezoelectric coefficients and the energy density delivered by the actuator initially increase upon the application of mechanical compressive stress. But applying much higher pre load has the adverse effect. Optimum pre load between 4-6ksi is concluded for most of the five tested stacks.

Giurgiutiu et al. (1994) showed that the maximum energy output is achieved when the stiffness of the load and stiffness of the actuator are matched. He also pointed out that maximum efficiency and the efficiency for maximum energy output is different, which means matched stiffness does not correspond with maximum efficiency.

Due to the limited stroke length of the raw piezoelectric materials, mechanical amplification is usually added into piezoelectric actuators, which decreases the power density of the raw material. Many researches have focused at developing mechanical amplifications in favor of power density and efficiency.

On the basis of a general model of piezoelectric materials with mechanical lever, Paine and Chaudhry (1996) showed that mechanical amplification techniques may cause a 60-80% reduction in the energy density as compared to the bare materials. Different lever material like steel, aluminum and titanium are compared in terms of overall power density and it indicated that a maximum energy density ratio of 37% is all that can be expected for the above materials.

Taking into account the elasticity of the lever support and amplification elasticity, Giurgiutiu and Rogers (Sep. 1997) showed that when using a mechanical lever to amplify the displacement of the piezoelectric materials, support stiffness of the lever have more significant influence with the overall stiffness than lever stiffness due to the amplification effect of the lever. Also in the research, a test set up was build and predicted behavior is observed. It mentions that due to less than ideal conditions the performance loss also became apparent.

In Nasser and Leo (2000b), based on a quasi static analysis of incompressible and inviscid flow of a piezohydraulic pump, efficiency metric was defined and evaluated. It is showed that maximal efficiency of hydraulic fluid is much higher than compressible gas, which means the compressibility of the work fluid would greatly influence the actuation efficiency. In his work, the mechanical efficiency and electrical efficiency was defined as the ratio of net power to peak power and because no energy losses was considered in the model, thus the defined efficiency can not be used to actually predict the power efficiency of system.

Although the piezoelectric actuation has been studied for a long time, there are only a few that focused at the concept of piezohydraulic actuation. At present, in most piezohydraulic actuation systems, passive valve as check valves and servo valves are used. Their results show the system performance drops fast at high frequency operation due to the slow transition of valves. The motivation of this design is to design a piezohydraulic pump with active valves which can operate at higher frequency by making use of the broad bandwidth of piezoelectric material. It is important to test the system in various operation conditions in order to optimize performance. However, this work is very timing and effort consuming. Thus theoretical models that can predict the system performance are favored. Nasser and Leo (2000b) studied the efficiency of piezohydraulic actuation by a quasi-static model that assumes an incompressible and inviscid fluid. It can not predict the dynamics of the system which becomes more obvious for higher frequency operations. The motivation of this study is to develop models that can represent the real compressible and viscous fluid and predict the dynamic characteristics of the system performance.

1.4 Objectives and Contribution

The objective of this research is to develop a piezo-hydraulic actuation system with active valves and model the actuation system for optimization.

In this work, the following major contributions are made:

- A compact piezo-hydraulic pump with active valves is developed and then tested and characterized.
- A linear bulk modulus to pre-pressure model is verified experimentally and is incorporated in the model simulations.

- Three models based on different approximation of fluid are presented and compared with experimental data. Without run into complex dynamic model, the presented CVF model which takes into account the compressibility and viscosity of fluid is very consistent with the experimental data. The other two model, though less accurate, can predict the system performance and basic features at less computation effort.
- Power and efficiency of the actuation system is analyzed. Efficiency dependence upon load is experimentally verified.

1.5 Approach

Chapter 2 is an introduction to the piezohydraulic system. The electromechanical coupling of the stack is modeled based on the constitutive law of the piezoceramic materials. The energy equations for a viscous flow in the hydraulic system is discussed based on the first principle of thermodynamics. Then the velocity profile and head losses of the flow are determined for both laminar and turbulent flows.

Chapter 3 introduces theoretical model to analyze the fluid system based on a four-stage operation model based on the stack model and energy equations obtained in the previous chapter. First an incompressible and inviscid model is analyzed and results are discussed. Then, a quasi-static compressible and viscous flow model is developed.

Chapter 4 is devoted to the experimental and simulated results with both a single ended and a double ended cylinder. The power and efficiencies of the system are analyzed and then optimization and tradeoffs are outlined.

Chapter 5 summarizes the conclusions, proposes future work and formulates the corresponding recommendation.

Chapter 2

Piezo-Hydraulic Actuation System

2.1 Introduction

This chapter is an introduction to the piezo-hydraulic system. The electrical system, mechanical system and hydraulic system are presented. The electrical system is coupled to the mechanical system by the piezoceramic stack and the mechanical system is coupled to the load by the hydraulic system. An electromechanical coupling model of the stack is presented. To model the hydraulic system that couples the load with the piezoceramic stack, the characteristics of the fluid are analyzed and modeled. First, the compressibility of the fluid is modeled. Then fluid flow in the hydraulic system is analyzed for both inviscid and viscous flows based on an energy analysis. The stack model and fluid model in this chapter will be integrated in the next chapter to model the performance of the whole system. The major topics of the chapter are:

- The four-stage operation model.
- The electro-mechanical coupling: piezoceramic stack model and efficiency analysis.
- The hydraulic system: the fluid flow which couples the stack with the load. Basic equation of fluid, Bernoulli equation and energy equation will be presented. The coefficient and terms in the energy equations will be determined.

Test Setup

The setup of the piezo-hydraulic pump is shown in Figure 2.1. Active valves made of piezoceramic stack actuators are adopted, which makes it possible to operate in high frequency

range and to control the timing of the valve in order to optimize the performance of the system. The active valves are incorporated in the pump and closely connected with the pumping chamber. The system can be divided into following sub-systems: the electrical system, electrical-mechanical coupling, hydraulic system and mechanical output system.

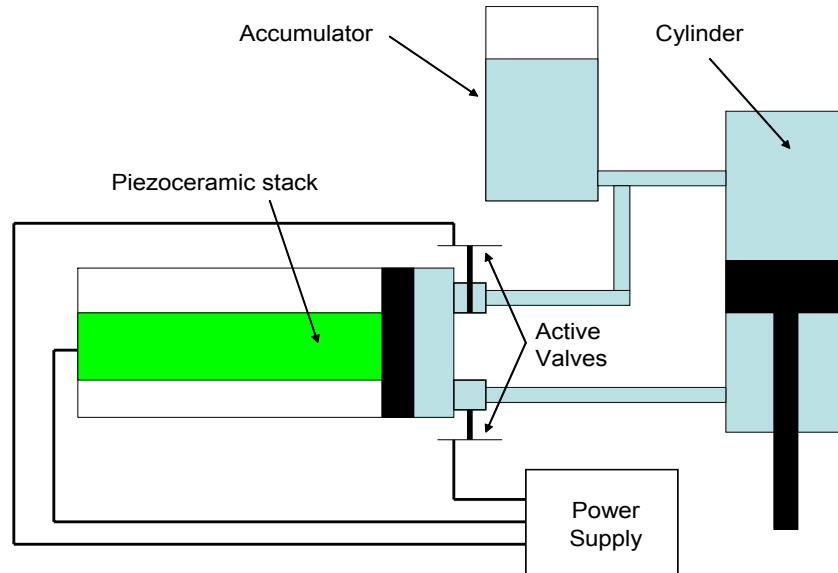


Figure 2.1: Diagram of a piezohydraulic pump

Figure 2.1 shows a simple diagram of the system with a single-ended cylinder. A system with a double-ended cylinder basically has the same configuration except that there is a rod in both ends of the cylinder such that the area in both end are equal. Systems with singled-ended and double-ended cylinder can give different performance. Power supplies are used to provide electrical power to the stack actuator and piezoceramic stack in both valves. Because the electrical-mechanical coupling of the piezoceramic stacks, they can generate displacement under the electrical excitation. By controlling the phase of the three electrical output signals, the motion of the stack and active valves are synchronized to generate fluid flow to drive the load through the hydraulic circuit. The cylinder translates the fluid flow into the motion of the load which is connected to the rod. It is noted that a vacuum pump is used to reduce the air entrapped in the working fluid, which improves the performance of the system. After the fluid is filled and pre-pressurized, the vacuum pump could be removed from the system.

2.2 The Four-Stage Operation Model

Nasser and Leo (2000b) first presented the four-stage operation model of a piezo-hydraulic system. We will use this model to simplify the operation of the system and the flow model in the next chapter will be based on this model.

The piezo-hydraulic actuation system works like a reciprocal pump except that the electrical motor is replaced with a piezoceramic stack actuator. The stack actuator moves in a reciprocal fashion under periodic electrical excitation. The valves open and close at the same frequency as the stack moves but are phased relative to the movement of the stack. Figure 2.2 shows the phases of stack signal and valves signal at 100 Hz operation frequency. The valves are closed when the signal is 0 volts and are open when the signal is at 10 V. The stack is at the full stroke when the signal is at 5 V.

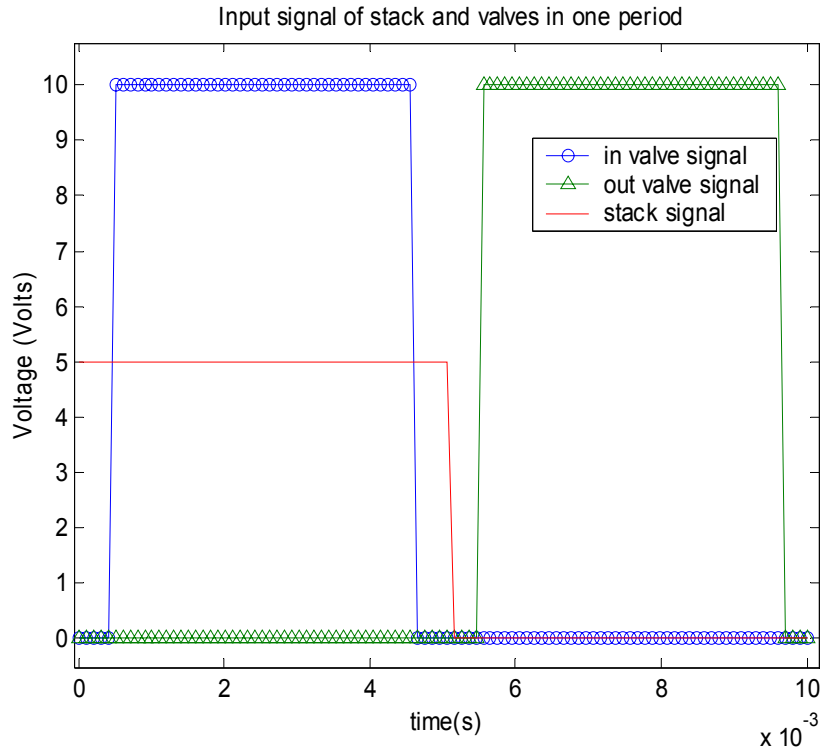


Figure 2.2: Diagram of four phases in one period of operation

The operation of the system can be divided into four stages: compression, exhaustion, expansion and intake. Figure 2.3 shows a diagram of action of piezoceramic stack and inlet and outlet valves in each stage.

At the beginning, the system is pre-pressurized to a uniform pressure of the ac-

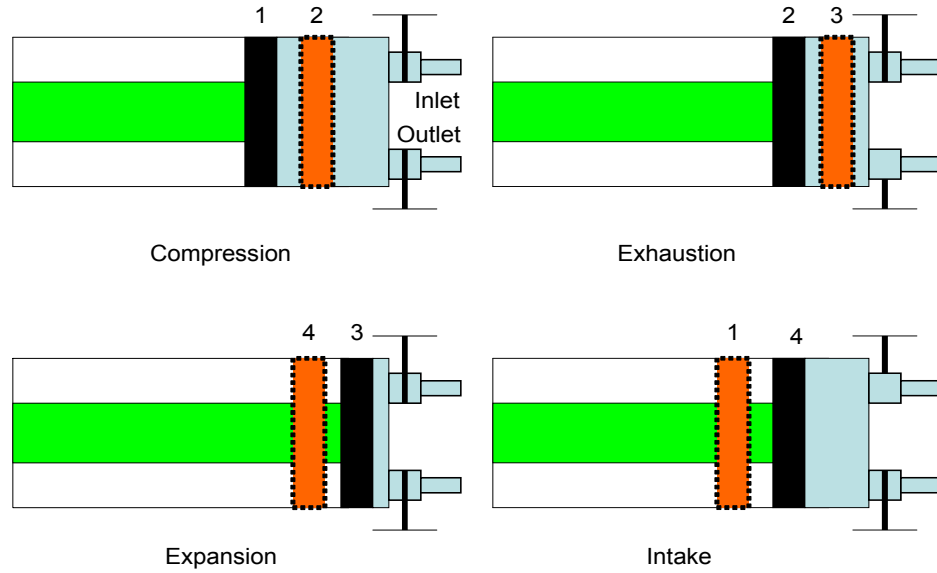


Figure 2.3: Diagram of four phases in one period of operation

cumulator pressure. The first stage is *compression* stage. With both valves closed, the piezoceramic stack pushes the hydraulic fluid in the closed pumping chamber from position 1 to position 2. The fluid is pressurized to a specific output pressure. Then the outlet valve opens and the stack continues to push the pressurized fluid out of the chamber to the position 3. At this exhaustion stage, the fluid is pushed through valves and pipings to drive the load. At the expansion stage, with both valves closed, the stack begins to retract from position 3 to position 4. The pressure in the pumping chamber is decreased. Then at the final intake stage, the inlet valve opens and the stack continues to retract from position 4 to position 1, which causes the fluid in the accumulator to flow into the pumping chamber. In this four stage model, it is noticed that only in exhaustion stage does the system do work to the load.

Not all the piezo-hydraulic system adopts the above four stage model. Some studies adopted a two stage actuation model which only consists of exhaustion stage and intake stage. In fact, the incorporation of the active valves in the system makes it possible to explore various of working fashions to optimize the performance of the system. This four stage model will be used later to model and analyze the power efficiency of the system.

2.3 The Piezoceramic Stack Actuator

The electromechanical coupling of a piezoceramic actuator is modeled and presented in the section. The energy losses in the piezoceramics are neglected, which predicts the upper bound of the performance. The electromechanical coupling model will be used in next chapter to develop the model the whole system.

2.3.1 Piezoelectricity and Piezoceramic Stack

When a piezoelectric element is subjected to mechanical stress, it generates electric charges and voltage associated with the charge. When it is stressed electrically by a voltage, its dimensions change. If its dimensions are fixed, a force is generated. Therefore piezoelectric materials are capable of acting either as a sensing or transmitting element, or both. Due to the small strain of piezoceramics, piezoceramic stacks that consist of many sheets of piezoceramic materials are designed and produced, which can generate larger deflection without sacrificing the force. Figure 2.4 shows a piezoceramic sheet and a stack that generates deflection under electrical excitation.

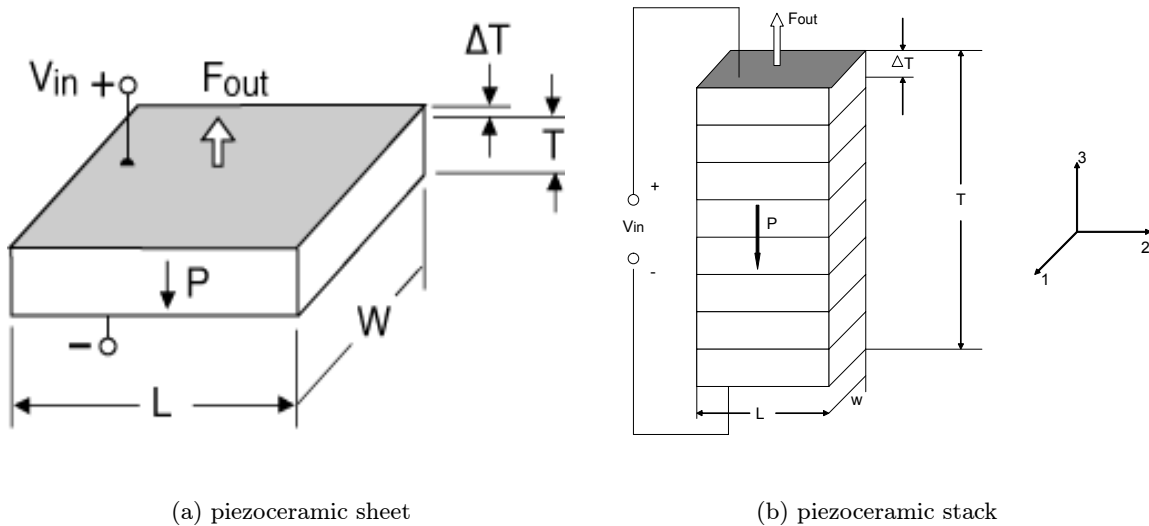


Figure 2.4: Piezoceramic materials

The relationships between the applied voltage and the resulting force depend on the piezoelectric properties of the ceramics, the direction of the applied electrical field and the shape and size of piezoceramics. As shown in Figure 2.4, the label \mathbf{P} represents the

polarization vector. Three axes, 1, 2 and 3, are used to identify different directions, with axis 3 to be parallel to the polarized direction of the piezoceramic material. Therefore, properties of piezoceramics usually use subscripts which indicate different directions. For example, the d_{33} strain constant represents the mechanical strain in the 3 direction produced by an electric field in the same direction and d_{31} represents mechanical strain in the 1 direction while the electric field still is in the 3 direction. By using two digit subscripts, it is possible to identify the relationship of the coupling of mechanical and electrical properties in different directions.

2.3.2 Electromechanical coupling of the piezoceramic stack

Generally, a piezoceramic stack consists of many piezoceramic sheets whose polarization directions are in line with the axis direction of stack. Therefore, the interested properties of a stack are the strain and stress along the axis direction. The constitutive equations for one-dimensional excitation and deformation of a piezoelectric element are [ANSI/IEEE Standard 176 (1987)]:

$$S = s^E T + dE \quad (2.1)$$

$$D = dT + \epsilon^T E \quad (2.2)$$

where S denotes strain of the element, s^E denotes compliance of element under constant electric field, D is the electrical density, d denotes the strain constant of material, E denotes the electric field acting on it, T denotes the mechanical stress of the material and ϵ^T denotes the dielectric permittivity of the material under constant stress. It is noticed the subscripts of the direction are dropped in the equation. The reason is that for a piezoceramic stack the interested strain and stress are in the same direction of applied electrical field. To simplify the equation, the subscripts of each term $_{33}$ are omitted here.

Nasser and Leo (2000b) derived a one dimensional model for piezoceramic stack by applying the above IEEE model of piezoelectric element to a stack with many layers of piezoelectric elements:

$$x = x_0 V - \frac{1}{K_a} F \quad (2.3)$$

$$Q = CV - x_0 F \quad (2.4)$$

where x is the displacement of stack, V denotes the voltage applied to the stack, Q represents the resulted charge and F is the force generated by the stack. The variable x_0 denotes the displacement-to-voltage constant of the stack, K_a is the stiffness and C is free-stress capacitance of the piezoceramic stack.

Under no load, we substitute $F = 0$ into Equation (2.3) and (2.4), then we have,

$$x_{free} = x_0V, \quad x_{max} = x_0V_{max} \quad (2.5)$$

$$Q_{free} = CV, \quad Q_{max} = CV_{max} \quad (2.6)$$

where x_{free} is free displacement of stack, x_{max} is the maximum displacement of the stack available, Q_{free} denotes the charge generated without load and Q_{max} is the maximum Q_{free} . In the blocked case, $x = 0$. Substituting this expression into Equation (2.3) and (2.4):

$$F_{block} = x_0K_aV, \quad F_{max} = x_0K_aV_{max} = K_ax_{max} \quad (2.7)$$

$$Q_{block} = C(1 - k^2)V = C_{block}V, \quad k^2 = \frac{K_ax_0^2}{C} \quad (2.8)$$

where F_{block} is the block force, F_{max} is the maximum force resulted from maximum voltage excitation, Q_{block} is the charge generated when stack is blocked and k^2 is the piezoelectric coupling coefficient. Figure 2.5 and Figure 2.6 show the above characteristic equations of a piezoceramic stack.

Figure 2.5 shows the force-displacement characteristics for a piezoceramic stack. At a given voltage, the available displacement decreases as the load increases. Each operation point is determined by a combination of the (F, x, Q, V) values. In the following analysis, these properties are normalized in order to simplify the analysis. Dividing Equation (2.3) by x_0V_{max} :

$$\frac{x}{x_0V_{max}} = \frac{V}{V_{max}} - \frac{F}{\frac{x_0V_{max}}{K_a}} \quad (2.9)$$

Substitute Equation (2.5) and (2.7) into the above equation:

$$\frac{x}{x_{max}} = \frac{V}{V_{max}} - \frac{F}{F_{max}} \quad (2.10)$$

The normalized and non dimensional displacement and force are defined as

$$\hat{x} = \frac{x}{x_{max}} \quad \hat{F} = \frac{F}{F_{max}} \quad \hat{V} = \frac{V}{V_{max}} \quad \hat{Q} = \frac{Q}{Q_{max}} \quad (2.11)$$

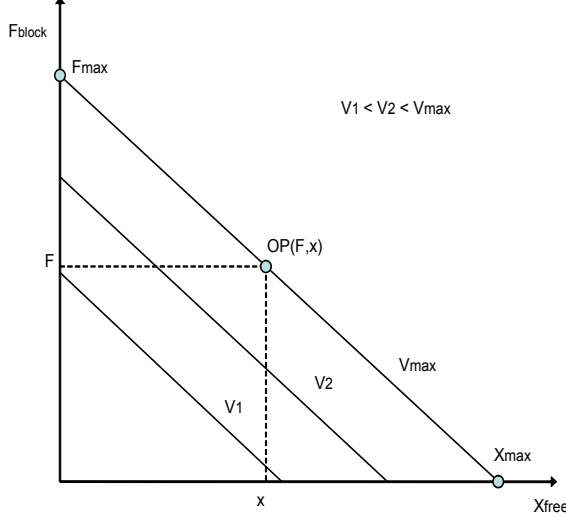


Figure 2.5: Force-displacement characteristic curve

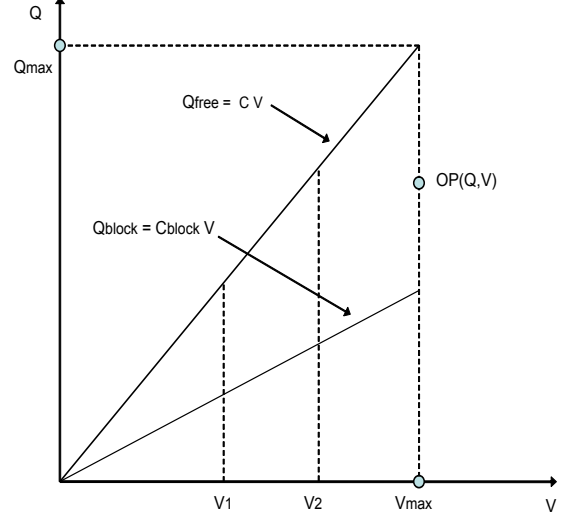


Figure 2.6: Charge-voltage characteristic curve

Substitute the above equations into Equation (2.11), the normalized force-displacement equation of a stack is:

$$\hat{V} = \hat{x} + \hat{F} \quad (2.12)$$

In the same manner, Equation (2.4) could be normalized by dividing it by CV_{max} :

$$\frac{Q}{CV_{max}} = \frac{V}{V_{max}} - \frac{x_0 F}{CV_{max}} \quad (2.13)$$

Substitute Equation (2.6), (2.7) and (2.8) into the above equation:

$$\frac{Q}{Q_{max}} = \frac{V}{V_{max}} - \frac{F}{F_{max}} k^2 \quad (2.14)$$

Substitute the definitions of the normalization Equation (2.11) into the above equation:

$$\hat{Q} = \hat{V} - k^2 \hat{F} \quad (2.15)$$

Equation (2.12) and (2.15) could be written in the matrix format as

$$\begin{bmatrix} \hat{Q} \\ \hat{V} \end{bmatrix} = A \begin{bmatrix} \hat{F} \\ \hat{x} \end{bmatrix} \quad A = \begin{bmatrix} 1 & 1 - k^2 \\ 1 & 1 \end{bmatrix} \quad (2.16)$$

2.3.3 Power efficiency of a piezoceramic stack

When operated with cyclic fashion, the normalized electrical work \hat{W}_e expended by the stack and mechanical work \hat{W}_m transferred to the load can calculate as

$$\hat{W}_e = \oint V dQ \quad \hat{W}_m = \oint F dx \quad (2.17)$$

To study the relationship of the output mechanical work with the input electrical work, we want to represent \hat{W}_e as a function of F and x . Differentiating Equation (2.16):

$$\begin{bmatrix} d\hat{Q} \\ d\hat{V} \end{bmatrix} = A \begin{bmatrix} d\hat{F} \\ d\hat{x} \end{bmatrix} \quad (2.18)$$

The electric work \hat{W}_e is

$$\hat{W}_e = \oint V dQ = \oint \begin{bmatrix} \hat{V} & \hat{Q} \end{bmatrix} \begin{bmatrix} 1 & 0 \\ 0 & 0 \end{bmatrix} \begin{bmatrix} d\hat{Q} \\ d\hat{V} \end{bmatrix} \quad (2.19)$$

$$\hat{W}_e = \oint \hat{V} d\hat{Q} = \oint \begin{bmatrix} 0 & 1 \\ 1 & 0 \end{bmatrix} \begin{bmatrix} \hat{Q} \\ \hat{V} \end{bmatrix}^T \begin{bmatrix} 1 & 0 \\ 0 & 0 \end{bmatrix} \begin{bmatrix} d\hat{Q} \\ d\hat{V} \end{bmatrix} \quad (2.20)$$

where T denotes a transpose of a matrix. Substituting Equation (2.16) and (2.18) into the above equation yields:

$$\hat{W}_e = \oint \hat{V} d\hat{Q} = \oint \begin{bmatrix} \hat{F} & \hat{x} \end{bmatrix} A^T \begin{bmatrix} 0 & 1 \\ 1 & 0 \end{bmatrix} \begin{bmatrix} 1 & 0 \\ 0 & 0 \end{bmatrix} A \begin{bmatrix} d\hat{F} \\ d\hat{x} \end{bmatrix} \quad (2.21)$$

Without losing generality, let two-by-two matrix A to be:

$$A = \begin{bmatrix} a_{11} & a_{12} \\ a_{21} & a_{22} \end{bmatrix} \quad (2.22)$$

Substitute it into Equation (2.21) and reduce the equation

$$\hat{W}_e = \oint (a_{11}a_{21} \hat{F} + a_{11}a_{22} \hat{x}) d\hat{F} + \oint (a_{12}a_{21} \hat{F} + a_{12}a_{22} \hat{x}) d\hat{x} \quad (2.23)$$

Because in a cyclic operation, the state of the system does not change at times that has an interval of any complete period, so we have

$$\oint \hat{F} d\hat{F} = 0 \quad \oint \hat{x} d\hat{x} = 0 \quad (2.24)$$

$$\oint d(\hat{F}\hat{x}) = 0 \quad (2.25)$$

From Equation (2.25), we have

$$\oint (\hat{F} d\hat{x}) + \oint (\hat{x} d\hat{F}) = 0 \quad (2.26)$$

Substitute Equation (2.24) and (2.26) into Equation (2.23) and reduce it:

$$\hat{W}_e = \oint (a_{12}a_{21} - a_{11}a_{22}) \hat{F} d\hat{x} = -|A| \hat{W}_m \quad (2.27)$$

It indicates that the normalized output mechanical work in one cycle is only a function of the electrical power expended by the stack and is not dependent on the real operation characteristics curve. Substituting the real value of matrix A in Equation (2.22) into the above equation,

$$\hat{W}_e = -k^2 \hat{W}_m \quad (2.28)$$

The negative sign indicates the electrical work is been done to the system and mechanical work is work that the system done to the load. The real electrical and mechanical work could be calculated by substituting Equation (2.5) and (2.6)

$$W_e = V_{max} Q_{max} \hat{W}_e = CV_{max}^2 \hat{W}_e \quad (2.29)$$

$$W_m = V_{max} x_{max} \hat{W}_m \quad (2.30)$$

Divided the above equation by Equation (2.29),

$$\frac{W_m}{W_e} = \frac{CV_{max}^2}{F_{max}x_{max}} \frac{\hat{W}_m}{\hat{W}_e} \quad (2.31)$$

Substituting Equation (2.28) and the definition of coupling coefficient k^2 in Equation (2.8) into the above equation, we have

$$W_m = -W_e \quad (2.32)$$

It indicates the real electrical work expended by the piezoceramic stack is equal to the work it transferred to the load, which means there is no energy loss in the stack. In the derivation of the equations we did not assume a particular characteristic curve, which means it is true for any stack operation that the electrical work equals to mechanical work. The energy balance between the electrical and mechanical domain results from the fact we neglected internal losses in the stack materials, such as hysteresis loss and friction loss, in the formulation of the coupled electromechanical equations. This is an idealization of the real materials and it is the upper bound of the energy transfer.

2.4 Definition of Efficiency Metrics

The efficiency definition are the subject of considerable debate. Nasser and Leo (2000b) defined the electrical efficiency to be the ratio of real electrical power to peak electrical power and the mechanical efficiency in the same manner. In Giurgiutiu and Rogers (Sep. 1997) used the ratio of real stored energy in the actuator to the energy stored in the actuator as efficiency. In this work the efficiency of the piezo-hydraulic actuation system is divided into two efficiency metrics. One is named electromechanical efficiency, which is defined by the ratio of mechanical energy output of the piezoelectric stack to the electrical energy input of the stack:

$$\eta_e = \frac{W_m}{W_e} \quad (2.33)$$

The energy loss that occurs due to conversion of electrical energy to mechanical energy by the piezo electric materials, which is contributed to the hysteresis losses and internal friction of the piezoelectric materials(Gilles Robert and Setter (2002)) .

The other major loss is the loss in the fluid system, which can be contributed to the friction due to the viscosity of the fluid. The definition of this mechanical efficiency is the ratio of the energy stored at the load and the energy output by the piezoceramic stack actuator:

$$\eta_m = \frac{W_{stack}}{W_L}, \quad (2.34)$$

where W_{stack} represent the energy output by the stack and W_L is the energy stored in the load.

In the cyclic operation as a piezo-hydraulic pump, the energy and work done to the system can be measured in one cycle and thus the efficiency can be computed by averaging the efficiency values of many cycles.

2.5 The Hydraulic Unit

The hydraulic system consists of the pumping chamber, the active valves, the hydraulic cylinder, the accumulator and piping. Figure 2.7 shows the setup of the system. The function of pumping chamber is to build pressurized fluid. The active valves consists of one outlet valve and one inlet valve. The accumulator is to keep the system under a bias

pre-pressure. The hydraulic fluid links the load with the piezoceramic stack and rectify the motion of stack.

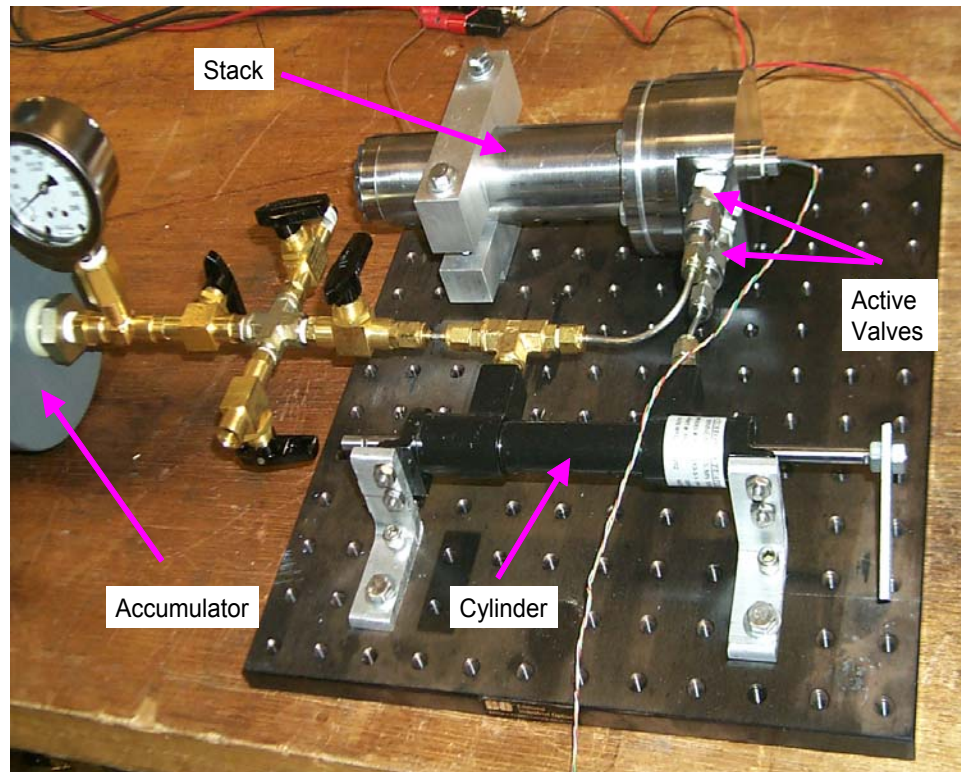


Figure 2.7: System setup

The valves are used to regulate the flow and pressure and prevent reverse flow. Passive valves have been used in piezo-hydraulic actuation system in several studies. A passive four way valve was used in a piezo-pump system by Mauck and Lynch (1999). They reported that the system performance began to degrade at 20 Hz. Nasser and Leo (2000a) developed a system that used the solenoid valves that enabled control the timing which they show were important to the performance of the system. But the operation frequency was limited under 10 Hz because the valves could not respond fast enough. Sirohi and Chopra (2002) developed a system with a small stack that enable to run into as high as 1K Hz. Their work shows that the transition of the passive valves limits the performance of the system.

In this research, active valves which consist of a piezoceramic stack actuator are adopted to operate at high frequency. Figure 2.8 shows the various parts of the active valve assembly. It include two sets of sub system, one acts as inlet valve and the other as outlet

valve. Figure 2.9 shows the cross section of one valve. At the bottom lie the piezoceramic stack, which then is connect to a pumping chamber. The chamber is designed to amplify the displacement of stack due to small strain of piezoceramic material. The stacks for the valves are high voltage stacks, which operated at the full voltage of 1000 V. The equivalent capacitance is 14.6 nF.



Figure 2.8: Parts of the active valve assembly [Kinetic Ceramics]

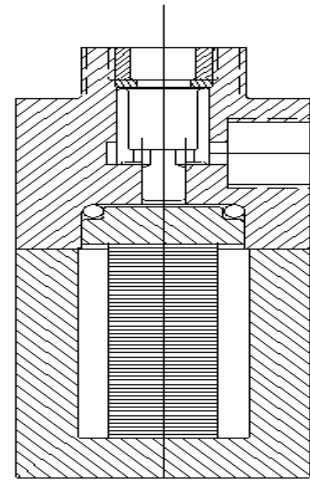


Figure 2.9: Diagram of cross section of an active valve [Kinetic Ceramics]

2.6 Effective Bulk Modulus of Fluid

In many hydraulic power applications, hydraulic fluid can be considered incompressible. Due to the high stiffness of the piezoelectric stack actuator and high operating frequency targeted for piezohydraulic applications, the compliance of the hydraulic fluid should be accounted for in system analysis and design. The bulk modulus of fluid is defined as (Doebelin (1972))

$$\beta = -\frac{\Delta P}{\Delta V/V} \quad (2.35)$$

where ΔP is the small variation of pressure and ΔV is the variation of fluid volume resulted from the variation of pressure. The minus sign is because when pressure increases, the volume of the fluid decreases.

According to Doebelin (1972), the hydraulic fluid elements could be modeled as mass and spring systems whose stiffness are linearly dependent upon the bulk modulus of the

working fluid. In many instances, the bulk modulus of the fluid is unknown due to the uncertainty of the amount of air resolved in the fluid. Manring (1997) discusses the fact that entrained air reduces the bulk modulus compared to that of pure hydraulic fluid.

2.7 Inviscid Flow in the Hydraulic System

This section will discuss the characteristics of an incompressible and inviscid steady flow. By assuming the fluid is inviscid, we eliminate the friction. By assuming a steady flow, the flow is fully developed and will not change with time. This model neglects the energy losses in the fluid flow, which could be considerably different from the real cases. However, it can provide the basis feature of a piezo-actuation system when combined with the model of the piezoceramic stack. It also is the upper bound of the performance that is possible and thus it is of interests to investigate this model.

Conservation of mass is one of the basic governing equations of the fluid flow. The conservation of mass principle states that mass can not be created or destroyed, which means the decrease of mass in the control volume should be equal to mass outflow, as in Equation (2.36):

$$\int_s \rho \mathbf{v} \cdot \mathbf{n} dS = - \int_v \frac{\partial \rho}{\partial t} dv \quad (2.36)$$

where S is the surface and v is the volume of the selected control volume, \mathbf{v} is the velocity vector and \mathbf{n} is the normal vector of the point on the small piece of surface dS . This equation can be applied to any flow.

Based on the assumption of incompressible and inviscid flow, there is no shear stress in the flow field. Eulerian equations of motion were obtained through analyzing the motion of a small particle of the fluid in [R. H. Sabersky and Gates (1999)]. Equation (2.37) is the vector form of the Eulerian equations:

$$\frac{D\mathbf{v}}{Dt} = -\frac{1}{\rho}\nabla p + \mathbf{f} \quad (2.37)$$

where \mathbf{v} is the velocity vector, p is the pressure and \mathbf{f} is the external force vector. The operation D is defined as:

$$\frac{D}{Dt} = \frac{\partial}{\partial t} + u \frac{\partial}{\partial x} + v \frac{\partial}{\partial y} + w \frac{\partial}{\partial z} \quad (2.38)$$

Figure 2.10 shows streamlines of an inviscid flow through a duct. Point 1 and 2 are on the same streamline. By integrating the above Eulerian equations along a streamline, R. H. Sabersky and Gates (1999) obtained Bernoulli's equation:

$$\frac{V_1^2}{2} + \frac{p_1}{\rho} + gh_1 = \frac{V_2^2}{2} + \frac{p_2}{\rho} + gh_2 \quad (2.39)$$

where V , p and h are respectively the velocity, pressure and height at that point. It is noted the assumptions of Bernoulli's equation are incompressible, steady and Inviscid flow and it is valid along an individual streamline.

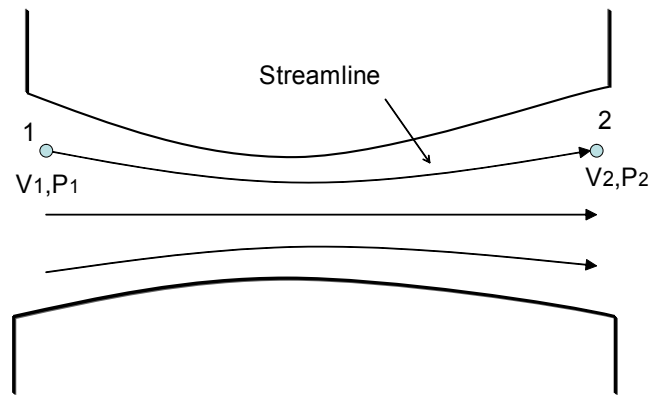


Figure 2.10: Streamlines in flow through a duct

In the next chapter, an inviscid flow model will be analyzed with the above obtained equations. Because this Inviscid flow model does not take into account the friction loss through the pipes circuit, it can provide an upper bound of the performance of the actuation system.

2.8 Viscous Flow in the Hydraulic Unit

In this section, energy equation for viscous flow in the hydraulic unit will be derived on the basis of the first law of thermodynamics. The velocity profile coefficients and head losses in the energy equations are determined for both laminar flow and turbulent flow. The energy equations will be used to derive the model for the whole system in the next chapter.

2.8.1 Energy Analysis for A Control Volume

In a viscous fluid, the surface forces acting on an element of fluid not only include the normal force or stress similar to pressure, but also include shear forces or stress resulted from the viscosity of the fluid. The shear stress τ of one dimensional flow can be calculated as following [R. H. Sabersky and Gates (1999)]:

$$\tau = \mu \frac{du}{dy} \quad (2.40)$$

where μ is the viscosity of the fluid, u is the velocity and y is the direction that is normal to the direction of flow. The direction of shear stress acted on the fluid element is in the opposite direction of its velocity. Due to the friction introduced by the viscosity, the Bernoulli's equation (Equation (2.39)) can not be directly applied to viscous flow.

To develop the energy equations of flow, a control volume is used to apply first law of thermodynamics. Figure 2.11 shows a control volume *c.v.* in the fluid flow. The energy equation for the system in the control volume is [Fox and McDonald (1978)]

$$\dot{Q} + \dot{W} = \frac{\partial}{\partial t} \int_{CV} e\rho d\nu + \int_{CS} e\rho \mathbf{v} d\mathbf{S} \quad (2.41)$$

where \dot{Q} and \dot{W} is respectively the rate of heat transferred and work done to the control volume and e is the energy per unit mass of the fluid element and is defined by:

$$e = u + \frac{V^2}{2} + gz \quad (2.42)$$

where u , $\frac{V^2}{2}$ and gz is respectively the internal energy, kinetic energy and potential energy per unit mass of the fluid. The first term in the right part of Equation (2.41) represents the rate of change of total energy in the control volume and the last term represents the rate of energy flowing out of the control volume. Note that Equation (2.41) does not assume any particular form of flow and thus it could be applied to any fluid flow. For steady flow, the term $\frac{\partial}{\partial t} \int_{CV} e\rho d\nu$ is zero, so Equation (2.41) becomes

$$\dot{Q} + \dot{W} = \int_{CS} e\rho \mathbf{v} d\mathbf{S} \quad (2.43)$$

The rate of work done on the control volume is conveniently subdivided into four classifications:

$$\dot{W} = \dot{W}_s + \dot{W}_{pressure} + \dot{W}_{shear} + \dot{W}_{other} \quad (2.44)$$

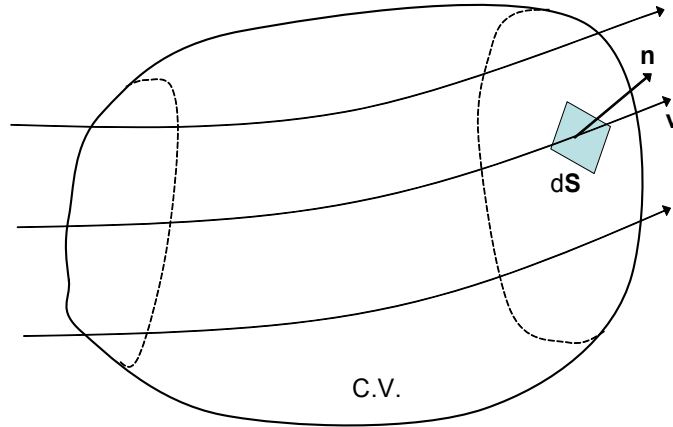


Figure 2.11: A control volume in the flow

The first term \dot{W}_s is shaft work. The second term $\dot{W}_{pressure}$ is the work done by pressure, which could be expressed as,

$$\dot{W}_{pressure} = - \int_{CS} p \mathbf{v} \cdot d\mathbf{S} \quad (2.45)$$

The minus sign in the above equation is because the direction of p is in the opposite of the normal direction of $d\mathbf{S}$. The third term \dot{W}_{shear} is the rate of work done by the shear force to the control volume and the last term \dot{W}_{other} is used to account for other energy source such as electrical energy and electromagnetic energy. In our case, we assume no other work done on the system, which means that \dot{W}_{other} is zero. Substitute Equations (2.44) and (2.45) into Equation (2.43), we obtain the energy equation for steady flow as

$$\dot{Q} + \dot{W}_s + \dot{W}_{shear} = \int_{CS} \left(u + \frac{p}{\rho} + \frac{V^2}{2} + gz \right) \rho \mathbf{v} \cdot d\mathbf{S} \quad (2.46)$$

Equation (2.46) is derived by applying the first thermodynamics law to a general control volume as in Figure 2.11. We can simplify it if we carefully choose the control volume as in Figure 2.12. The control volume boundaries are shown as dashed lines. They are normal to the flow at sections 1 and 2 and coincide with the inside pipe wall at other locations.

Figure 2.13 shows a typical velocity profile of a section for viscous flow through a pipe. Note the velocity in one section is not uniform due to the viscosity of the fluid. Because of the no slipping boundary conditions at the inside pipe wall, the velocity of the

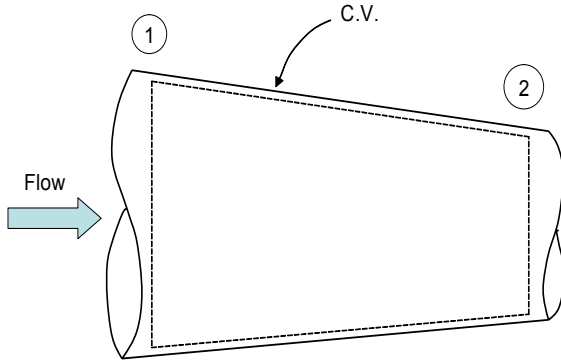


Figure 2.12: Control volume for flow through a pipe

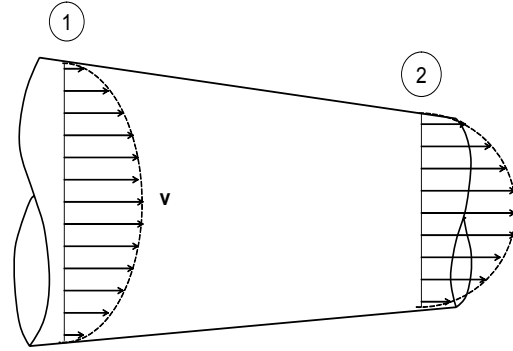


Figure 2.13: Velocity profile of flow through a pipe

fluid at the inside pipe wall is zero. In the control volume in Figure 2.12, although shear stress is present at the walls of pipe, \dot{W}_{shear} is zero because the velocity there is zero. Equation 2.46 can be reduced to

$$\dot{Q} + \dot{W}_s = \int_{A_2} \left(u_2 + \frac{p_2}{\rho} + \frac{V_2^2}{2} + gz_2 \right) \rho V_2 dA_2 - \int_{A_1} \left(u_1 + \frac{p_1}{\rho} + \frac{V_1^2}{2} + gz_1 \right) \rho V_1 dA_1 \quad (2.47)$$

Assume that in a section the temperature of fluid is uniform so that the internal energy u is also uniform. Also assume the pressure in a section is uniform. We have

$$\begin{aligned} \dot{Q} + \dot{W}_s = & \left(u_2 + \frac{p_2}{\rho} + gz_2 \right) \int_{A_2} \rho V_2 dA_2 - \left(u_1 + \frac{p_1}{\rho} + gz_1 \right) \int_{A_1} \rho V_1 dA_1 + \\ & \int_{A_2} \frac{V_2^2}{2} \rho V_2 dA_2 - \int_{A_1} \frac{V_1^2}{2} \rho V_1 dA_1 \end{aligned} \quad (2.48)$$

Note that according to conservation of mass, the mass flow at section 1 and 2 should be equal

$$\dot{m} = \int_{A_2} \rho V_2 dA_2 = \int_{A_1} \rho V_1 dA_1 \quad (2.49)$$

Thus, Equation 2.48 could be reduced to

$$\dot{Q} + \dot{W}_s = \dot{m} \left(u_2 + \frac{p_2}{\rho} + gz_2 \right) - \dot{m} \left(u_1 + \frac{p_1}{\rho} + gz_1 \right) + \int_{A_2} \frac{V_2^2}{2} \rho V_2 dA_2 - \int_{A_1} \frac{V_1^2}{2} \rho V_1 dA_1 \quad (2.50)$$

Dividing the above equation by \dot{m}

$$\frac{\dot{Q}}{\dot{m}} + \frac{\dot{W}_s}{\dot{m}} = \left(u_2 + \frac{p_2}{\rho} + gz_2 \right) - \left(u_1 + \frac{p_1}{\rho} + gz_1 \right) + \frac{\int_{A_2} \frac{V_2^2}{2} \rho V_2 dA_2}{\int_{A_2} \rho V_2 dA_2} - \frac{\int_{A_1} \frac{V_1^2}{2} \rho V_1 dA_1}{\int_{A_1} \rho V_1 dA_1} \quad (2.51)$$

Note that the last two terms are only determined by the velocity profile in the section. To eliminate the integrate signs, a coefficient α will be defined such that

$$\int_A \frac{V^2}{2} \rho V dA = \alpha \int_A \frac{\bar{V}^2}{2} \rho V dA = \alpha \dot{m} \frac{\bar{V}^2}{2} \quad (2.52)$$

where \bar{V} is the average velocity of the section and is defined by

$$\bar{V} = \frac{\int_A V dA}{A} \quad (2.53)$$

Substitute Equation (2.52) into Equation (2.51) and rearrange it, we have

$$\left(\alpha_1 \frac{\bar{V}_1^2}{2} + \frac{p_1}{\rho} + gz_1 \right) - \left(\alpha_2 \frac{\bar{V}_2^2}{2} + \frac{p_2}{\rho} + gz_2 \right) = (u_2 - u_1) - \frac{\dot{Q}}{\dot{m}} - \frac{\dot{W}_s}{\dot{m}} \quad (2.54)$$

Note that in Equation (2.54), the term $\left(\alpha \frac{\bar{V}^2}{2} + \frac{p}{\rho} + gz \right)$ represents the mechanical energy per unit mass at a cross section and $\frac{\dot{W}_s}{\dot{m}}$ is the mechanical work done to the fluid per unit mass. Thus the term $(u_2 - u_1) - \frac{\dot{Q}}{\dot{m}}$ represents the change of internal energy per unit mass, which means the amount of mechanical energy converted into unwanted thermal energy and heat loss. It can be identified as the head loss h_l and the term $\frac{\dot{W}_s}{\dot{m}}$ can be represented as the head added by external work h_w . Then

$$\left(\alpha_1 \frac{\bar{V}_1^2}{2} + \frac{p_1}{\rho} + gz_1 \right) - \left(\alpha_2 \frac{\bar{V}_2^2}{2} + \frac{p_2}{\rho} + gz_2 \right) = h_l - h_w \quad (2.55)$$

Note if there is no friction, head loss h_l is zero, and also the velocity in a section is uniform thus the velocity coefficient $\alpha = 1$. And if we assume there is no external work done to the system, Equation (2.55) turns out to be the same as the Bernoulli's equation. Equation (2.55) predict the states at the outlet of a control volume related with the inlet states and head loss in terms of energy respect for an incompressible steady flow. The head loss h_l and velocity coefficient α have to be determined when Equation (2.55) is used to analyze the flow. The next section will concentrate on determining them for different types flow.

2.8.2 Determination of Velocity Profile Coefficient α

Viscous flows can be classified into laminar or turbulent flow on the basis of internal flow structure. In laminar flow, flow structure is characterized by motion in lamina while flow structure in turbulent flow is characterized by random motions of fluid particles. For a

viscous flow through pipes, whether a flow is laminar or turbulent depends on the Reynolds number,

$$Re = \frac{\bar{V}D}{\nu} \quad (2.56)$$

where \bar{V} is the average velocity, D is the diameter of the pipe and ν is the kinetic viscosity of the fluid. Under normal engineering conditions, for $Re > 3000$ the flow is usually turbulent, for $Re < 2000$ the flow is completely stable and will be laminar and for $2000 < Re < 3000$ the transition occurs [R. H. Sabersky and Gates (1999)].

Because of the different flow structures of laminar and turbulent flow, the velocity profile and head loss of the flow will be also different. Figure 2.14 shows the velocity profiles of laminar and turbulent flow in a pipe whose radius is R . The maximum velocity U is at the center of the pipe. It is noted that for the turbulent flow the velocity profile is more uniform while for laminar flows the velocity profile is parabolic .

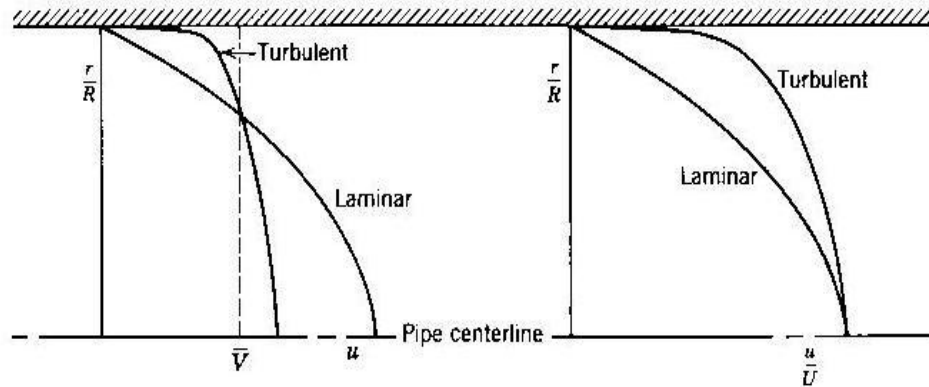


Figure 2.14: Velocity profiles for laminar and turbulent flow in a pipe at $Re = 4 \times 10^3$ [Fox and McDonald (1978)]

Fox and McDonald (1978) derived the velocity profile of laminar pipe flow by assuming the pressure is uniform in a cross section and pressure gradient $\frac{\partial p}{\partial x}$ is constant. The result showed that velocity profile is a parabolic function of the distance from the centerline:

$$V = -\frac{R^2}{4\mu} \frac{\partial p}{\partial x} \left[1 - \frac{r^2}{R^2}\right] \quad (2.57)$$

where R is the radius of pipe, μ is dynamic viscosity of fluid and r is the distance from centerline. Note that the minus sign is because the gradient of pressure is negative. The

maximum velocity is at $r = 0$:

$$V_{max} = -\frac{R^2}{4\mu} \frac{\partial p}{\partial x} = U \quad (2.58)$$

So that we have

$$\frac{V}{U} = 1 - \frac{r^2}{R^2} \quad (2.59)$$

The average velocity \bar{V} and velocity coefficient α for laminar flow could be calculated by Equations (2.52) and (2.53):

$$\bar{V} = \frac{\int_A V dA}{A} = \frac{\int_0^{2\pi} \int_0^R U(1 - (\frac{r}{R})^2) r dr d\theta}{\pi R^2} = \frac{U}{2} \quad (2.60)$$

$$\alpha = \frac{\int_A \frac{V^2}{2} \rho V dA}{\int_A \frac{\bar{V}^2}{2} \rho V dA} = 2 \quad (2.61)$$

Note that for laminar flow, the average velocity is half of the maximum velocity and the velocity profile coefficient α is a constant 2 for different Reynolds number. This is not the case for a turbulent flow. There is no rigorous theoretical equation to exactly describe turbulent flows. Thus experiment becomes more important. The velocity profile for turbulent flow through a pipe can be represented by the empirical equation [Fox and McDonald (1978)]

$$\frac{V}{U} = (1 - \frac{r}{R})^{1/n} \quad (2.62)$$

where n is a integer which depends on the Reynolds number. When Reynolds number increases, the value of n increases. For example, for $Re = 4 \times 10^3$ the value of n is 6 for $Re = 3.2 \times 10^6$ n is 10. In the same manner, average velocity \bar{V} and velocity coefficient α for turbulent flow could be calculated by Equations (2.52) and (2.53):

$$\bar{V} = \frac{\int_A V dA}{A} = \frac{2n^2}{(n+1)(2n+1)} U \quad (2.63)$$

$$\alpha = \frac{\int_A \frac{V^2}{2} \rho V dA}{\int_A \frac{\bar{V}^2}{2} \rho V dA} = \frac{(n+1)^3(2n+1)^3}{4n^4(n+3)(2n+3)} \quad (2.64)$$

Let $\gamma = \frac{\bar{V}}{U}$ be the normalized average velocity. Figure 2.15 shows the variation of γ and α with different values of n . As n increases, γ increases and approaches 1 and the

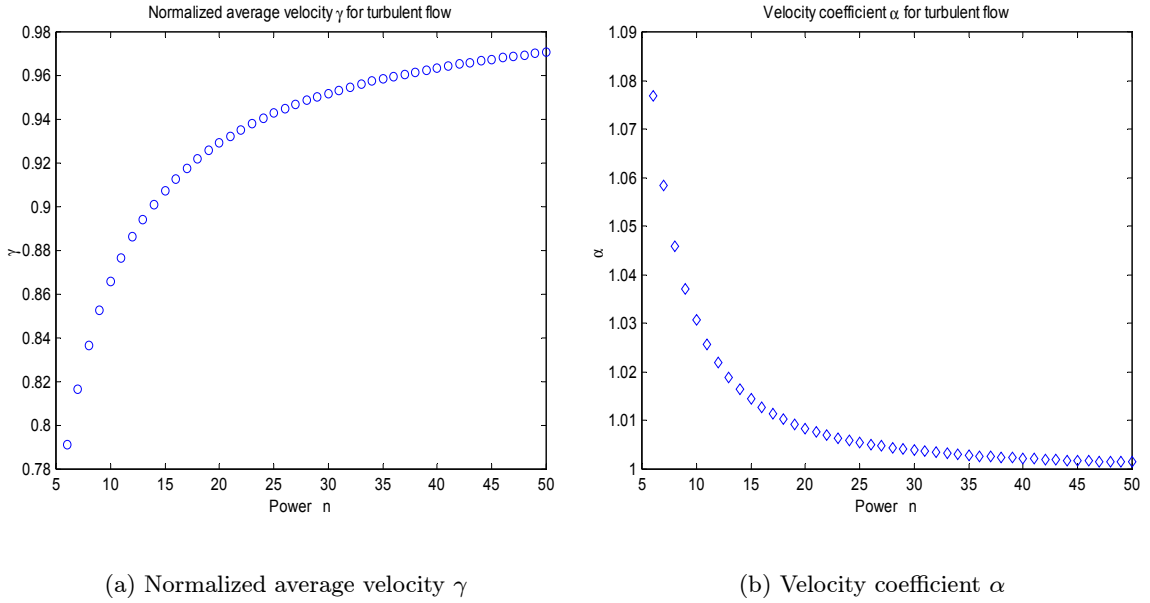


Figure 2.15: Velocity profile for different value of power n

value of α decreases but also approaches 1, which means the velocity profile of turbulent flow becomes more like uniform for higher Reynolds number.

In this section, velocity profile of laminar flow and turbulent flow is calculated. For laminar flow, the velocity profile coefficient α is a constant 2, while for turbulent flow, the value of α will vary with Reynolds number and approaches 1 as Reynolds number increases. The value of α can be approximated by 1 for $n > 10$, which corresponds to Reynolds number $Re > 3.2 \times 10^6$.

2.8.3 Determination of Head Losses

When fluid flows through pipes, the friction resulted from the viscosity of the fluid will reduce the energy of fluid. This causes an unconvertible energy transform from mechanical energy to thermal energy. The energy loss or head loss can be divided into two major classifications. One kind of losses is named major losses due to the friction of the inside wall of pipes. The other kind of losses is minor losses resulted from the variation of area of section or direction of flow in pipe connectors, such as valves, orifices and elbows.

The major losses for a fully developed laminar flow in a ideal pipe can be analytically

calculated. Fox and McDonald (1978) derived that the expression is

$$h_{major} = \left(\frac{64}{Re}\right) \frac{L}{D} \frac{\bar{V}^2}{2} \quad (2.65)$$

In the case of turbulent flow, no analytical equations can be applied to describe the flow directly. Both experimental data and dimensional analysis are used to determine the loss function. In Fox and McDonald (1978), dimensional analysis shows that the friction factor f , which is defined by

$$f = \frac{D}{L} \frac{2}{\bar{V}^2} h_{major} \quad (2.66)$$

is only a function of Reynolds number Re and pipe roughness e :

$$f = \phi\left(Re, \frac{e}{D}\right) \quad (2.67)$$

Experiments were tested to determine the function ϕ . Figure 2.16 shows the experimentally measured friction factors f for different Re and pipe roughness e . For turbulent flow, the friction factor decreases as Reynolds number for all pipe roughness. But it varies little for very high Reynolds number. The major losses h_{major} for turbulent flow can be calculated by Equation (2.66) and by f determined by the Moody chart in Figure 2.16.

The minor losses result from abrupt changes in area in the flow. These losses are called minor losses because compared to losses through long pipe, their values normally are smaller than major losses. In a piezo-hydraulic system, the piping is general short in order to make the system compact and minimize major losses, thus the minor losses are more of importance than other hydraulic applications. Since the flow pattern in fittings and valves is quite complex, the losses are commonly measured experimentally and correlated with the pipe-flow parameters. The minor losses may be expressed as

$$h_{minor} = K \frac{\bar{V}^2}{2} \quad (2.68)$$

where K is the loss coefficient, which is usually determined by experimental results. The value of K can vary with different type of fittings.

For a piezo-hydraulic actuation system, there are various piping and fittings, such as entrance to pipe, enlargement and contraction, pipe bends and valves. These common situations are summarized below.

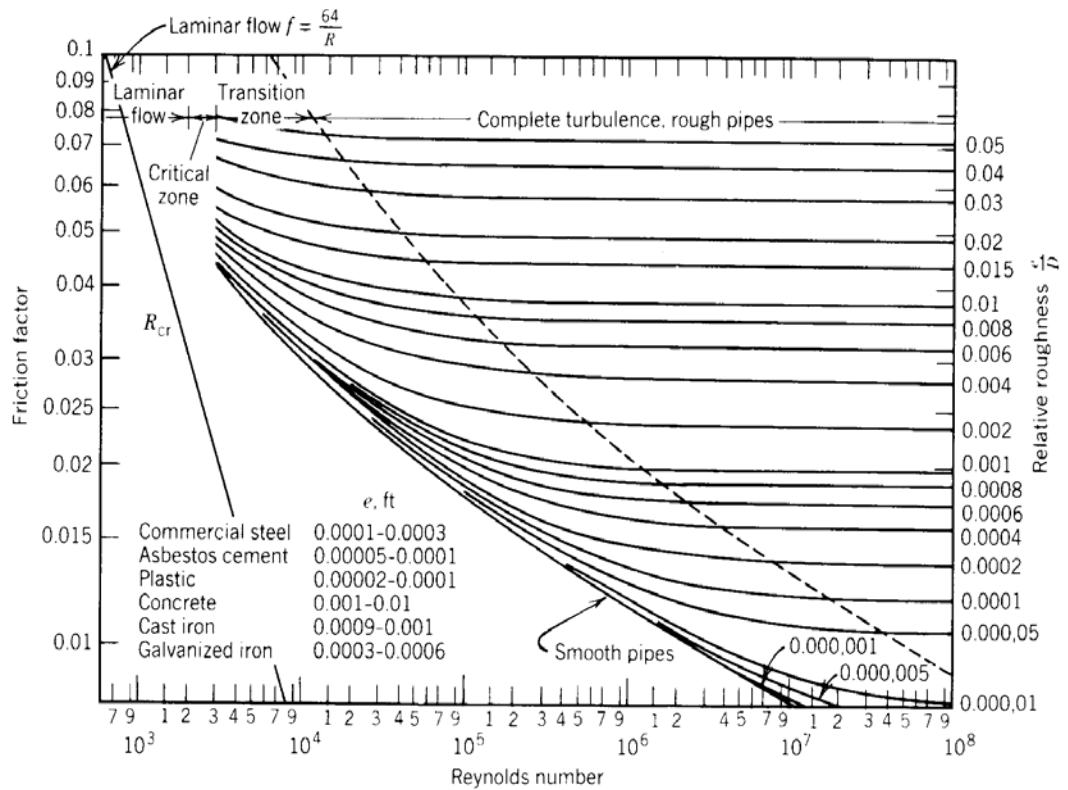


Figure 2.16: Moody diagram for fully developed flow in circular pipes [Tullis (1989)]

Entrances to Pipes

The entrance losses happen when the fluid from a big area flows into a small pipe area. This losses may result in a big pressure drop at the entrance if the shape of inlet is not smooth. Figure 2.17 shows the typical value of loss coefficient for different entrance types.

Sudden Expansions and Contractions

Sudden expansions and contractions are very common in hydraulic circuits. In Fox and McDonald (1978), minor loss coefficients of sudden expansion is calculated theoretically by

$$K_{SE} = \left(1 - \frac{d^2}{D^2}\right)^2 \quad (2.69)$$

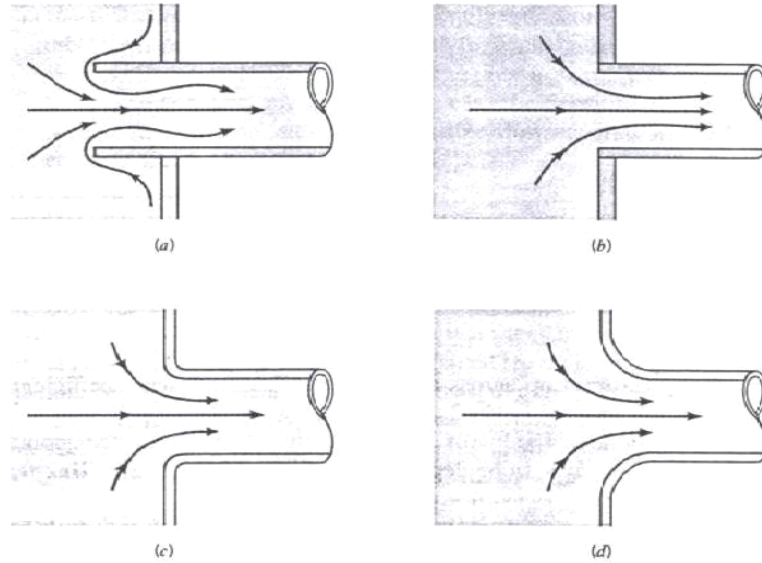


Figure 2.17: Loss coefficient for different entrance types. (a) Reentrant, $K = 0.8$, (b) sharp-edged, $K = 0.5$, (c) slightly rounded, $K = 0.2$, (d) well-rounded, $K = 0.04$. [Munson and Young (1998)]

The loss coefficients of sudden contractions are determined by experimental because the theory for them are not well developed:

$$K_{SC} = 0.42 \left(1 - \frac{d^2}{D^2}\right) \quad (2.70)$$

which can fit experimental data well for $\frac{d}{D} < 0.76$. Figure 2.18 shows the loss factor K for the sudden expansions and contractions. Note that when using $h_l = K \frac{\bar{V}^2}{2}$ to calculate head loss h_l , the average velocity of the smaller section \bar{V} should be used.

Pipe Bends

When the pipe is not straight, extra losses will be introduced besides the simple Moody friction loss. The loss coefficients K due to pipe bends is a function of the pipe roughness and ratio of bending radius to diameter of pipe, R/D , [White (1994)]. For the piezo-hydraulic system, generally the value of ratio is big enough such that the loss coefficient K is relatively a constant. In Munson and Young (1998) for a regular 90° elbow the loss coefficient K is 0.3 and for a regular 180° return bends K is 0.2.

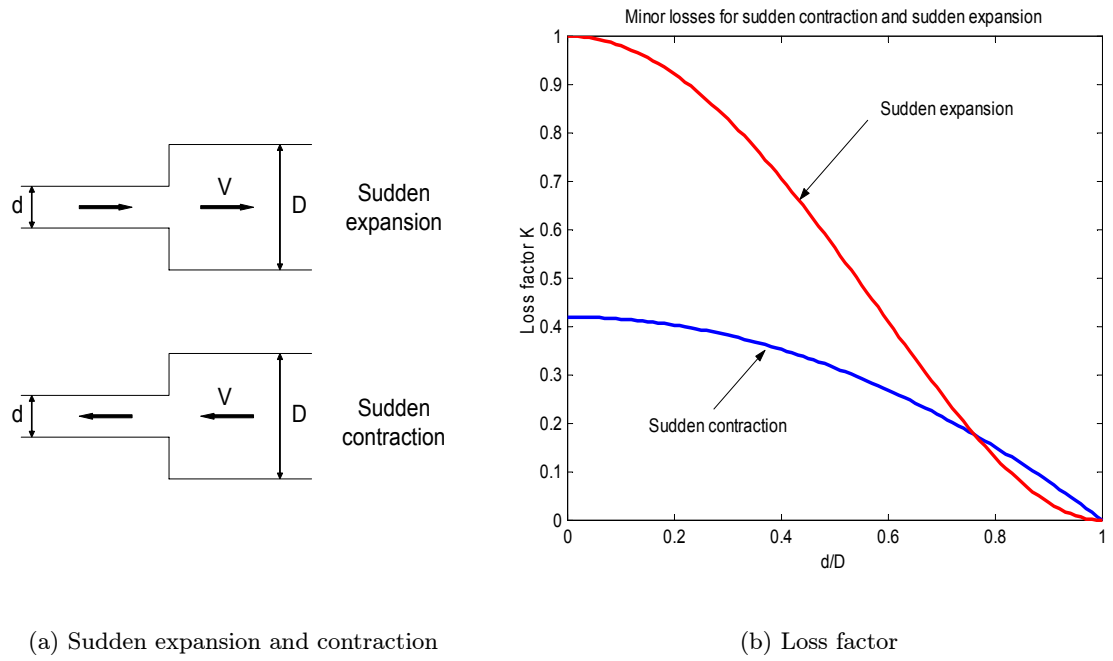


Figure 2.18: Loss factor of sudden expansion and contraction

Valves

The loss for a valve is different from other minor losses in that the loss can vary with the degree of open position. Losses can be much higher for a partially opened valve. The active valves are actuated by a piezoceramic stack which can expand and contract very fast. The rising time of the valves could be decreased to less than one millisecond (Kinetic Ceramics). The transition of the valves are neglected to simplify the model. The valve can be considered as only having two states, one is closed and the other one is fully open.

The losses factor of the run flow K_r and branch flow K_b of a **T** can be determined by

$$K_r = 1 \quad K_b = 3 \quad (2.71)$$

2.9 Summary

In this chapter, a model for piezoceramic stack is presented. Though it does not take account in the energy loss in the actuator, it represents a upper bound of electromechanical coupling of the stack. Then the hydraulic system is analyzed. Both Inviscid and viscous

flows pattern in the hydraulic unit of the system is analyzed in terms of energy respect. Finally, Major losses and minor losses are determined for both laminar and turbulent flow conditions.

Chapter 3

Model of Piezo-Hydraulic Actuation System

3.1 Introduction

In this chapter, definition of power and efficiency of the hydraulic actuation system will be presented. Three theoretical models of the piezo-hydraulic actuation system will be presented based on the four stage operation model derived in Chapter 2. Flow equations derived in *Chapter 2* will be used to obtain the model for the system. First, an ideal model that assumed incompressible and inviscid fluid flow will be analyzed. Power and efficiency will be determined analytically. Then, the viscosity of the fluid will be considered and an incompressible viscous flow model will be presented. The Reynolds number of the fluid flow will be determined and head losses will be calculated in each part. The equations of the whole system will be derived by applying energy analysis for control volumes. Finally, a compressible viscous flow model is presented to address the compressibility of the working fluid.

The output power of the piezo-hydraulic actuation system can be calculated by

$$Power = Work f \quad (3.1)$$

where *Work* is the work done in each period and *f* is the operating frequency. In the ideal case, the output power is proportional to the frequency.

The energy loss in a piezo-hydraulic actuation system can be classified into two major sources. One is the losses in the electromechanical coupling in the piezoceramic stack due to

hysteresis and internal friction. The hysteresis loss is dependent on many factors, including the operating frequency, the electrical excitation signal and physical parameters of the materials. The other major losses are losses in the hydraulic circuits due to the viscosity of fluid. The total efficiency η of the actuation system is the product of the electromechanical efficiency η_e and mechanical efficiency η_m :

$$\eta = \eta_e \eta_m \quad (3.2)$$

In this work, we emphasize the analysis the mechanical efficiency. Three models will be presented to determine performance and power efficiency of the system.

3.2 The Incompressible Inviscid Fluid (IIF) Model

Several assumptions will be made when developing the model. The first assumption is quasi-steady flow, which means the acceleration of fluid will be neglected. The second is that an incompressible and inviscid fluid will be assumed. Another assumption is that the velocity in a section is uniform in the pipe because there is no shear stress in the fluid.

The setup diagram are shown in Figure 3.1. Some important parameters are also shown. The pressure of the accumulator is P_{acc} , the gravity of the load is G_L , the cross section area of the pumping is A_{ch} and the bore area of the cylinder is A_{cy} . Due to the different area on the two sides of the single-ended cylinder, a parameter γ is introduced to denote the ratio of the area of larger side to the area of smaller side. Thus for a single-ended cylinder, γ is always bigger than one. If the area of the pumping chamber is different from the area of the bore in the cylinder, a hydraulic amplification exists. To simplify the calculations, an hydraulic amplification factor λ is denoted by

$$\lambda = \frac{A_{ch}}{A_{cy}} \gamma \quad (3.3)$$

In the following paragraph, we will derive the model for a single-ended cylinder. To evaluate the results for a double-ended cylinder, we only need to let γ to be equal to one.

3.2.1 Four-Stage Operation

The model will be based on the four-stage model presented in Figure 2.3. We assume the outlet valve opens when the pressure in the pumping chamber reaches a specific value, which

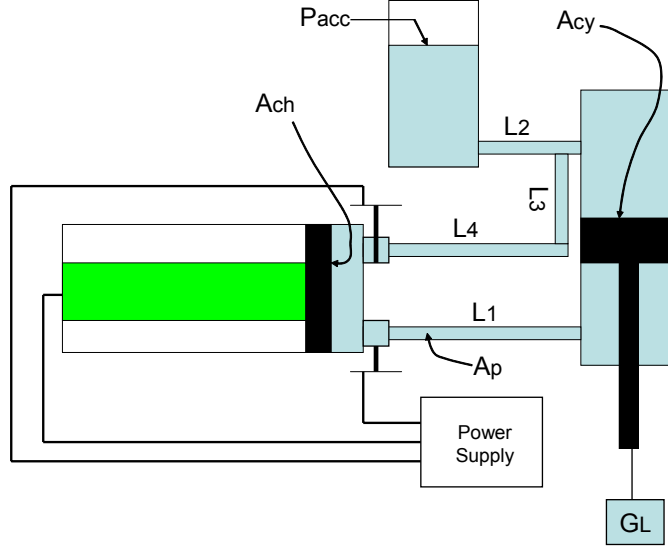


Figure 3.1: Setup diagrams and parameters

is the pressure that is able to move the load. To determine that outlet pressure P_{out} , the free body diagram of the piston in the hydraulic cylinder is shown in Figure 3.2. We have

$$\begin{aligned}
 P \frac{A_{cy}}{\gamma} - P_{acc} A_{cy} - G_L &= 0 \\
 P_{out} = P &= (P_{acc} + \frac{G_L}{A_{cy}}) \gamma
 \end{aligned} \tag{3.4}$$

In the first *compression* stage, the stack will compress the fluid while both valves are closed. The *exhaustion* stage occurs when the pressure in the closed chamber reaches the P_{out} . The outlet valve opens and the stack actuator continues to push the fluid. After the stack reaches the maximum stroke, the outlet valve closes and the stack actuator begins to contract, which is the *expansion* stage. During the *intake* stage, the inlet valve opens and the stack continues to contract, which results in the fluid in the accumulator flowing into the chamber. The following paragraphs will discuss each stage in detail to evaluate the performance of the system.

The system is originally pre-pressurized to the accumulator pressure P_{acc} . The characteristic equation of a stack is described by Equations (2.3) and (2.4). When the system is pre-pressurized, we assume the displacement of stack x is zero. Thus by Equation (2.3), the corresponding voltage is

$$V = \frac{P_{acc} A_{ch}}{x_0 K_a} \tag{3.5}$$

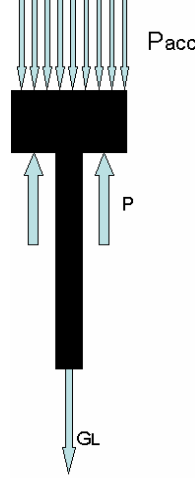


Figure 3.2: Free body diagram of piston in the cylinder

In the *compression* stage, the initial conditions are

$$\begin{aligned}
 F_1 &= P_{acc} A_{ch} \\
 x_1 &= 0 \\
 V_1 &= \frac{P_{acc} A_{ch}}{x_0 K_a} \\
 Q_1 &= C \frac{P_{acc} A_{ch}}{x_0 K_a} - x_0 P_{acc} A_{ch} = \left(\frac{1}{k^2} - 1 \right) x_0 P_{acc} A_{ch} \quad (3.6)
 \end{aligned}$$

During the compression stage, the displacement x is zero. Thus the characteristic equations in Equations (2.3) and (2.4) turn into

$$\begin{aligned}
 0 &= x_0 V - \frac{1}{K_a} F \\
 Q &= CV - x_0 F \quad (3.7)
 \end{aligned}$$

At the end of the compression, we have $x_2 = 0$ and $F_2 = P_{out} A_{ch}$. Substitute these conditions into Equation (3.7), we have the ending states of the *compression* stage

$$\begin{aligned}
 F_2 &= \left(P_{acc} + \frac{G_L}{A_{cy}} \right) A_{ch} \gamma = P_{acc} A_{ch} \gamma + G_L \lambda \\
 x_2 &= 0 \\
 V_2 &= \frac{P_{acc} A_{ch} \gamma + G_L \lambda}{x_0 K_a} \\
 Q_2 &= \left(\frac{C}{x_0 K_a} - x_0 \right) (P_{acc} A_{ch} \gamma + G_L \lambda) = \left(\frac{1}{k^2} - 1 \right) x_0 (P_{acc} A_{ch} \gamma + G_L \lambda) \quad (3.8)
 \end{aligned}$$

In the *exhaustion* stage, the initial states will be the ending states in the *compression* stage. Through the stage, the pressure in the chamber is constant at P_{out} . The characteristics equation is

$$\begin{aligned}x &= x_0 V - \frac{1}{K_a} P_{out} A_{ch} \\Q &= CV - x_0 P_{out} A_{ch}\end{aligned}\quad (3.9)$$

At the end of the stage, the excitation voltage of stack reaches the maximum value V_{max} . We denotes the states at the end of the *exhaustion* stage by subscription 3. So We have

$$\begin{aligned}F_3 &= P_{acc} A_{ch} \gamma + G_L \lambda \\x_3 &= x_0 V_{max} - \frac{P_{acc} A_{ch} \gamma + G_L \lambda}{K_a} \\V_3 &= V_{max} \\Q_3 &= C V_{max} - x_0 (P_{acc} A_{ch} \gamma + G_L \lambda)\end{aligned}\quad (3.10)$$

In the *expansion* stage, the initial states are the ending states of the *exhaustion* stage. The stack contracts and the pressure in the chamber decreases to the accumulator pressure while both valve is closed. Because the fluid is incompressible, through this stage the actual stack position x remains constant. $x = x_3$. But the force acting on the stack actuator F decreases because the pressure in the chamber drops. The characteristics equation in this stage is

$$\begin{aligned}x_3 &= x_0 V - \frac{1}{K_a} F \\Q &= CV - x_0 F\end{aligned}\quad (3.11)$$

At the end of the stage, the pressure in the chamber is equal to P_{acc} and the force acting on stack is thus $F = P_{acc} A_{ch}$. The position of stack x remains constant at x_3 . Thus all the states can be calculated by Equation (3.11)

$$\begin{aligned}F_4 &= P_{acc} A_{ch} \\x_4 &= x_0 V_{max} - \frac{P_{acc} A_{ch} \gamma + G_L \lambda}{K_a} \\V_4 &= \frac{x_4}{x_0} - \frac{F_4}{K_a} = V_{max} - \frac{(\gamma - 1) P_{acc} A_{ch} + G_L \lambda}{K_a x_0} \\Q_4 &= C V_4 - x_0 F_4 = C \left(V_{max} - \frac{(\gamma - 1 + k^2) P_{acc} A_{ch} + G_L \lambda}{K_a x_0} \right)\end{aligned}\quad (3.12)$$

In the *intake* stage, the stack contracts while the pressure in the chamber remains to be a constant F_4 . The characteristics equation of this stage is

$$\begin{aligned} x &= x_0 V - \frac{1}{K_a} F_4 \\ Q &= C V - x_0 F_4 \end{aligned} \quad (3.13)$$

At the end, the stack returns to the initial position which is set to be 0 and the pressure becomes equal to the accumulator pressure. The complete states can be calculated by Equation 3.13

$$\begin{aligned} F_5 &= P_{acc} A_{ch} \\ x_5 &= 0 \\ V_5 &= \frac{P_{acc} A_{ch}}{x_0 K_a} \\ Q_5 &= \left(\frac{1}{k^2} - 1 \right) x_0 P_{acc} A_{ch} \end{aligned} \quad (3.14)$$

By comparing Equation (3.6) and (3.14), we observe that the states with subscript 5 are the same as the states with the subscript 1, which means the states of the system return to the original states after a cycle of the four stages.

3.2.2 Work and Efficiency

The force-displacement curves of the stack actuator are determined by characteristics equations of each stage. The mechanical work done by the actuator in one cycle can be determined by calculating the area encircled by the force-displacement curves. In the same manner, the output work of the system, which is also the work done to the load, can be calculated. Figure 3.3 shows the force-displacement curve of the stack actuator and the load in one cycle. Due to hydraulic amplification, the displacement of load G_L is λ times as the stack displacement in the *exhaustion* stage. F_{out} and F_{in} are respectively the force acting on the stack in the *exhaustion* stage and *intake* stage. The area marked by **Work1** is the work done by the actuator and the area marked by **Work2** is the work done to the load in each cycle.

The work can be calculated analytically by the characteristics equation we derived

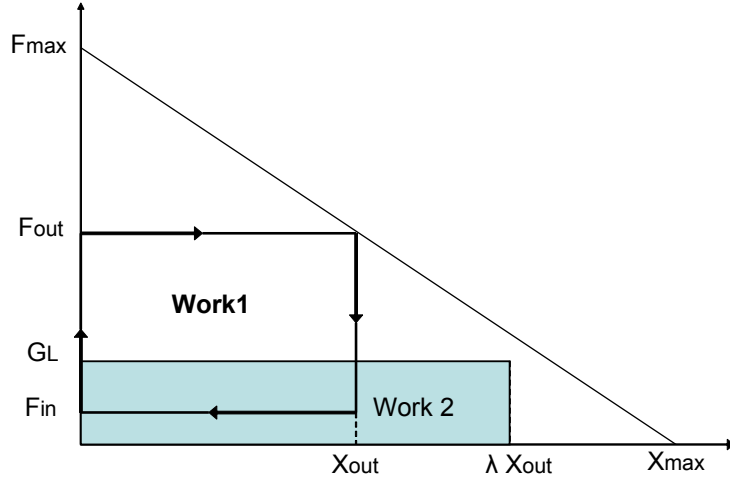


Figure 3.3: Mechanical work of the stack and load

in the former paragraphs: Equations (3.8) and (3.10)

$$F_{in} = P_{acc} A_{ch} \quad (3.15)$$

$$F_{out} = P_{acc} A_{ch} \gamma + G_L \lambda \quad (3.16)$$

$$x_{out} = x_0 V_{max} - \frac{P_{acc} A_{ch} \gamma + G_L \lambda}{K_a} \quad (3.17)$$

The work W_a done by the stack actuator in each cycle can be calculated by

$$\begin{aligned} W_a &= (F_{out} - F_{in}) x_{out} \\ &= (P_{acc} A_{ch} (\gamma - 1) + G_L \lambda) \left(x_0 V_{max} - \frac{P_{acc} A_{ch} \gamma + G_L \lambda}{K_a} \right) \end{aligned} \quad (3.18)$$

The work W_L done to the load in each cycle can be calculated by

$$\begin{aligned} W_L &= \lambda x_{out} G_L \\ &= \lambda G_L \left(x_0 V_{max} - \frac{P_{acc} A_{ch} \gamma + G_L \lambda}{K_a} \right) \end{aligned} \quad (3.19)$$

Thus the mechanical efficiency of the system can be calculated by

$$\begin{aligned} \eta_m &= \frac{W_L}{W_a} = \frac{G_L \lambda}{G_L \lambda + P_{acc} A_{ch} (\gamma - 1) + G_L \lambda} \\ &= \frac{1}{1 + \frac{\gamma - 1}{\lambda} \frac{P_{acc} A_{ch}}{G_L}} \end{aligned} \quad (3.20)$$

The mechanical efficiency η_m calculated by Equation (3.20) is always less or equal to one. Several cases can be discussed:

1. For a double-ended cylinder, we have $\gamma = 1$. No matter whether pre-pressure is applied the efficiency is always one.

2. For a single-ended cylinder, we have $\gamma > 1$. The efficiency is less than one if a pre-pressure is applied. If the pre-pressure is zero, the efficiency is equal to be one.

Although this model assumes an inviscid incompressible fluid, we find that in the single-ended cylinder case, when pre-pressure applied to the system, the mechanical efficiency is less than one. This is because the area difference of the two sides of the cylinder piston, when the load moves, less fluid flows into the high side of the cylinder than the fluid flow to the accumulator, thus extra work is needed to pump the fluid to compress the gas in the accumulator. In the double-end case, the volume flows into the high side is equal to the volume flows out the low side of the hydraulic cylinder, thus the work done by the stack is completely transfer to the load.

For a typical single-ended cylinder, the diameter of rod is usually half the diameter of the cylinder, which indicates $\gamma = \frac{4}{3}$. If we assume the diameter of the chamber is the same of the diameter of the bore of cylinder, we have $\lambda = \frac{4}{3}$. Let φ be defined to be the ratio of load to the force acting on the stack resulted from pre-pressure.

$$\varphi = \frac{G_L}{P_{acc} A_{ch}} \quad (3.21)$$

Figure 3.4 shows the mechanical efficiency for different value of φ . When $\varphi = 1$, the efficiency is 0.8 and for low values of φ the efficiency decreases. In order to achieve good efficiency, higher load to pre-pressure ratio is desired when using single-ended cylinder.

The output power of the system is the product of work done to the load in each period W_l and the operating frequency f .

$$Power = W_L f = \lambda G_L \left(x_0 V_{max} - \frac{P_{acc} A_{ch} \gamma + G_L \lambda}{K_a} \right) f \quad (3.22)$$

In the above equation, $x_0 V_{max}$ is the maximum free stroke x_{max} . To simplify further, we define the normalized load ζ and normalized pre-pressure ι to be

$$\zeta = \frac{G_L}{K_a x_{max}} \quad (3.23)$$

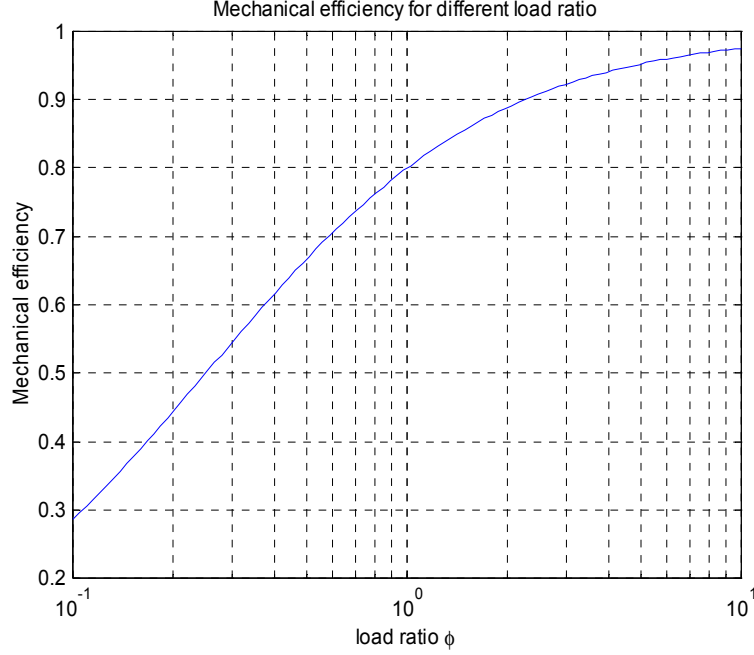


Figure 3.4: Efficiency of a single-ended cylinder

$$\iota = \frac{P_{acc} A_{ch}}{K_a x_{max}} \quad (3.24)$$

To ensure the stack be able to move the load, we must have limitations for the maximum load and pre-pressure, which results in $\zeta < 1$ and $\iota < 1$. Substitute Equations (3.23) and (3.24) into Equation (3.22) and rearrange it

$$\begin{aligned} Power &= K_a x_{max}^2 f (1 - \iota\gamma - \zeta\lambda) \zeta\lambda \\ &= K_a x_{max}^2 f \left(- \left(\zeta\lambda - \frac{(1 - \iota\gamma)}{2} \right)^2 + \frac{(1 - \iota\gamma)^2}{4} \right) \end{aligned} \quad (3.25)$$

In the above equation, the maximum power is

$$Power_{max} = \frac{K_a x_{max}^2 f}{4} (1 - \iota\gamma)^2 \quad (3.26)$$

and the maximum power condition is

$$2\zeta\lambda + \iota\gamma = 1 \quad (3.27)$$

For a given pre-pressure, Equation (3.27) determines the optimal load that maximize the output power. From the Equation (3.26), for a given pre-pressure, the maximum power will decrease as γ increases, which indicates that double-ended cylinder can deliver more power

than a single-end one. We also observe that the higher pre-pressure corresponds to lower maximum power. Let pre-pressure be zero, thus we obtain the maximum available power for a piezoceramic stack is

$$Power_{max} = \frac{K_a x_{max}^2 f}{4} \quad (3.28)$$

It represents the upper limit of the power that can be generated by the system. The maximum power is proportional to the square of the maximum stroke and to the stiffness, which means that to achieve higher output power, increasing the stroke while maintaining the same stiffness is more effective than increasing stiffness.

3.2.3 Summary

In this model, we assume an inviscid and incompressible fluid. Thus there is no energy loss by friction due to viscosity of the fluid, which may be considerably different from the real case. However, it represents the upper limit performance that is available. Furthermore, the model can provide some basic views for the power and efficiency analysis. Several points of the analytical results are summarized as following:

- In terms of both efficiency and power, the double-ended cylinders are better than single-ended ones. The mechanical efficiency of double-ended cylinders is always one while for the single-ended ones the mechanical efficiency decreases as pre-pressure increases.
- For a given pre-pressure, increasing the load will increase the mechanical efficiency.
- At a certain pre-pressure, there is an optimal load that maximizes the output power. And the maximum output power will decrease as pre-pressure increases.
- The output power is more sensitive with the maximum stroke than with stiffness of the stack actuator.
- The output power is proportional to the operating frequency.

3.3 The Incompressible Viscous Fluid (IVF) Model

This model will take into account the viscosity of the fluid while assuming an incompressible flow. The system is described by a four-stage operation model in the *Chapter 2*. In developing this flow model, we assume an incompressible flow in the open chamber operations: the *exhaustion* stage and *intake* stage, while the compressibility is considered in the closed chamber operations: the *compression* stage and *expansion* stage. The reason that the model is called incompressible is because we assume the fluid is incompressible in all stages where real flow occurs. We manage to avoid complex dynamic model, such as finite element models, and at the same time these simple models may provide accurate predictions of the system performance.

3.3.1 Calculation of the Reynolds Number

The energy analysis for the viscous flow in the *Chapter 2* shows the different flow characteristics for laminar flows and turbulent flows. For flow in pipes, the flow is laminar when Reynolds number $Re < 2000$ and flow is usually turbulent when Reynolds number $Re > 3000$. It is important to determine the Reynolds number for the flow in the actuation system.

For a fully developed steady flow in a pipe, the Reynolds number is defined by Equation (2.56).

$$Re = \frac{\bar{V}D}{\nu} \quad (3.29)$$

where \bar{V} is the average velocity, D is the diameter of the pipe and ν is the kinematic viscosity of the fluid. To determine the average velocity, a quasi-steady flow model will be defined. Figure 3.5 shows the diagram of the pumping chamber and the pipes connecting it. The velocity in the pipe V_p is determined by the hydraulic amplification and the fluid velocity in the chamber V_{ch} , which we assume is equal to the velocity of the stack actuator.

We assume that the stack expands at a constant velocity V_s

$$V_s = \frac{x_{max}}{t_s} \quad (3.30)$$

where t_s is the time duration of the expand, which can be calculated by dividing the duty cycle d_c of stack by operating frequency f

$$t_s = \frac{d_c}{f} \quad (3.31)$$

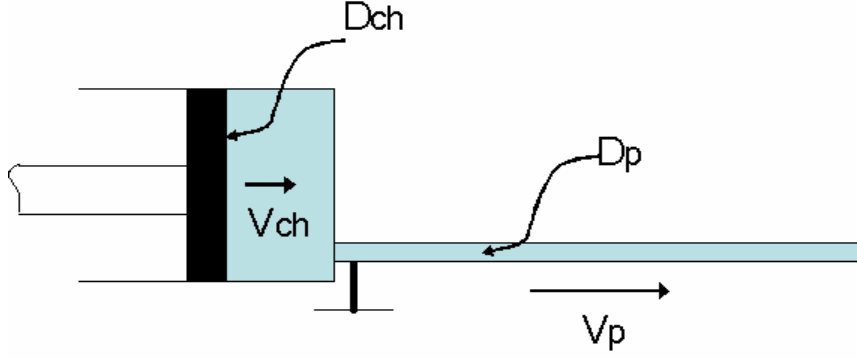


Figure 3.5: Diagram of fluid flow

Substituting Equation (3.31) and Equation (3.30) into the equation of Reynolds number definition, we have

$$\begin{aligned} Re &= \frac{\bar{V}D}{\nu} = \frac{x_{max}}{d_c \nu} \frac{A_{ch}}{A_p} D_p f \\ &= \frac{x_{max}}{d_c \nu} \frac{D_{ch}^2}{D_p} f \end{aligned} \quad (3.32)$$

If we define the critical frequency f_{cr} as the operating frequency that corresponds to Reynolds number $Re = 2000$, we have

$$f_{cr} = 2000 \frac{d_c \nu}{x_{max}} \frac{D_p}{D_{ch}^2} \quad (3.33)$$

In the experiment setup, we use the *EP Hydraulic Oil 32* as the hydraulic fluid because it is anti-wear hydraulic oil and good for high pressure applications. The viscosity of the fluid is $135 \sim 165$ SUS at $100^\circ F$. Here the average value of 150 SUS at $100^\circ F$ will be used for calculation. The SUS value can be converted into ISO standard unit by

$$SUS@100^\circ F / 5 = cST@40^\circ C = 10^{-6} m/s^2 \quad (3.34)$$

Thus the kinematic viscosity ν is

$$\nu = 3 \times 10^{-5} (m/s^2) \quad (3.35)$$

Table 3.1 shows the value of the parameters needed to determine the critical frequency f_{cr} . Substitute the values in the table into Equation (3.33), we obtain

$$f_{cr} = 960 Hz \quad (3.36)$$

Table 3.1: Parameters of the system.

d_c	$\nu(m/s^2)$	$x_{max}(\mu m)$	$D_p(mm)$	$D_{ch}(mm)$
0.5	3×10^{-5}	80	1.6	25

For operating frequency less than f_{cr} , we can assume that the fluid in the piezo-hydraulic system is laminar.

In this section, the critical frequency is determined by a quasi-steady flow model and flow pattern in the hydraulic system is determined. In the following sections, the viscous model will be derived and fluid equations will be presented for laminar flows.

3.3.2 Flow Equations

The flow equations will be presented for each stages respectively. Then, we can combine the equations in the four stages to describe the flow in one cycle.

At the beginning, the system is pre-pressurized to P_{acc} . The initial volume in the pumping chamber is \forall_0 and the displacement of the piston is 0. Then the system begins to operate by the four stage fashion. The states of stack can be completely determined with four states: displacement x , force F , voltage V and charges Q . However due to the two constitutive equations of stack actuator (Equation (2.3), (2.4)), there are only two independent states. For convenience, we choose the displacement x and the pressure in the chamber P as two states to analyze. Once P and x are determined, the other states can be calculated by Equation (2.3) and (2.4). To be general, we will choose one of the cycle, not the first cycle, to begin with analysis. The reason is that after a cycle of four stage operation, the system does not must return to the initial states, which is the case for the IIF model discussed in the former section.

Compression Stage

In this analysis, we assume that the bulk modulus of the fluid β is a constant. Figure 3.6 shows the diagram for the *compression* stage. We assume the initial states of that cycle are $P = P_1$ and $x = x_1$, which could be different from the accumulator pressure and zero

position.

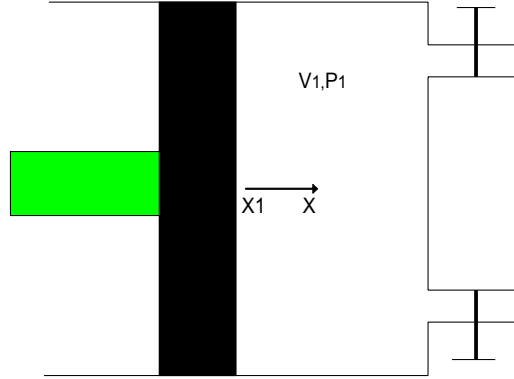


Figure 3.6: Diagram of compression stage

The volume of fluid in the chamber can be determined by the position of piston x

$$\begin{aligned} \forall &= \forall_0 - A_{ch} x \\ \Delta \forall &= -\Delta x A_{ch} \end{aligned} \quad (3.37)$$

Substitute into Equation (4.1), we have

$$\beta = \frac{dP}{-dx A_{ch} / (\forall_0 - A_{ch} x)} \quad (3.38)$$

Rearrange it we have

$$dP = \beta \frac{A_{ch}}{\forall_0 - A_{ch} x} dx \quad (3.39)$$

Integrating the above equation and substituting in the initial conditions, we have

$$\int_{P_1}^P dP = \int_{x_1}^x \beta \frac{A_{ch}}{\forall_0 - A_{ch} x} dx \quad (3.40)$$

Simplify and rearrange it, we obtain the pressure as a function of the displacement of the piston

$$P = P_1 - \beta \ln \frac{\frac{\forall_0}{A_{ch}} - x}{\frac{\forall_0}{A_{ch}} - x_1} \quad (3.41)$$

If pressure or displacement is given, the other can be calculated by Equation (3.41). Then by using the constitutive equation of the stack actuator we can determine the voltage and charge of the stack.

Exhaustion Stage

We assume the initial states of the stage is $x = x_2$ and $P = P_2$. In this stage, the fluid is pumped from the pumping chamber into the high side of the cylinder. And the piston in the cylinder pushes the fluid to flow into the accumulator. Figure 3.1 shows the setup of the system.

In the former chapter, we derived the energy equation for a steady viscous flow as Equation (2.55). For a laminar flow, the velocity coefficient $\alpha = 2$. And we assume no extra shaft work is added into the flow such that $h_w = 0$. We neglect the height differential in the system, thus the energy equation is simplified to be

$$\left(\bar{V}_1^2 + \frac{p_1}{\rho}\right) - \left(\bar{V}_2^2 + \frac{p_2}{\rho}\right) = h_l \quad (3.42)$$

To apply the above energy equation, special control volumes are chosen as the dash lines in Figure 3.7. The control volume CV_1 is chosen such that the left section is enough near from the piston in the pumping chamber and the upper section is enough near from the piston in the cylinder and else where is the same as the inner surface of the pumping chamber, pipes and single-ended cylinder. The control volume CV_2 is chosen such that the bottom section is enough near from the piston in the single-ended chamber and the upper section is enough near from free surface in the accumulator and elsewhere is the same as the inner surface of the accumulator, pipes and single-ended cylinder.

For the control volume CV_1 , because the left section is very close to the piston, we can assume the average velocity at that section is the same as the velocity of the piston \dot{x} and the pressure P at the section is same as the pressure at the surface of the piston. For the same reason, we assume the velocity at the above section of CV_1 is the same as the velocity of the piston in the hydraulic cylinder and the pressure P_{ca} is the same as the pressure at the bottom surface of the piston. For the control volume CV_2 , we also have that the velocity at the bottom section is the same as the velocity of the piston in the hydraulic cylinder and the pressure at that section P_{cb} is the same as the pressure at the upper surface of the piston in the cylinder. The velocity at the top section of CV_2 is assumed to be constant and the pressure at that section is the same as the pressure of the gas P_{acc} .

To apply Equation (3.42) into control volume CV_1 , the head losses h_l should be determined. Because the cross section area of the pumping chamber and hydraulic cylinder is much larger than the pipe, the friction in the cylinder and pumping chamber is much

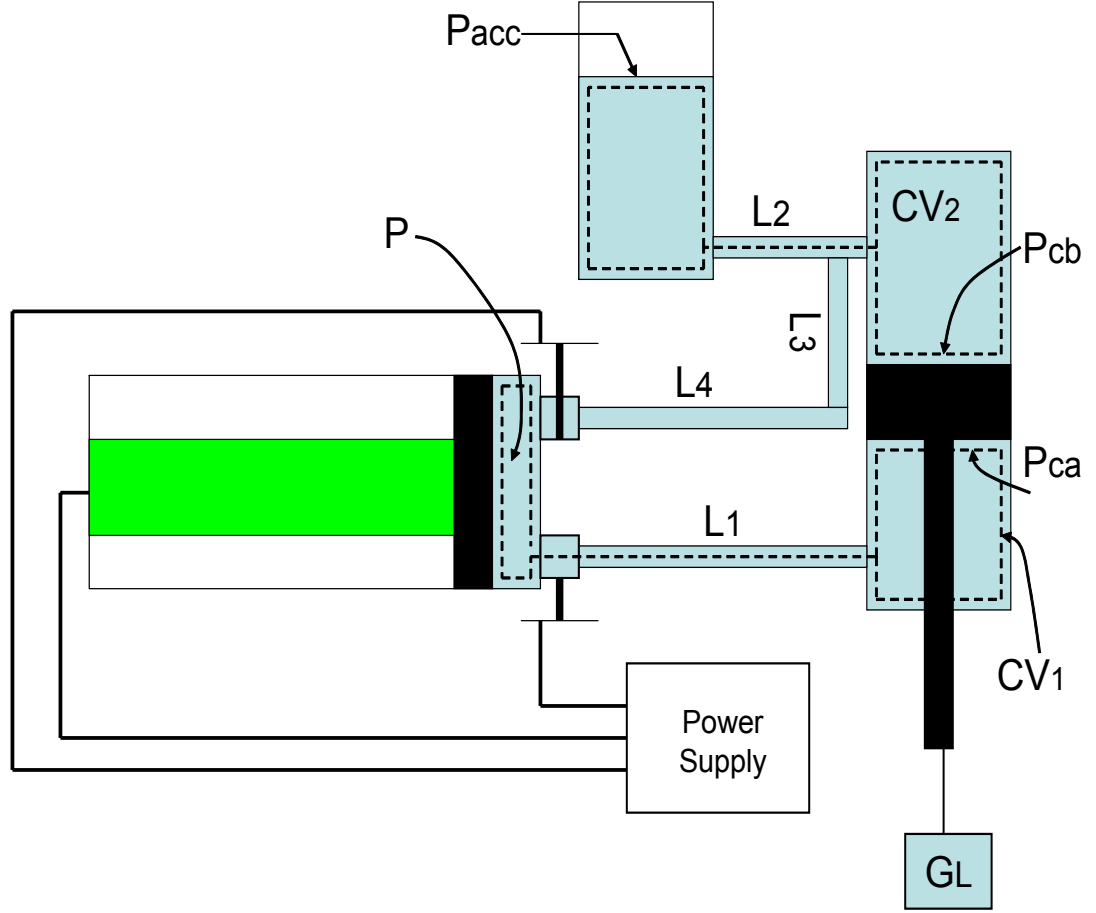


Figure 3.7: Control volumes of the flow

less than the friction in the pipe. Thus when calculating the major losses, we only compute the losses in the pipes. As shown in Figure 3.7, the effective pipe length for CV_1 is L_1 . Substitute in Equation (2.65), the major losses are

$$h_{major} = \left(\frac{64}{Re} \right) \frac{L_1}{D} \frac{\bar{V}^2}{2} \quad (3.43)$$

The major losses factor K_{Lma} is

$$K_{lma} = \left(\frac{64}{Re} \right) \frac{L_1}{D} \quad (3.44)$$

As the diagram shown in Figure 3.7, there is a sudden contraction between the chamber and pipe and a sudden expansion between the pipe and the cylinder in control volume CV_1 . In addition, the active valves are equivalent to gate valves. The orifice in the valves are larger than the section area of the pipes, which also results in a sudden expansion

and sudden contraction. The loss factor of the sudden contraction and expansion can be calculated by Equation (2.69) and (2.70). We denote the total minor losses factor in CV_1 by K_{Lmi} .

The total head losses are

$$h_l = (K_{Lma} + K_{Lmi}) \frac{\bar{V}^2}{2} = K_{L1} \frac{\bar{V}^2}{2} \quad (3.45)$$

where \bar{V} is the average velocity in the pipes. Substitute it into Equation (3.42), we have

$$\left(\dot{x}^2 + \frac{P}{\rho} \right) - \left(V_L^2 + \frac{P_{ca}}{\rho} \right) = K_{L1} \frac{\bar{V}^2}{2} \quad (3.46)$$

where \dot{x} is the velocity of the piston in the pumping chamber, V_L is the velocity of load, which is the same as the velocity of piston in the cylinder. Apply conservation of mass for the steady flow, we have

$$\dot{x} = \frac{V_L}{\lambda} = \bar{V} \frac{A_p}{A_{ch}} \quad (3.47)$$

We denote the amplification ϵ by

$$\epsilon = \frac{A_{ch}}{A_p} \quad (3.48)$$

Substitute Equation (3.47) and (3.48) into Equation (3.46) and rearrange

$$P - P_{ca} = \left(\frac{\epsilon^2 K_{L1}}{2} + \lambda^2 - 1 \right) \rho \dot{x}^2 \quad (3.49)$$

In the same manner, we can derive the flow equation for the control volume CV_2 . As shown in Figure 3.7, the effective pipe length for CV_2 is L_2 . Substitute in Equation (2.65), the major losses are

$$h_{major} = \left(\frac{64}{Re} \right) \frac{L_2}{D} \frac{\bar{V}^2}{2} \quad (3.50)$$

The major losses factor K_{Lma} is

$$K_{Lma} = \left(\frac{64}{Re} \right) \frac{L_2}{D} \quad (3.51)$$

As the diagram shown in Figure 3.7, there is sudden contraction between the cylinder and pipe and a sudden expansion between the pipe and the accumulator in control volume CV_2 . In addition, there is a **T** fitting, whose losses are defined by Equation (2.71). The losses factor of the sudden contraction and expansion can be calculated by Equation (2.69)

and (2.70). We denotes the total minor losses factor in CV_2 by K_{Lmi} , which is the sum of the minor losses in each parts.

The total head losses are

$$h_l = (K_{Lma} + K_{Lmi}) \frac{\bar{V}^2}{2} = K_{L2} \frac{\bar{V}^2}{2} \quad (3.52)$$

where \bar{V} is the average velocity in the pipes. Substitute it into Equation (3.42), we have

$$\left(V_L + \frac{P_{cb}}{\rho} \right) - \left(V_a^2 + \frac{P_{acc}}{\rho} \right) = K_{L2} \frac{\bar{V}^2}{2} \quad (3.53)$$

where V_a is the average velocity of at the surface of the accumulator. Because the cross section area of the accumulator is much bigger than the cylinder, we assume $V_a = 0$. Apply conservation of mass for the steady flow, we have

$$\frac{V_L}{\bar{V}} = \frac{A_p}{A_{cy}} = \frac{A_p}{A_{ch}} \frac{A_{ch}}{A_{cy}} = \frac{\lambda}{\gamma \epsilon} \quad (3.54)$$

Substitute the above equation into Equation (3.53) and rearrange it,

$$P_{cb} - P_{acc} = \left(\frac{\gamma^2 \epsilon^2}{2\lambda^2} K_{L2} - 1 \right) \rho V_L^2 \quad (3.55)$$

Equation (3.49) and (3.55) is respectively the energy equations for control volume CV_1 and CV_2 , which is interconnected by the piston in the cylinder. Figure 3.8 shows the free body diagram of the piston in the cylinder. Thus we have

$$\begin{aligned} P_{ca} \frac{A_{cy}}{\gamma} &= P_{cb} A_{cy} + G_L \\ P_{ca} - \gamma P_{cb} &= \gamma \frac{G_L}{A_{cy}} \end{aligned} \quad (3.56)$$

To eliminate P_{ca} and P_{cb} , solve together Equations (3.49), (3.55) and (3.56), we have

$$P = \gamma P_{acc} + \left(\frac{\epsilon^2 K_{L1}}{2} + \lambda^2 - 1 \right) \rho \dot{x}^2 + \gamma \left(\frac{\gamma^2 \epsilon^2}{2\lambda^2} K_{L2} - 1 \right) \rho V_L^2 + \gamma \frac{G_L}{A_{cy}} \quad (3.57)$$

Substitute $V_L = \lambda \dot{x}$ into the above equation and simplify it, we have

$$\begin{aligned} P &= \gamma P_{acc} + \Omega \rho \dot{x}^2 + \gamma \frac{G_L}{A_{cy}} \\ \Omega &= \left(\frac{\epsilon^2}{2} (K_{L1} + \gamma^3 K_{L2}) - (\gamma - 1) \lambda^2 - 1 \right) \end{aligned} \quad (3.58)$$

Equation (3.58) shows the pressure in the pumping chamber is a function of the velocity of the piston. To solve the equation, we can use the characteristics equation of stack. Differentiate Equation (2.3) and substitute $F = P A_{ch}$ into it

$$\dot{x} = x_0 \dot{V} - \frac{A_{ch}}{K_a} \dot{P} \quad (3.59)$$

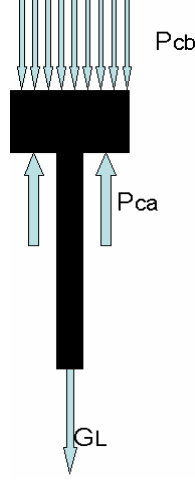


Figure 3.8: Free body diagram of piston in the cylinder

Because the impedance of a piezoceramic stack is similar to a capacitor. We have

$$\begin{aligned} V &= \frac{1}{C} \int i dt \\ \dot{V} &= \frac{i}{C} \end{aligned} \quad (3.60)$$

where C is the equivalent capacitance of the stack. Substitute Equation (3.60) into Equation (3.59), we have

$$\dot{x} = \frac{x_0 i}{C} - \frac{A_{ch} \dot{P}}{K_a} \quad (3.61)$$

Substitute it into Equation (3.58) and rearrange it

$$\dot{P} = -\frac{K_a}{A_{ch}} \sqrt{\frac{1}{\Omega \rho} \left(P - \gamma \left(P_{acc} + \frac{G_L}{A_{cy}} \right) \right)} + \frac{x_0 K_a}{C A_{ch}} i \quad (3.62)$$

For a current controlled stack, the input current i of the stack depends on the characteristic of the power supply. For example, the power supply from DSM always outputs the maximum current I_{max} . We can solve the differential equation of the pressure in Equation (3.62) if the dynamics of the input current is known. Equation (3.61) can be used to calculate the displacement of the stack once the pressure is solved. Finally the displacement of the load can be obtained by $x_L = \lambda x$.

Expansion Stage

During the expansion stage, the stack contracts while both valves are closed. We assume the initial pressure is P_3 and initial displacement x_3 . Equation (3.39) can also be applied

in this stage. Integrate it and simplify, we have

$$P = P_3 - \beta \ln \frac{\frac{\forall_0}{A_{ch}} - x}{\frac{\forall_0}{A_{ch}} - x_3} \quad (3.63)$$

Intake Stage

In the intake stage, the inlet valve opens and the fluid flows from the accumulator into the pumping chamber. This stage is similar to the exhaustion stage. Control volume will be used to analyze the fluid flow. Figure 3.9 shows the control volume CV_3 in dashed lines. The control volume is chosen such that the upper section is very near to the free surface of the accumulator that the velocity and pressure at that section is the same as the free surface, and the left section of the control volume is very close to the piston that the velocity and pressure at that section can be assumed to be the same as the velocity and pressure at the surface of the piston, and the boundaries of the control volume elsewhere are the inner surface of the accumulator, pipes and the pumping chamber.

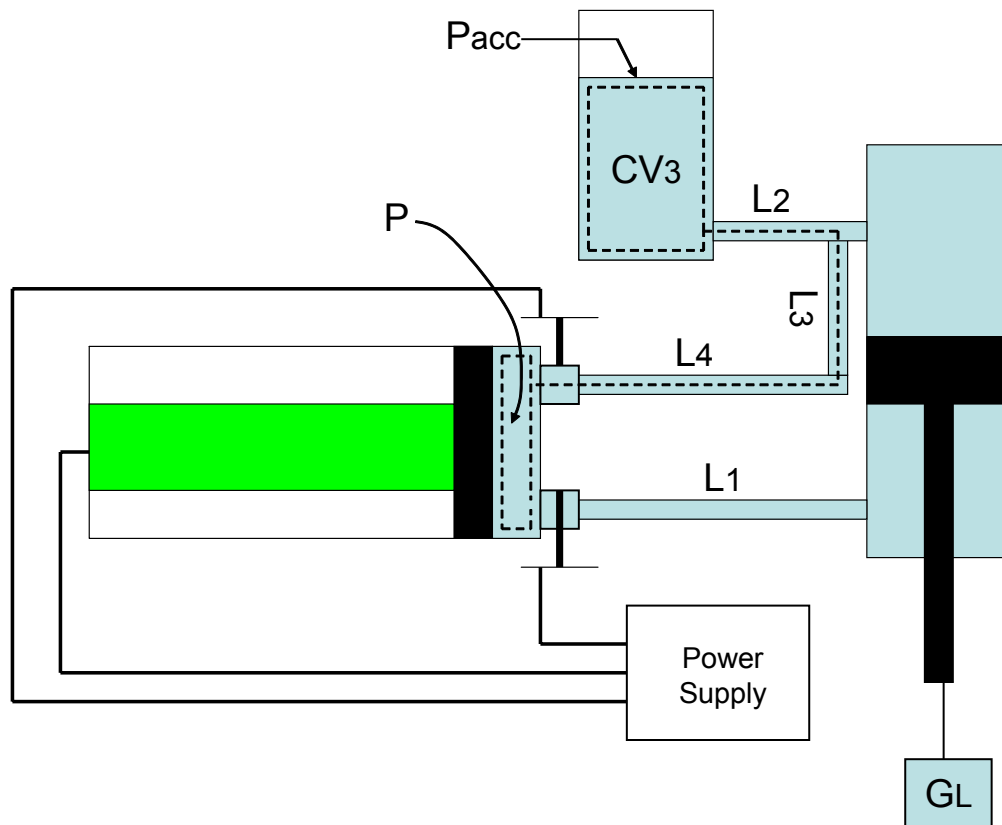


Figure 3.9: Control volume in the intake stage

As shown in Figure 3.9, the effective pipe length for CV_2 is $L_2 + L_3 + L_4$. Substitute it in Equation (2.65), the major losses are

$$h_{major} = \left(\frac{64}{Re} \right) \frac{L_2 + L_3 + L_4}{D} \frac{\bar{V}^2}{2} \quad (3.64)$$

The major losses factor K_{Lma} is

$$K_{Lma} = \left(\frac{64}{Re} \right) \frac{L_2 + L_3 + L_4}{D} \quad (3.65)$$

As the diagram shown in Figure 3.7, there is a sudden contraction between the accumulator and pipe and a sudden expansion between the pipe and the chamber in control volume CV_3 . In addition, there is a **T** fittings, whose branch run losses are defined by Equation (2.71). Because the orifice of the active valves are larger than the cross section of the valve, the losses in the valve can be approximated by a pair of sudden expansion and sudden contraction. The losses factor of the sudden contraction and expansion can be calculated by Equation (2.69) and (2.70). We denotes the total minor losses factor in CV_3 by K_{Lmi} , which is the sum of the minor losses in each parts.

The total head losses are

$$h_l = (K_{Lma} + K_{Lmi}) \frac{\bar{V}^2}{2} = K_{L3} \frac{\bar{V}^2}{2} \quad (3.66)$$

where \bar{V} is the average velocity in the pipes. Substitute it into Equation (3.42), we have

$$\left(V_a^2 + \frac{P_{acc}}{\rho} \right) - \left(\dot{x}^2 + \frac{P}{\rho} \right) = K_{L3} \frac{\bar{V}^2}{2} \quad (3.67)$$

Because the cross section area of the accumulator is much bigger than the cylinder, we assume $V_a = 0$. Apply conservation of mass for the steady flow, we have

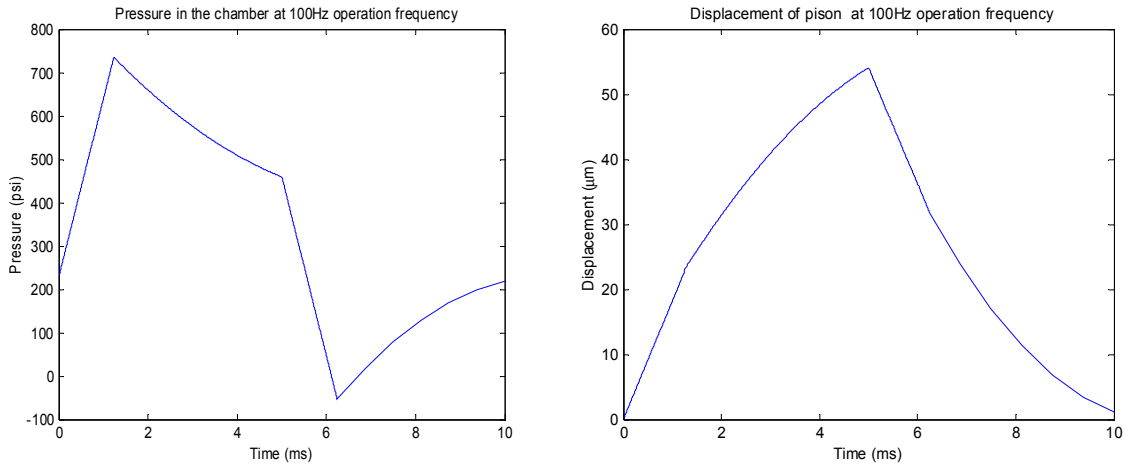
$$\begin{aligned} P_{acc} - P &= \Theta \rho \dot{x}^2 \\ \Theta &= \left(\frac{\epsilon^2 K_{L3}}{2} + 1 \right) \end{aligned} \quad (3.68)$$

Substitute Equation (3.61) into the above equation and simplify, we have

$$\dot{P} = \frac{K_a}{A_{ch}} \sqrt{\frac{1}{\Theta \rho} (P_{acc} - P)} + \frac{x_0}{C} \frac{K_a}{A_{ch}} i \quad (3.69)$$

In the same manner, we can calculate the pressure P and displacement of the piston x if the input current i is known.

In the above sections, the flow equation in each stage is derived given the initial conditions. Thus, the operations of the system can be modeled by combining these equations. Figure 3.10 shows the simulation results in one cycle of the IVF model.



(a) Pressure in chamber

(b) Displacement of piston

Figure 3.10: IVF Simulation at 100 Hz under 6.84 Kg load

3.3.3 Summary

In the IVF model, we assume a viscous incompressible flow. The viscosity is taken into account in order to energy loss in the hydraulic components. Reynolds number is computed to determine the flow in the system. The flow equations in each stage is derived based on the energy equations derived in the previous chapter. By assuming the fluid is incompressible, the IVF model is described by only one first order differential equation and is easy to solve.

3.4 The Compressible Viscous Fluid (CVF) Model

In this model, compressibility of the fluid will be modeled in the full cycle of the four stages. Because in the development of the IVF model, we already assumed compressibility in the *compression* stage and *expansion* stage, equations of motion of IVF model in these two stages are the same for CVF model. Thus, we only need to derive the flow equations for the *exhaustion* stage and *intake* stage.

3.4.1 Equations for The Exhaustion Stage

In the analysis of the IVF model presented in the previous section, the flow is divided into closed volumes by the piston in the hydraulic cylinder and for each flow control volumes are chosen and energy equations are applied to calculate the system response. In this section,

the approach is different in terms of dividing the flow. The system is considered as six components of fluid as shown in Figure 3.11.

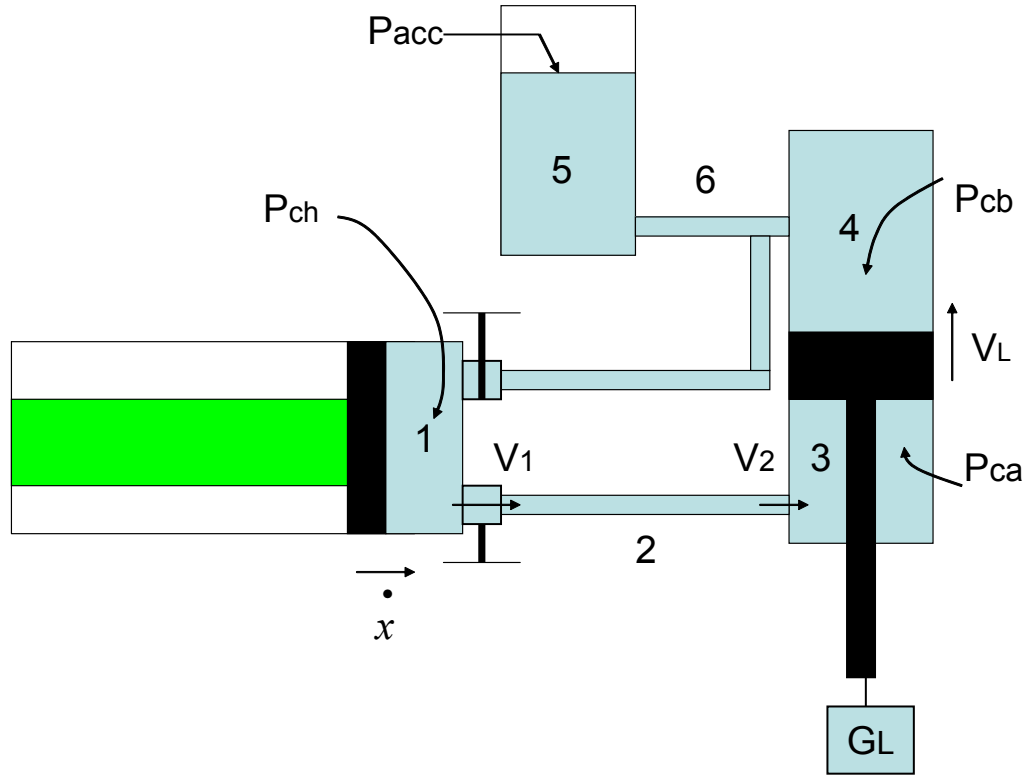


Figure 3.11: Diagram of system used to develop CVP model.

To maintain the simplicity of the model, assumptions and approximations are made based on observation of the test setup. First assumption is that we assume energy losses, including major losses and minor losses only exist in the pipes, fittings and valves. There are no energy losses in large volume components, such as the pumping chamber, hydraulic cylinder and accumulator. It is justified that for a large section the Reynolds number is much smaller than the small area section, which means the friction due to viscous flow is much less. Secondly, we assume compressibility of fluid only occurs in pumping chamber and high side of the cylinder, which corresponds to part 1 and 3 respectively in Figure 3.11. We neglect the compressibility in component 4. The reason is that it is directly connected with the accumulator, which means the pressure variation is small and thus we can consider the density is constant. Because the cross section area of pipe is very small and the length of pipe in part 2 is made short as possible to reduce energy losses, we can assume the fluid

volume in the pipe is relatively small compared to the volume in the pumping chamber and hydraulic cylinder. Thus we neglect the mass changes of fluid in pipes of component 2.

The density-pressure relationship of fluid can be derived from the definition of bulk modulus in Equation (4.1). For a closed volume of fluid, we have

$$\forall = \frac{m}{\rho} \quad (3.70)$$

Differentiating the above equation and assuming constant mass, yields

$$d\forall = -\frac{m d\rho}{\rho^2} \quad (3.71)$$

Substitute Equations (3.70) and (3.71) into Equation (4.1), we have

$$\frac{d\rho}{\rho} = \frac{1}{\beta} P \quad (3.72)$$

Integrating it yields

$$\rho = \exp\left(\frac{P}{\beta}\right) + C \quad (3.73)$$

We assume the initial pressure is accumulator pressure P_0 and initial density is ρ_0 . The integral constant C can be solved by substituting initial conditions into Equation (3.73).

$$\rho = \rho_0 \exp\left(\frac{P - P_0}{\beta}\right) \quad (3.74)$$

Thus we get the pressure-density relationship of the compressible fluid. For a given fluid, the bulk modulus is given and initial conditions is known. The density is only dependent on pressure.

Differentiating the definition of density $\rho = \frac{m}{\forall}$ yields

$$\begin{aligned} \dot{\rho} &= d\left(\frac{m}{\forall}\right)/dt \\ &= \frac{\dot{m}}{\forall} - \frac{m \dot{\forall}}{\forall^2} \\ &= \frac{\dot{m} - \rho \dot{\forall}}{\forall} \end{aligned} \quad (3.75)$$

The above equation shows the change of density is resulted from two factors: one is the mass flow into or out from the volume and the other one is the volume change of the fluid. When deriving Equation (3.74) and (3.75), we did not make approximations, and thus they can be used in any compressible fluid.

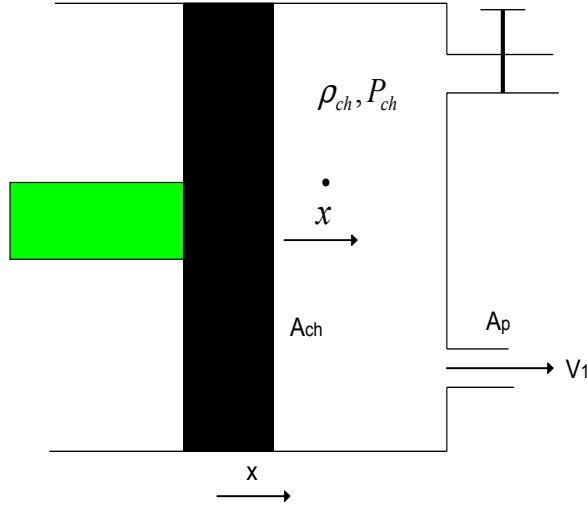


Figure 3.12: Diagram of chamber for CVP model.

The flow equations of the system in Figure 3.11 is derived by analyzing each component. Figure 3.12 shows the diagram of pumping chamber with the stack pushing the fluid out through the open outlet valve.

For the volume of fluid in the pumping chamber, the mass flow out of chamber is

$$\dot{m} = \rho V_1 A_p \quad (3.76)$$

The volume change of the fluid is

$$\dot{V} = -\dot{x} A_{ch} \quad (3.77)$$

It is noted the minus sign in the above equation is because we define that a positive of displacement x corresponds to a decreasing volume. Substitute Equations (3.76) and (3.77) into Equation (3.75) to yield

$$\dot{\rho}_{ch} = \frac{\rho_{ch}}{A_{ch}} \frac{-V_1 A_p + \dot{x} A_{ch}}{L_0 - x} \quad (3.78)$$

In order to simplify the equations, we define the area ratios in the system as following

$$\begin{aligned} \lambda &= \frac{A_{ch}}{A_{cy}} \gamma \\ \epsilon &= \frac{A_{ch}}{A_p} \end{aligned} \quad (3.79)$$

where γ is the area ratio of the area of low side of the cylinder to the high side. These definitions are same as when developing the IIF model. Then Equation (3.78) could be

simplified as

$$\rho_{ch} = \rho_{ch} \frac{-\frac{V_1}{\epsilon} + \dot{x}}{L_0 - x} \quad (3.80)$$

where V_1 is the velocity of fluid entering the pipe.

The density of fluid in the pumping chamber could be calculated by Equation (3.74)

$$\rho_{ch} = \rho_0 \exp\left(\frac{P_{ch} - P_0}{\beta}\right) \quad (3.81)$$

Because the bulk modulus of fluid is far larger than pressures in the fluid, the value of $\frac{P_{ch} - P_0}{\beta}$ is far less than one. Thus the above equation can be approximated with the first order term by Taylor series

$$\rho_{ch} = \rho_0 \left(1 + \frac{P_{ch} - P_0}{\beta}\right) \quad (3.82)$$

For the cylinder in Figure 3.13, applying Equation (3.75) yields

$$\begin{aligned} \rho_{ca} &= \frac{\dot{m} - \rho_{ca} \nabla}{\nabla} \\ &= \frac{\rho_{ca} A_p V_2 - \rho_{ca} V_L A_{cy}}{A_{cy} x_L} \\ &= \rho_{ca} \frac{\frac{V_2 \lambda}{\epsilon} + V_L}{x_L} \end{aligned} \quad (3.83)$$

where V_2 is the velocity of fluid flowing out of pipe. The density to pressure relationship in Equation (3.74) is also valid

$$\rho_{ca} = \rho_0 \exp\left(\frac{P_{ca} - P_0}{\beta}\right) \quad (3.84)$$

Simplifying the exponential term by the linear term yields

$$\rho_{ca} = \rho_0 \left(1 + \frac{P_{ca} - P_0}{\beta}\right) \quad (3.85)$$

For the pipe, component 2 as in Figure 3.11, the flow will be approximated with a fully-developed quasi-static flow. The energy equations presented in the previous chapter is hold. The losses include the major losses in the pipe and minor losses at the orifice at the intersection of chamber and pipe, the valve orifice, piping turns and orifice at the hydraulic cylinder. The energy equation of component 2 becomes

$$V_1^2 + \frac{P_{ch}}{\rho_{ch}} = V_2^2 + \frac{P_{ca}}{\rho_{ca}} + K_{L1} \frac{\bar{V}}{2}, \quad (3.86)$$

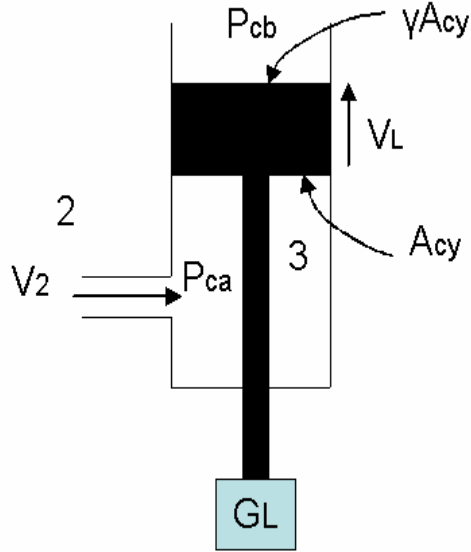


Figure 3.13: Diagram of hydraulic cylinder for CVF model.

where V_1 and V_2 is the velocity of fluid entering and flowing out of pipe, K_{L1} is the total loss factor in the pipe and \bar{V} is the average velocity in the pipe, which is defined by $\bar{V} = \frac{V_1+V_2}{2}$. Applying the mass conservation law on the pipe yields

$$V_1 \rho_{ch} = V_2 \rho_{ca} \quad (3.87)$$

The motion of load can be computed by the free body diagram of the piston. We neglect the dynamics of the string by which load is attached at the piston of the hydraulic cylinder. As shown in Figure 3.13, the motion of equation of load is

$$\frac{G_L}{g} \ddot{x}_L A_{cy} = P_{ca} A_{cy} - P_{cb} \gamma A_{cy} - G_L A_{cy} \quad (3.88)$$

Simplifying the equation yields

$$P_{ca} = (P_{cb} + \frac{G_L (1 + \frac{\ddot{x}_L}{g})}{A_{cy}}) \gamma \quad (3.89)$$

The flow from the low side of cylinder to the accumulate in Figure 3.11 is approximated by a fully developed quasi-static incompressible flow. This is justified by that because the low side is directly connected with the accumulator thus the dynamic pressure is relative small and density change is also small. Applying the energy equation Equation (3.42) into this volume yields

$$P_{cb} = P_{acc} + K_{L2} \rho_0 V_L^2 (\frac{\epsilon \gamma}{\lambda})^2 \quad (3.90)$$

The motion of stack can be described by

$$x = x_0 V - \frac{F}{k_a} \quad (3.91)$$

where x_0 is the voltage-to-displacement coefficient, V is the applied voltage, F is the force and k_a is the stiffness of the stack. Differentiate the above equation and simplify to yield

$$\dot{x} = \frac{x_0 i}{C} - \frac{A_{ch}}{k_a} \dot{P}_{ch}, \quad (3.92)$$

where i is the current input of stack, which is dependent on the characteristics of the power source.

In the above section, we analyzed the equation of each component of the system (Equation 3.80, 3.82, 3.83, 3.85, 3.86, 3.87, 3.89, 3.90, 3.92). The system can be described by integrating the coupled equations as an equation array:

$$\dot{\rho}_{ch} = \rho_{ch} \frac{-\frac{V_1}{\epsilon} + \dot{x}}{L_0 - x} \quad (3.93)$$

$$\rho_{ch} = \rho_0 \left(1 + \frac{P_{ch} - P_0}{\beta}\right) \quad (3.94)$$

$$\dot{\rho}_{ca} = \rho_{ca} \frac{\frac{V_2 \lambda}{\epsilon} + \dot{x}_L}{x_L} \quad (3.95)$$

$$\rho_{ca} = \rho_0 \left(1 + \frac{P_{ca} - P_0}{\beta}\right) \quad (3.96)$$

$$V_1^2 + \frac{P_{ch}}{\rho_{ch}} = V_2^2 + \frac{P_{ca}}{\rho_{ca}} + K_{L1} \frac{(V_1 + V_2)^2}{8} \quad (3.97)$$

$$V_1 \rho_{ch} = V_2 \rho_{ca} \quad (3.98)$$

$$P_{ca} = \left(P_{cb} + \frac{G_L (1 + \frac{\dot{x}_L}{g})}{A_{cy}}\right) \gamma \quad (3.99)$$

$$P_{cb} = P_{acc} + K_{L2} \rho_0 \dot{x}_L^2 \left(\frac{\epsilon \gamma}{\lambda}\right)^2 \quad (3.100)$$

$$\dot{x} = \frac{x_0 i}{C} - \frac{A_{ch}}{k_a} \dot{P}_{ch} \quad (3.101)$$

There are nine unknowns in the above equations: ρ_{ch} , ρ_{ca} , P_{ch} , P_{ca} , P_{cb} , V_1 , V_2 , x and x_L , which is equal to the number of equations. Thus this system can be solved by these equations. In order to reduce the complexity of the model, further simplification will be carried on before numerical simulations. It is noticed the unknown variables P_{ca} , P_{cb} , x and x_L are of more interests in terms of calculating the performance and power efficiency. Thus we will eliminate the other unknowns from the array of equations.

Differentiating Equation (3.94) with time and substituting in Equation (3.93) yields

$$\frac{\rho_0 \dot{P}_{ch}}{\beta} = \rho_0 \left(1 + \frac{P_{ch} - P_0}{\beta}\right) \frac{-\frac{V_1}{\epsilon} + \dot{x}}{L_0 - x} \quad (3.102)$$

Rearranging it yields

$$V_1 = \left(\dot{x} - \frac{\dot{P}_{ch}}{\beta + P_{ch} - P_0} (L_0 - x)\right) \epsilon \quad (3.103)$$

Because P_{ch} and P_0 is far smaller than β , we approximate $\beta + P_{ch} - P_0$ with β . Thus Equation (3.103) becomes

$$V_1 = \left(\dot{x} - \frac{\dot{P}_{ch}}{\beta} (L_0 - x)\right) \epsilon \quad (3.104)$$

Differentiating Equation (3.96) with time and substituting in Equation (3.95) yields

$$\frac{\rho_0 \dot{P}_{ca}}{\beta} = \rho_0 \left(1 + \frac{P_{ca} - P_0}{\beta}\right) \frac{\frac{V_2 \lambda}{\epsilon} + \dot{x}_L}{x_L} \quad (3.105)$$

Rearranging it yields

$$V_2 = \left(\dot{x}_L + \frac{\dot{P}_{ca}}{\beta + P_{ca} - P_0} x_L\right) \frac{\epsilon}{\lambda} \quad (3.106)$$

In the same manner, we approximate $\beta + P_{ca} - P_0$ with β to yield

$$V_2 = \left(\dot{x}_L + \frac{\dot{P}_{ca}}{\beta} x_L\right) \frac{\epsilon}{\lambda} \quad (3.107)$$

Substitute Equation (3.94) and (3.96) into Equation (3.98) to yield

$$\begin{aligned} V_1 \rho_0 \left(1 + \frac{P_{ch} - P_0}{\beta}\right) &= V_2 \rho_0 \left(1 + \frac{P_{ca} - P_0}{\beta}\right) \\ \frac{V_1}{V_2} &= \frac{\beta + P_{ch} - P_0}{\beta + P_{ca} - P_0} \end{aligned} \quad (3.108)$$

Substitute Equation (3.106) and (3.107) into Equation (3.108) to yield

$$\frac{\dot{x} - \frac{\dot{P}_{ch}}{\beta} (L_0 - x)}{\dot{x}_L + \frac{\dot{P}_{ca}}{\beta} x_L} = \frac{\beta + P_{ch} - P_0}{\beta + P_{ca} - P_0} \quad (3.109)$$

Substituting Equation (3.95), (3.96), (3.104) and (3.107) into Equation (3.97) yields

$$\begin{aligned}
\left(\dot{x} - \frac{\dot{P}_{ch}}{\beta}(L_0 - x)\right)\epsilon^2 & - \left((x_L \frac{\dot{P}_{ca}}{\beta} + \dot{x}_L) \frac{\epsilon}{\lambda}\right)^2 \\
& - \frac{K_{L1} \epsilon^2}{8} \left((x_L \frac{\dot{P}_{ca}}{\beta} + \dot{x}_L) \frac{\lambda}{\gamma} + \dot{x} - \frac{\dot{P}_{ch}}{\beta}(L_0 - x)\right)^2 \\
& = \frac{P_{ca}}{\rho_0 \left(1 + \frac{P_{ca} - P_0}{\beta}\right)} - \frac{P_{ch}}{\rho_0 \left(1 + \frac{P_{ch} - P_0}{\beta}\right)}
\end{aligned} \tag{3.110}$$

Substituting Equation (3.100) into Equation (3.99) yields

$$P_{ca} = (P_{acc} + K_{L2} \rho \rho_0 \dot{x}_L^2 \left(\frac{\epsilon \gamma}{\lambda}\right)^2) + \frac{G_L \left(1 + \frac{\dot{x}_L}{g}\right)}{A_{cy}} \gamma \tag{3.111}$$

The Equation (3.109), (3.110), (3.111) and together with the stack motion equation (3.101) are totally four equations and with P_{ca} , P_{ch} , x and x_L four unknown variables. Numerical simulations can be used to achieve solutions.

3.4.2 Equations for The Intake Stage

In the intake stage, the stack contracts while the outlet valve is closed and inlet valve is open. The fluid flows from the accumulator into the chamber. Figure 3.14 shows the diagram of system in the intake stage. If the outlet valve is ideally closed, the pressure in the high and low side of the cylinder maintain a constant. Thus it is reasonable to assume the load will not move in this stage.

In the same approach as in the exhaustion stage, we treat the flow from the accumulator to the chamber as two major parts: the piping and fittings, the pumping chamber. In the same manner, we consider all the energy losses exists in the piping and fittings and we treat flow in the pipe as a incompressible quasi-static flow. The fluid in the pumping chamber is first discharged to a low pressure then recharged to the accumulator pressure. Applying Equation (3.81) and (3.75) into the volume of fluid in pumping chamber respectively yields

$$\rho_{ch} = \rho_0 \left(1 + \frac{P_{ch} - P_0}{\beta}\right) \tag{3.112}$$

$$\dot{\rho}_{ch} = \frac{\rho_{ch} V_1 A_p + \rho_{ch} \dot{x} A_{ch}}{(L_0 - x) A_{ch}} \tag{3.113}$$

Applying flow equations and reserve of mass law to the flow in the piping yields

$$V_2^2 + \frac{P_0}{\rho_0} + K_{L3} \frac{\left(\frac{V_1 + V_2}{2}\right)^2}{2} = V_1^2 + \frac{P_{ch}}{\rho_{ch}} \tag{3.114}$$

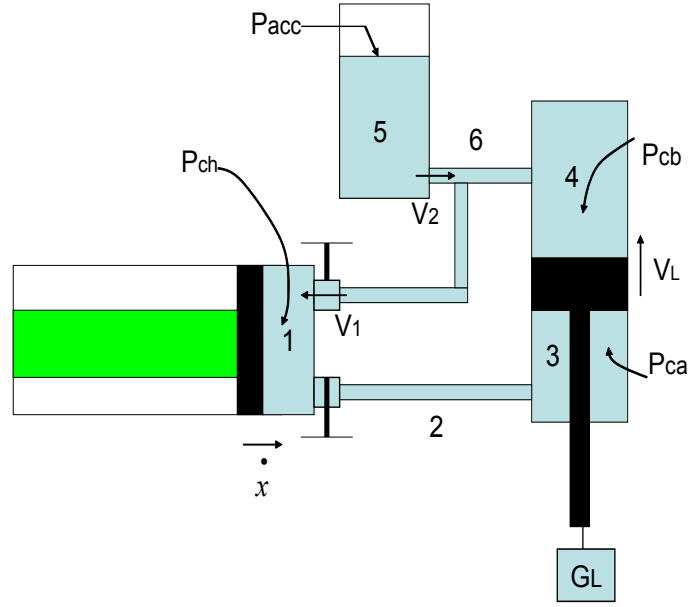


Figure 3.14: Diagram of intake stage for CVF model.

$$\rho_{ch} V_1 = \rho_0 V_2 \quad (3.115)$$

The equation of stack motion is the same as in the exhaustion stage

$$\dot{x} = \frac{x_0 i}{C} - \frac{A_c h}{k_a} P_{ch} \quad (3.116)$$

Equations (3.112), (3.113), (3.114), (3.115), (3.116) are five coupled equations, where five unknown variables, V_1 , V_2 , x , P_{ch} and ρ_{ch} exist. The number of equations is equal to the number of unknown variables, thus the system is solvable given the initial conditions. Numerical analysis can be used to simulate the solutions.

For closed volume operations, such as the compression stage and expansion stage, the equations of motion is the same as in the IVF model (Equation (3.41) and (3.63)). Thus we derived equations in each of the four stages. Given the initial operation conditions, the simulations can iterate on in each stage by using the ending value of states of the previous stage as the initial value of the states in the coming stage. By this way, simulations can be iterated on until it reaches steady states. Based on the simulations, the output power, input power and power efficiency defined in the previous chapter can be computed and analyzed, which will be going into the next chapter. Figure 3.15 shows the one cycle of the simulation results of CVF model at 100 Hz operation frequency under 6.84 Kg load.

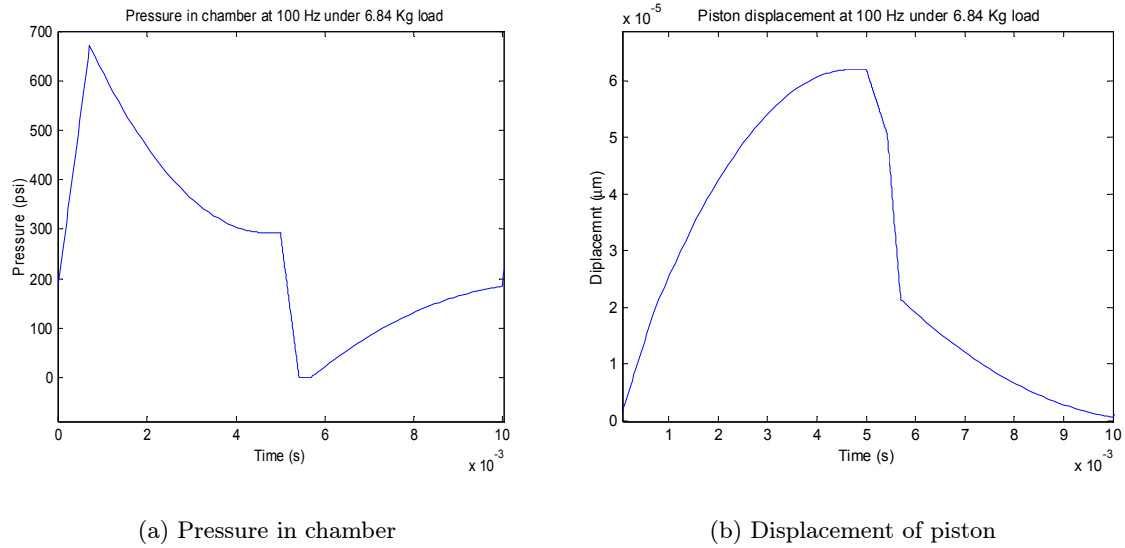


Figure 3.15: CVF Simulation at 100 Hz under 6.84 Kg load

3.5 Summary

In this chapter, three models are presented to analyze the system. Although the IIF model does not take into account the energy losses and compressibility in fluid flow, it shows some basic features of the piezohydraulic system, which could be guidelines for further studies. The inviscid flow model shows the double-ended cylinder is superior to single-ended ones in terms of both power and efficiency issues. For a single-ended cylinder, the efficiency will increase as the load increases. For any cylinder, an optimal load that maximizes the output power exists under a given pre-pressure.

The quasi-steady IVF flow model takes account in the energy losses due to viscosity and thus can more accurately predict the behavior of the system. The states of the viscous flow model are a function of time, which indicates it could provide dynamic characteristics of the system that is not available from the inviscid model. The model is comprised of a first order ODE in each stage, which makes it a compact model with small computation effort. However by neglecting compressibility of the fluid, performance may be overestimated. Based on this observation, a CVF model which takes account in both viscosity and compressibility is presented. In order to avoid complex dynamic model, approximations were made. It involves four or five first order non-linear ODEs, which we expect to give more accurate predictions than the IVF model.

Chapter 4

Experimental Results And Simulations

4.1 Introduction

The test setup is presented in this chapter. The bulk modulus of the fluid is characterized and the characteristics of power supply are determined experimentally. These parameters are then combined with the theoretical models for system simulations. The single-ended cylinder and double-ended cylinder are tested and simulation results of both IVG and CVG models are compared. Power and efficiency are calculated and analyzed.

4.2 Experimental Setup

The figure below is the diagram of the experimental setup of the system. A dSpace control unit implementing SIMULINK model with 8 input and 8 output channels is used to manage and instrument the experiment. The SIMULINK model is built and the object module is then downloaded into dSpace unit which provides a user-friendly interface for real-time signal acquisition and control.

There are three output signals from dSpace unit in this system setup. One controls the piezoelectric stack actuator and the other two control the inlet and outlet valve respectively. Because the maximum voltage of the output signal is 10 V and the operating voltage of stack actuator and valves are in the order of hundreds of volts, power amplifiers are used to provide enough power and appropriate voltages. In order to measure the performance of

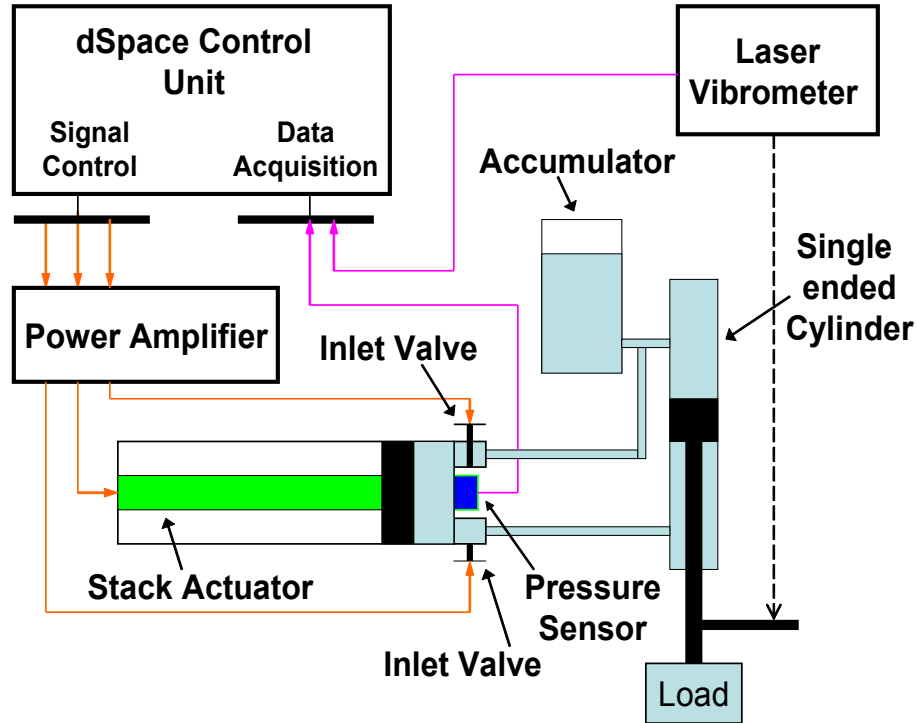


Figure 4.1: Experimental setup diagram for velocity measurement

the system, the velocity of the load can be calculated by the displacement of the load and then the power can be computed give a known load. The pressure in the pumping chamber and displacement of piston are also measured. The force acting on the stack is computed by the pressure times the area of pumping chamber and the force-displacement relationship of the piston can be used to compute the work done on each cycle. The power of the output of piezoelectric stack can be computed by averaging the work and dividing by time of the cycle. The input current and voltage to the stack actuator is measured and the electrical power can be computed. Thus with the experiment setup, we can compute the input power and output power the piezoelectric actuator and the power transferred to the load, which will enable us to analysis the electromechanical efficiency η_e and mechanical efficiency η_m defined in *Chapter 2*.

Figure 4.2 shows the experimental setup. In this configuration a double-ended hydraulic cylinder is used. A piezohydraulic actuation unit consisting of a housing, pumping chamber and piston was fabricated as shown in Figure 4.3. The components were designed in house, whereas the piezoceramic stack actuator and corresponding flexure were purchased

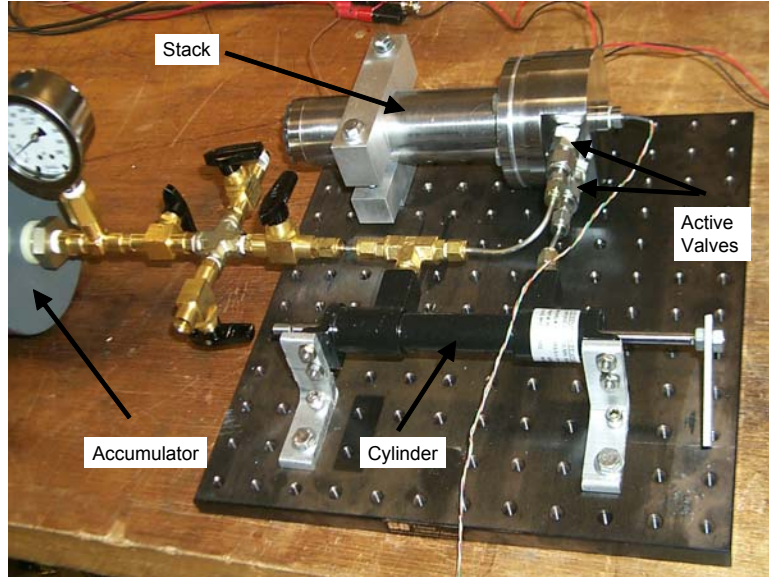


Figure 4.2: Experiment setup

from Physik Instrumente (P-844.60 and P-176.60). These components were assembled together with aluminum plates separating the housing and pumping chamber, which allowed us to vary the volume of fluid inside the pumping chamber. Active valves are then integrated with the unit into one component. The actuation system measured approximately 32 cm in length with an OD of almost 8 cm around the pumping chamber. The pumping chamber measured 2.5 cm in diameter with a 2 mm length.

4.3 Bulk Modulus Measurement

Air dissolved in the hydraulic fluid can result in a bulk modulus that is much lower than that of pure hydraulic fluid. It is noted when deriving the flow equations in Chapter 3 a known bulk modulus is assumed. However, because the amount of air dissolved is difficult to know, the bulk modulus is hard to determine. Manring (Manring, 1997) found bulk modulus is a function of pressure. He experimentally showed that the bulk modulus of hydraulic fluid β can be model as a linear function of pressure P ,

$$\beta = \gamma P + \beta_0 \quad (4.1)$$

where γ and β_0 are constant.

Closed chamber tests are conducted in order to determine the equivalent bulk modulus of the mixed working fluid. The idea of closed chamber tests is to compute the equivalent

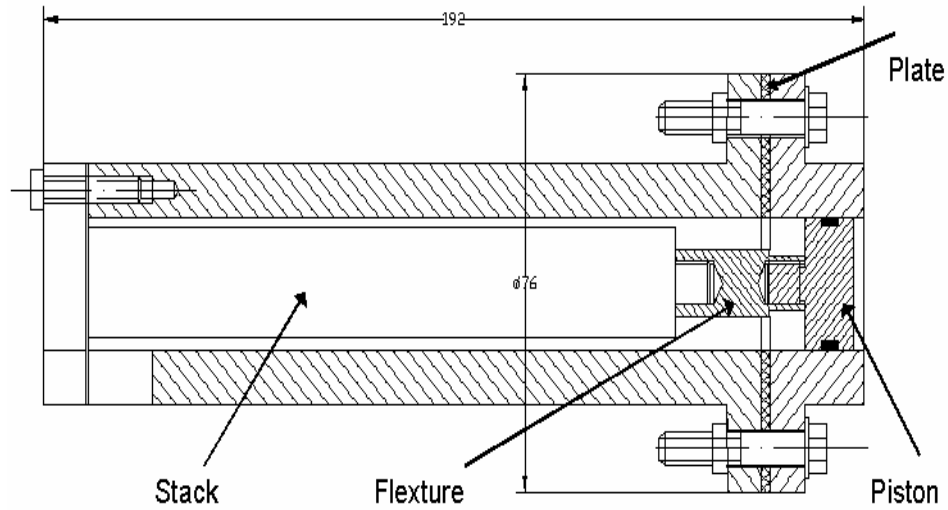


Figure 4.3: Components of stack unit

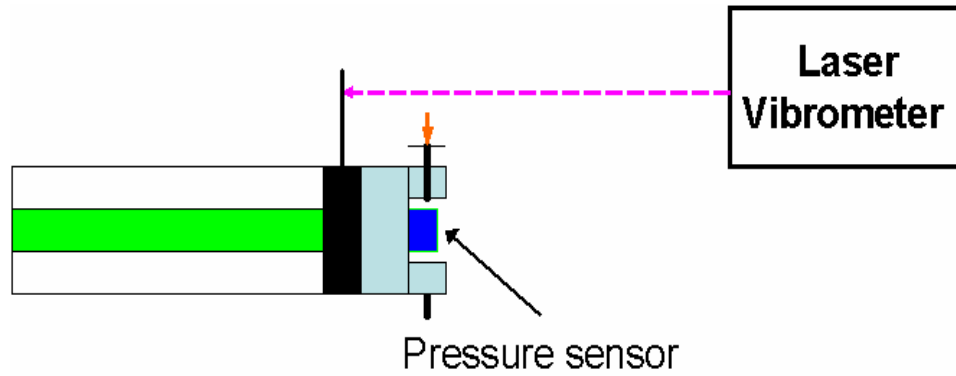


Figure 4.4: Closed chamber test setup

stiffness of the fluid by measuring the pressure and volume change of a closed volume of fluid. According to Doebelin (1972), the equivalent stiffness of a volume of fluid can be calculated by

$$K = \frac{\beta A}{l}, \quad (4.2)$$

where A is the cross section area of the fluid volume and l is the length of the fluid volume. By measuring the stiffness of the fluid, we can compute the bulk modulus by Equation (4.2).

The closed volume test setup is shown in Figure 4.4. We maintain the inlet valve and outlet valve closed all the time. By applying electrical excitation to the stack actuator, we measure the pressure in the chamber and the displacement of the piston.

The force acting on the piston was calculated by multiplying the fluid pressure with

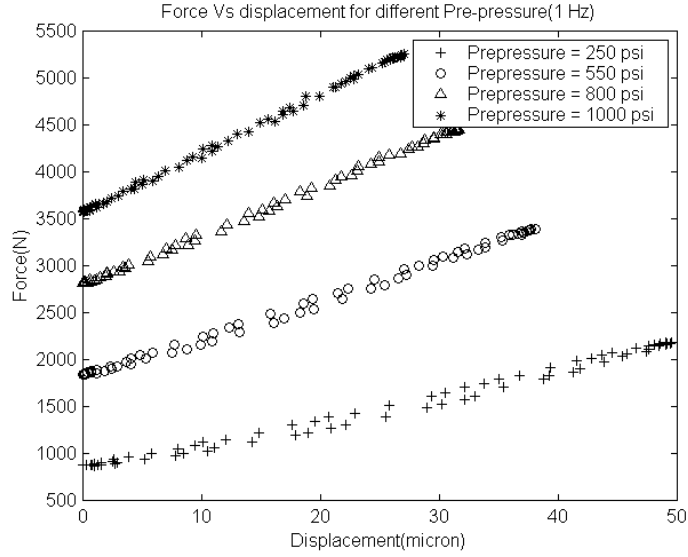


Figure 4.5: Force vs displacement

the cross section area of the pumping chamber. Tests were run at different pressures in order to characterize the hydraulic fluid by determine the constants γ and β_0 in Equation (4.1). Different pre-pressures were applied to the hydraulic fluid in the closed chamber. Figure 4.5 shows the force-displacement relationship for tests run at 1 Hz. Four different pre-pressures were applied before the stack began to push against the fluid. It is noted that for each pressure, the force-displacement is similar to a straight line, which means for a specific pre-pressure, the stiffness and the bulk modulus of the fluid can be assumed to be constant. Figure 4.6 shows the equivalent stiffness of the fluid for different pre-pressures by computing the slope of the force-displacement in Figure 4.5. The equivalent stiffness of the fluid was obtained by calculating the slopes of these lines shown in Figure 4.5. The equivalent stiffnesses of the hydraulic fluid at different pre-pressures are shown in Figure 4.6. The stiffness changed substantially as a function of pre-pressure, from 27.0 N/ μm at 250 psi pre-pressure to 62.9 N/ μm at 1000 psi pre-pressure. Figure 4.6 also shows that the peak-to-peak displacement of piston decreases linearly as the pre-pressure increases. It is noted the stiffness increases as pre-pressure increases while the peak-to-peak displacement of the stack decreases. Higher stiffness will allow more power to be transferred to the load while smaller stroke will definitely deteriorate the performance of the actuation system. This is a compromise situation.

The measured equivalent stiffness of fluid is dependent on pre-pressure, which indi-

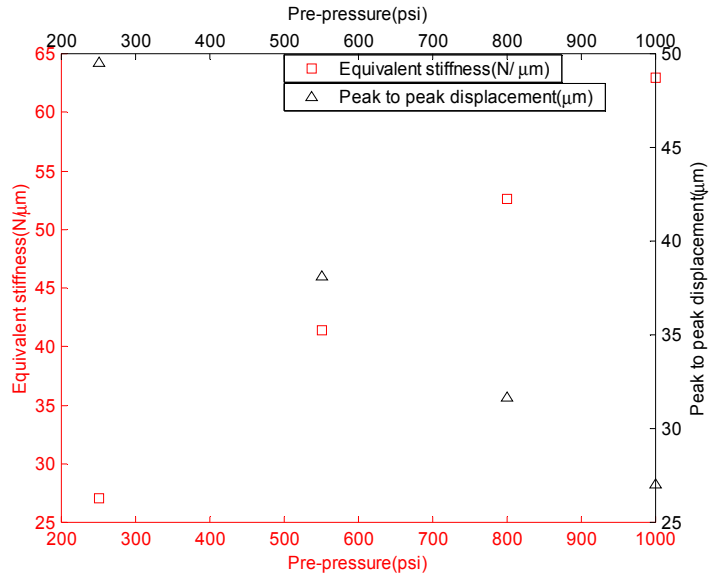


Figure 4.6: Peak pressure

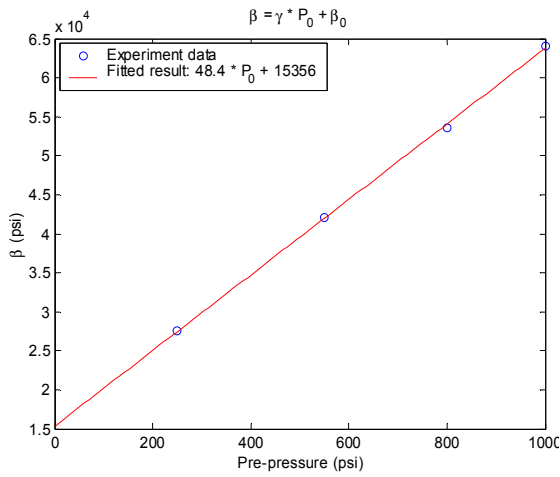


Figure 4.7: Linearly fitted bulk modulus with pressure

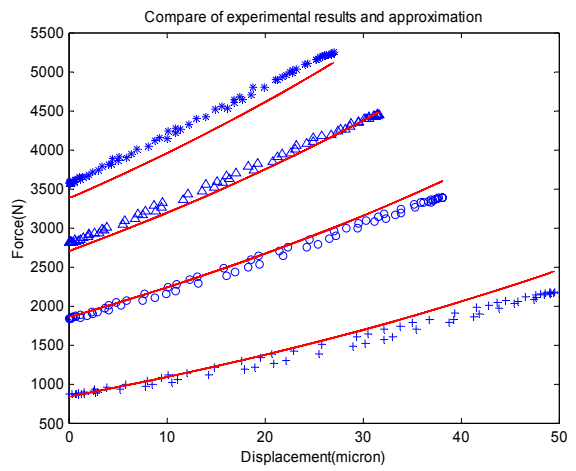


Figure 4.8: Experimental and approximated force-displacement

icates that the bulk modulus of working fluid is dependent on pre-pressure as well. The bulk modulus β was calculated by

$$\beta = \frac{KL}{A} \quad (4.3)$$

where K is the equivalent stiffness, L is the length of the fluid element and A is the cross section area of the fluid element. Figure 4.7 shows the calculated bulk modulus and a linear approximation of it based on equation(4.1). The constant γ is obtained by calculated the slope of the linear approximation of bulk modulus as a function of pressure and β_0 is obtained by calculated the intersection of the line approximation with the y-axis, physically the bulk modulus at zero pressure. The linear bulk modulus model (units in psi) is as following

$$\beta = 48.8P + 15356, \quad \beta_0 = 15356, \quad \gamma = 48.8 \quad (4.4)$$

To check the validity of the linear model, the force as a function of displacement was calculated based on the model and compared to the experimental data. The bulk modulus of fluid is defined as,

$$\beta = -\frac{dP}{dV/V} \quad (4.5)$$

where P is fluid pressure and V is the volume of fluid element. With equation 4.1 and 4.5, we obtained the force F as a function of displacement x as

$$F = [(P_0 + \frac{\beta_0}{\gamma}) \exp(\frac{\gamma x}{L}) - \frac{\beta_0}{\gamma}]A \quad (4.6)$$

where P_0 is pre-pressure of fluid.

Figure 4.8 shows both the force-displacement relationship from equation 4.6 and the experimentally measured data under different pre-pressures. It is noticed that for the case of 250 psi low pre-pressure, there are relatively big discrepancies between the model and experimental data when the displacement is at the end of stroke. While for the other three cases whose pre-pressures are 500 psi, 800 psi and 1000 psi, the maximum relative error between the linear model and experiment results is less than 8%. It indicates the linear bulk modulus to pressure model has better approximation for higher fluid pressure.

In this section, a linear bulk modulus to pressure model was presented and verified by experimental results. This model will then be used to determine the bulk modulus of the fluid in theoretical simulations.

4.4 Simulation Parameters

The model of IVF and CVF presented in Chapter 3 will be used to predict the performance and efficiency calculations. In the simulations performed in this paper the following parameters will be used:

- The modulus of the fluid will be modeled as Equation 4.4.
- The density of fluid is assumed to be $\rho = 900(kg/m^3)$, which is a typical density for mineral oil. The viscosity $\nu = 3 \times 10^{-5}(m/s^2)$ as calculated in Equation (3.35).
- The dynamics of the power supply to the stack actuator is different for different amplifier. For a specific amplifier, the peak voltage and peak current is constant, which will be determined by experimental measurements.
- The area ratio of section of rod and section of hydraulic cylinder is set to be 1/4 for both single-ended and double-ended cylinders, which means the diameter of the rod is one half of the diameter of the cylinders. For single-ended cylinders the load is assumed to be attached to the side of the cylinder where the area is smaller than the other side.

4.5 Single-ended Cylinder

The single-ended cylinder test bench is built and tested first. A DSM 2 Level PZT drive whose maximum operation frequency is 100 Hz is used to power the piezoelectric stack. A two channel Trek amplifier of model 70/750 is used to power the two active valves. The system is sealed in a closed volume and then a vacuum pump is used to such the air inside the system in order to increase the effective bulk modulus of the fluid. Then the valve connected to the accumulator is opened and the whole system is filled with pre-pressurized fluid. At this point, all the preparation work is done and the system is ready for testing.

4.5.1 Characteristics of Power Amplifier

The DSM 2 drive in test always generate a square wave signal with a maximum peak current at a fixed peak voltage. Figure 4.9 shows voltage output of amplifier under different load respectively at 100 Hz operation frequency. The figures show the peak voltage is fairly constant under different load for the same frequency. It is noted that the voltage signals are in general periodic but the amplitude and shape are not same in each period due to noise or unknown dynamics. Figure 4.10 shows current output of amplifier under different

load respectively at 100 Hz operation frequency. It is noted it has a peak current of 4.2 Amps. In order to study the frequency response of the power amplifier, the current signals and voltage signals are averaged into one period to cancel the noise. The peak voltage and peak current of the averaged signal at different frequencies are shown in Figure 4.11 and Figure 4.12.

From the averaged voltage signal and current signal shown in Figure 4.11 and Figure 4.12, we notice the amplitude of the voltage signal and current signal decreases as frequency increases. For frequency less than 70 Hz, the change is relatively small, but above 70 Hz this tendency becomes more obvious. The reason is that operating at higher frequency requires higher power and the amplifier has to reduce the peak voltage and current for higher frequency.

Because the output voltage and current values are the characteristics of the power supply which is not accounted into our model, this peak voltage and peak current will be set in the model when simulating the performance under a specific frequency. To simplify the output signal of the power supply, we approximate the current signal to be a ideal square wave with an amplitude determined by Figure 4.12. We can assume the input impedance is an ideal capacitor, then we have

$$V = \frac{\int i dt}{C} \quad (4.7)$$

Thus the voltage can be computed if the current i is known. Figure 4.13 shows the simplified current and voltage signal in one operation period. This input signal model will be used when simulating the performance of the system.

4.5.2 Performance Measurements and Simulation

The fluid was pre-pressured at 230 Psi for the first set of tests. Because the maximum operation frequency of the DSM 2 amplifier is 100 Hz, the system was tested at frequencies from 20 Hz up to 100 Hz. Through these tests, a timing scheme of 50% stack duty cycle and 40% valve duty cycle with 5% outlet valve offset and 55% inlet valve offset is adopted. The pressure in the pumping chamber, the displacement of load and displacement of the piston are measured.

A typical time responses of the system are show in Figure 4.14. The pressure shown in the first part of figure has different peaks and dips in different cycle and so does the

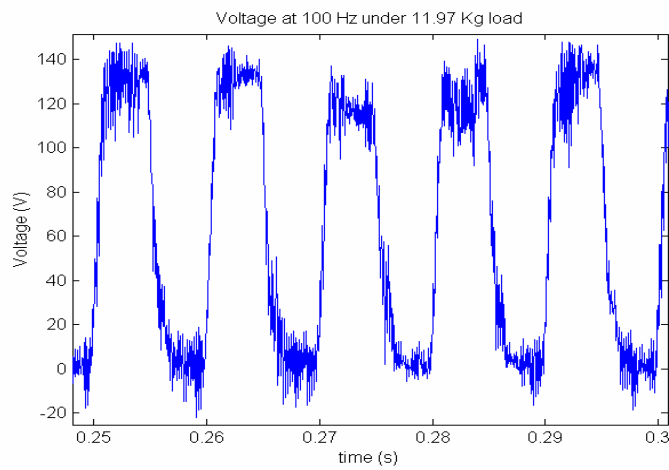
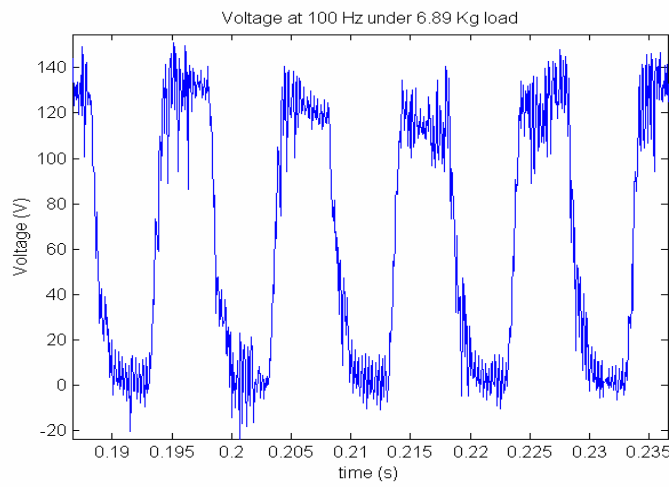
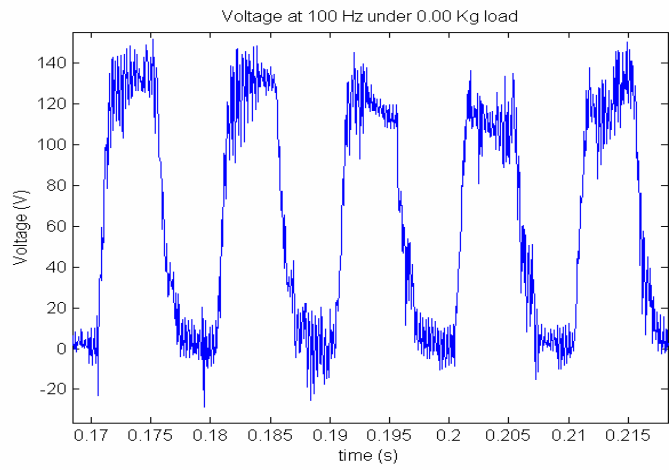


Figure 4.9: Voltage at 100 Hz frequency under different loads

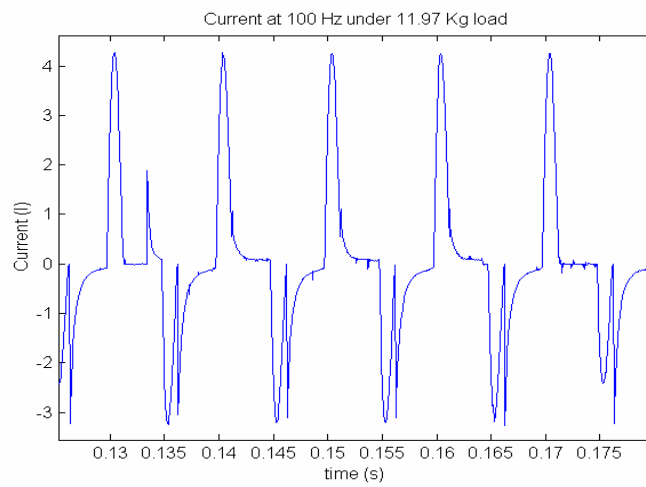
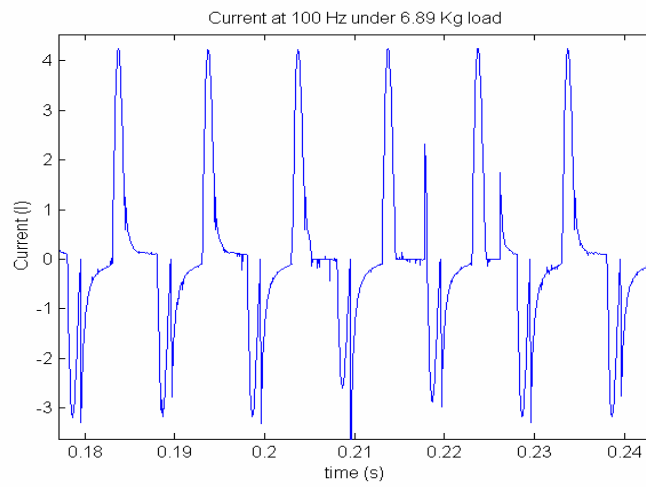
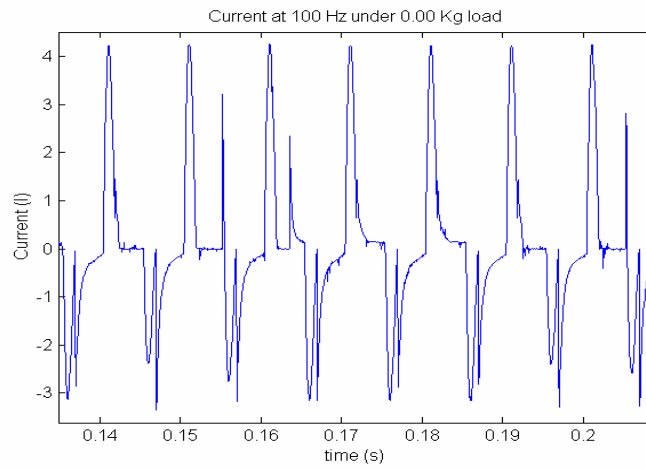


Figure 4.10: Current at 100 Hz frequency under different loads

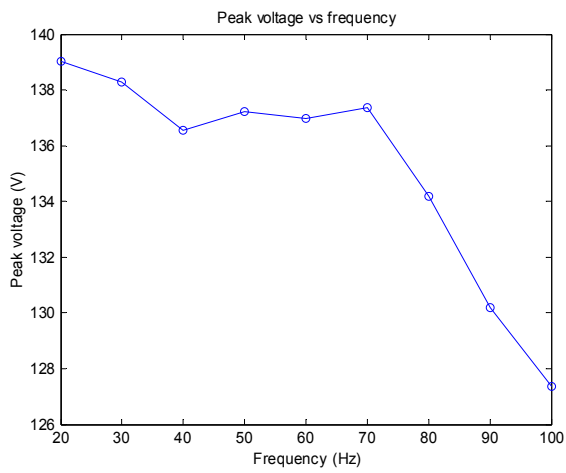


Figure 4.11: Peak voltage for different frequency

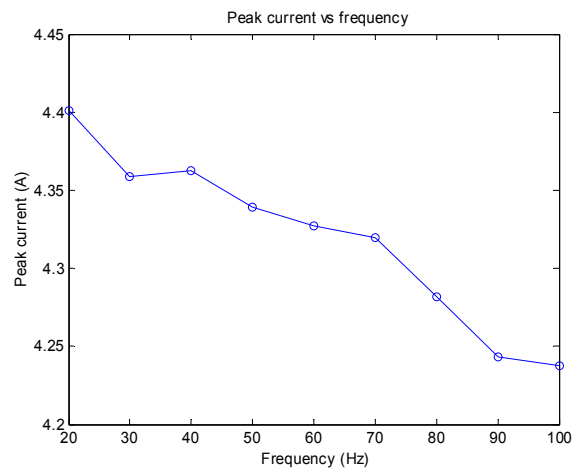


Figure 4.12: Peak current for different frequency

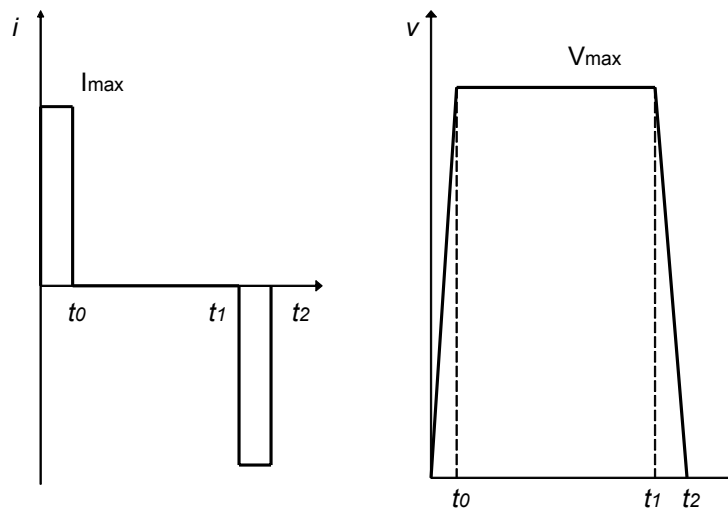


Figure 4.13: Current and voltage model of input of stack

displacement of piston shown in the second part. The third part of the figure is the displacement of load plot. The velocity of the load is calculated by computing every slope of the load displacement plot. It is noted that the pressure signals and displacement signals becomes irregular due to noise problem. The same average technique as dealing with the current and voltage signal in the previous section is used to processing the measurement signals in order to get rid of the noise. Figure 4.15 shows the average pressure and piston displacement in one cycle. It is noted that both signals are much smoother after averaging which means the noises are effectively canceled.

Figure 4.16 shows a typical valve timing. For this timing, duty cycle of the stack is 50% and duty cycles of both valves are 40%. The outlet valve opens at 5% and closes at 45% offset the stack timing. The inlet valve opens at 55% and closes at 95% offset the stack timing. This timing was chosen in order to achieve optimum performance. Figure 4.17 shows the pressure of the pumping chamber in the four stages of one cycle. It is noticed when the stack retracts the pressure in the chamber goes even a little below zero. Because we set the zero to be atmosphere pressure, a negative pressure means pressure below the atmosphere pressure.

The simulation begins with the initial states, where the total system is subjected to a uniform pre-pressure and the displacements and velocities of the fluid is assumed to be zero. Then the simulation program runs into a cyclic fashion where the final states of the previous cycle are set to be the initial states of the following cycle. This iterative approach only ends when the states of the system converges. In the program, we assume the system to be converged when the difference of the pressure in the pumping chamber between two consecutive cycles are less than 1%. Figure 4.18 and 4.19 show the simulation results of CVF model at 100V peak voltage excitation for 100 Hz and 200 Hz respectively. It is noted that it takes more cycles for 200 Hz to converge than the 100 Hz one. We notice that in the intake stage due to the fluid can not flow back into the chamber enough, the operation at 200 Hz has a lower final intake pressure than the other one, which results in the less stiff fluid and thus lower dynamic pressure. Simulations results show that the maximum stroke of piston for 200 Hz is around 55 μm while for the 100 Hz the maximum stroke is 49 μm . And the peak pressure at 200 Hz is 480 psi while for the 100 Hz it is 520 psi. The stroke increase for 200 Hz does not increase the displacement of the load. On the contrary, the lower stiffness of the fluid need to be compressed more to achieve the pressure to drive the

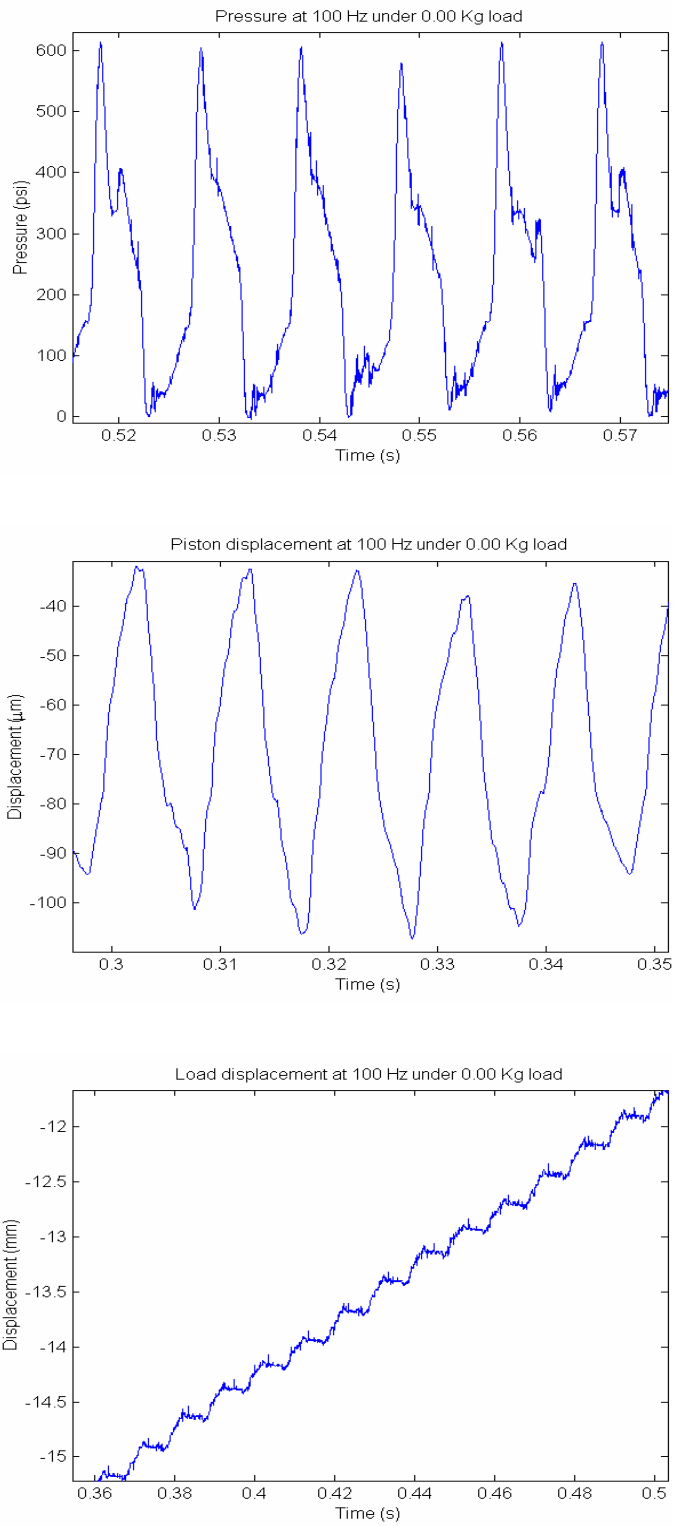


Figure 4.14: Performance measurements at 100 Hz under 0Kg load

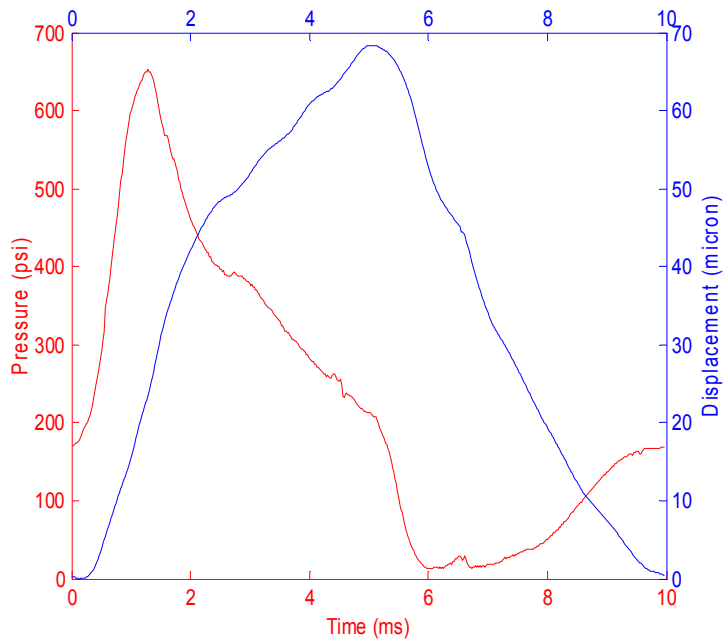


Figure 4.15: Average measurements at 100 Hz under 0Kg load

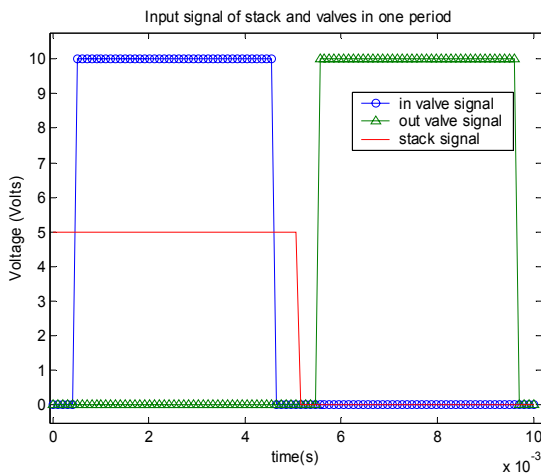


Figure 4.16: Four stage timing at 100 Hz

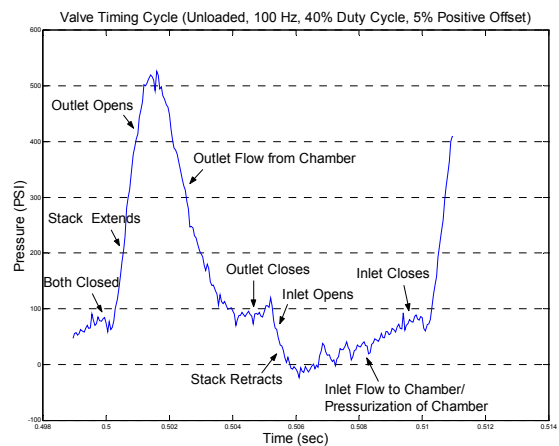


Figure 4.17: Pressure in chamber in four stages at 100 Hz

load, which reduce the performance of the system.

Figure 4.20, 4.21 and 4.22 show the simulation results and experimental measurement of chamber pressure and piston displacement at 50 Hz operating frequency under different loads. For all the three loads, the simulation results match with experimental very well. The peak pressure is almost the same and the back pressure at the mid point of the cycle also match very well. It is noted that the pressure decay from the peak for the CVF models are slower than the ICF models under every load. We believe it can be contributed to the compressibility of fluid. For the CVF model, the volume of fluid increases as it flows from high pressure chamber to low pressure cylinder and thus take more time to flow out the chamber than the IVF model predicts. The CVF models match the experimental results better than the IVF models

Figure 4.23, 4.24 and 4.25 show the simulation results and experimental measurement of chamber pressure and piston displacement at 100 Hz operating frequency under different loads. It is noted that at 100 Hz, neither IVF model nor the CVF model matches with the experimental data as well as for 50 Hz operation frequency. This may result from the operation frequency limit of the 100 Hz of the power supply. At 100 Hz, the voltage and current signal might be more distorted rather than the ideal square wave which is assumed by the model.

The velocity of load can be calculated by multiplying the displacement of load in one cycle by the operation frequency. The calculated velocity is the average velocity rather than an instantaneous velocity. The power output of the system can be computed by multiplying velocity by the weight of load. Thus the power calculated is also an average power.

The simulation of velocity and power of CVF and IVF models are compared with experimental data in Figures 4.26 to Figure 4.31. The CVF model is much more close to experimental data than IVF model in terms of both velocity and power. For loads up to 15 Kg, the simulation results of CVF model consist with the experimental data pretty well. It is noted the simulation velocity of both model are very like a straight line. But the slope of the CVF model is steeper than the slope of IVF. Accordingly, the difference of the two models becomes more obvious when the load is larger than 7 Kg. The reason can be explained by the compressibility of the fluid. When a larger load is attached to the cylinder, the back pressure is increased, which reduce the stroke of the piezoelectric actuator. Thus the displacement of the load also decreases accordingly. Furthermore, due

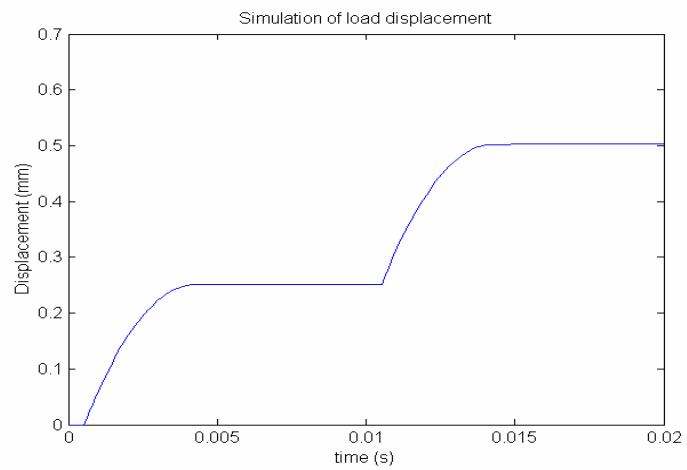
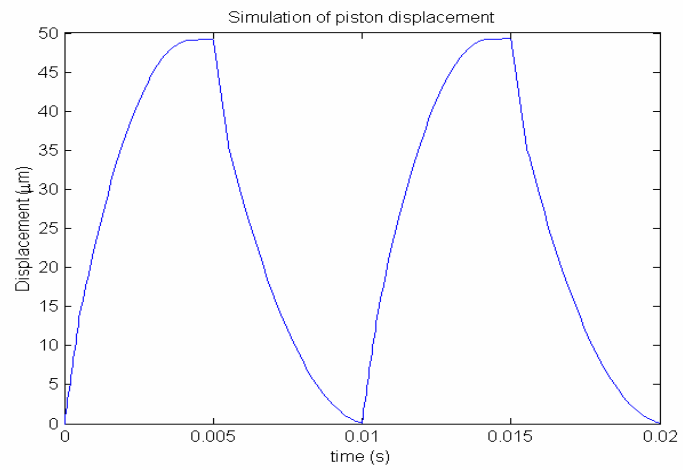
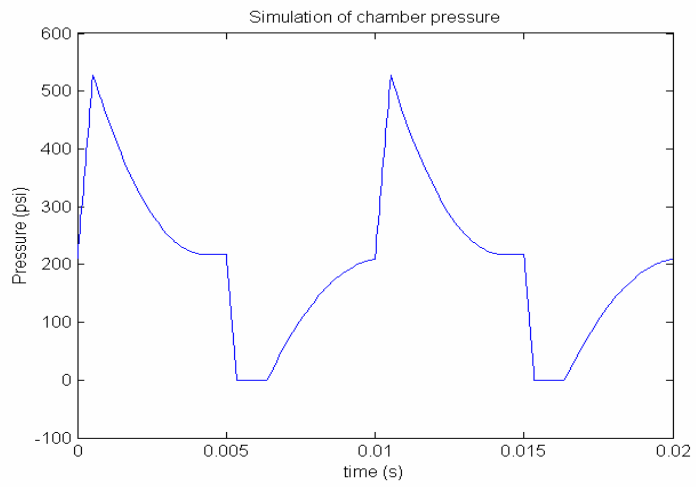


Figure 4.18: Simulation results at 100 Hz under 0 Kg load

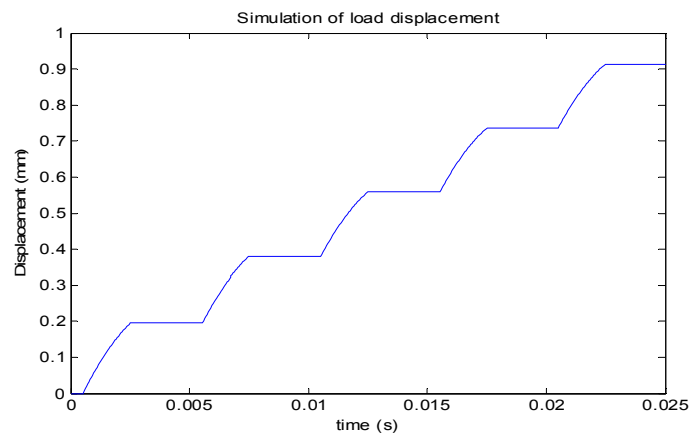
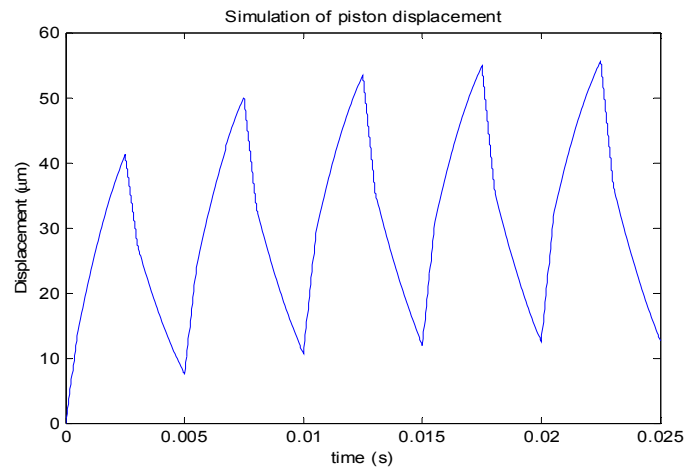
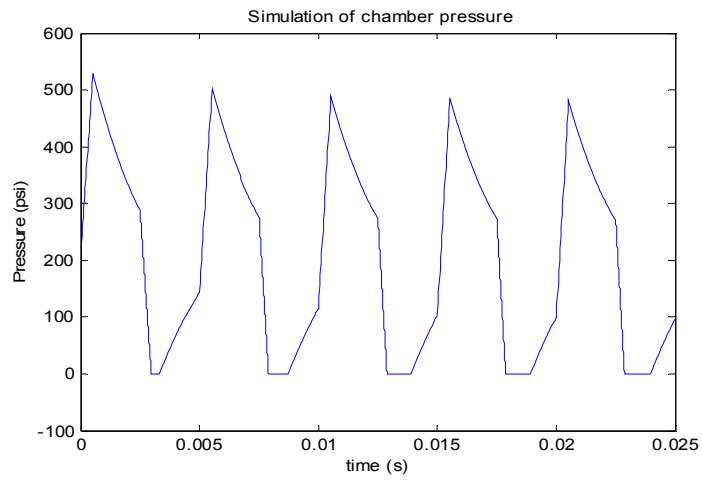
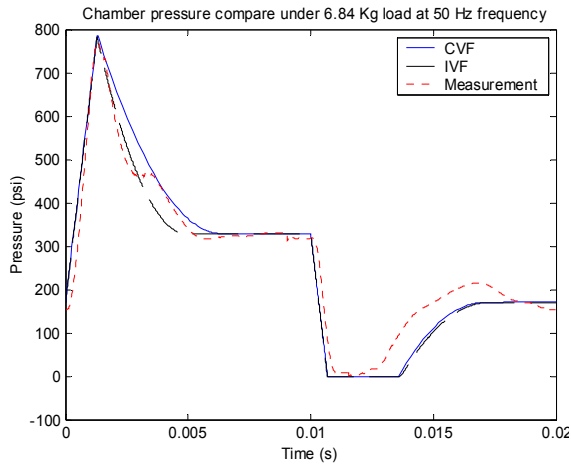
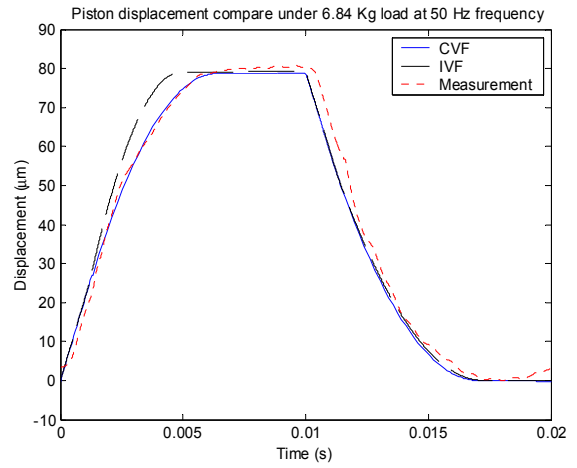


Figure 4.19: Simulation results at 200 Hz under 0 Kg load

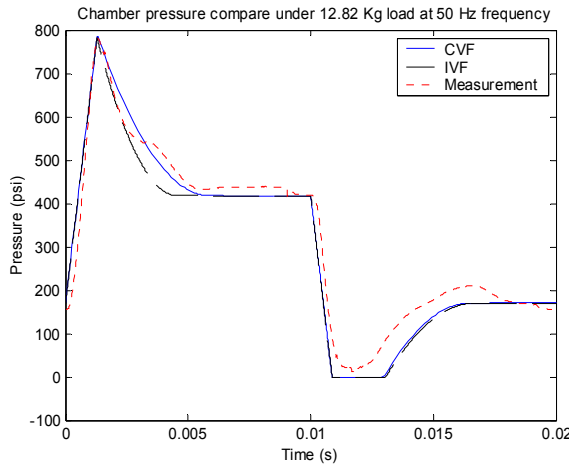


(a) Pressure

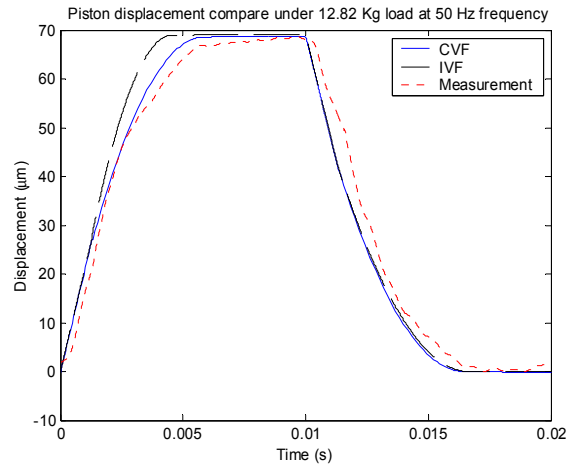


(b) Piston displacement

Figure 4.20: Measurements compare of the single-ended cylinder at 50 Hz under 6.84 Kg load

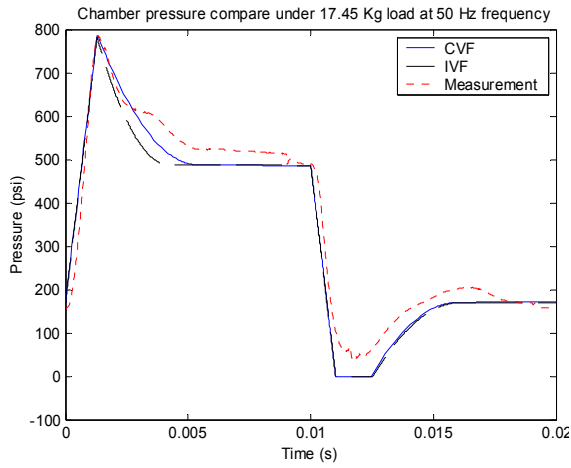


(a) Pressure

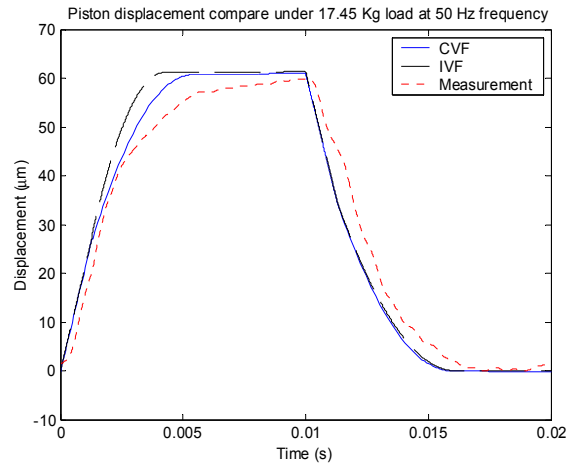


(b) Piston displacement

Figure 4.21: Measurements compare of the single-ended cylinder at 50 Hz under 12.82 Kg load

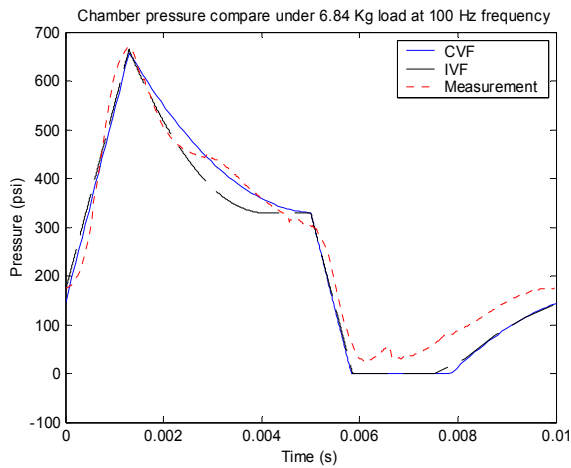


(a) Pressure

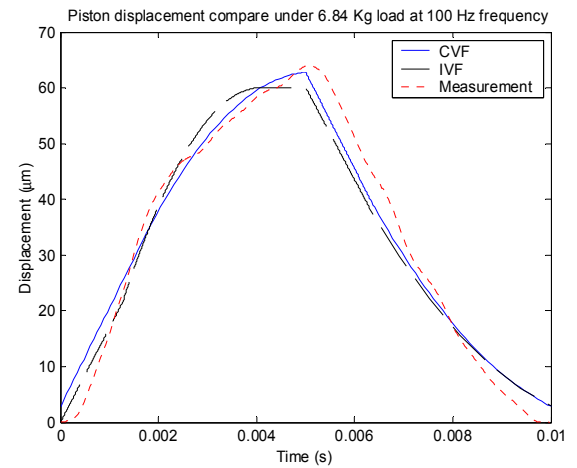


(b) Piston displacement

Figure 4.22: Measurements compare of the single-ended cylinder at 50 Hz under 17.45 Kg load

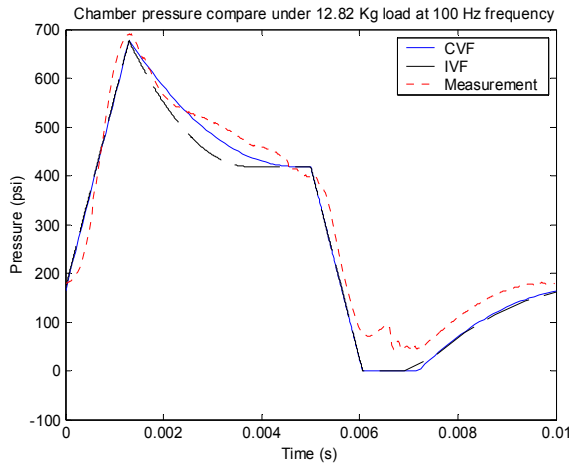


(a) Pressure

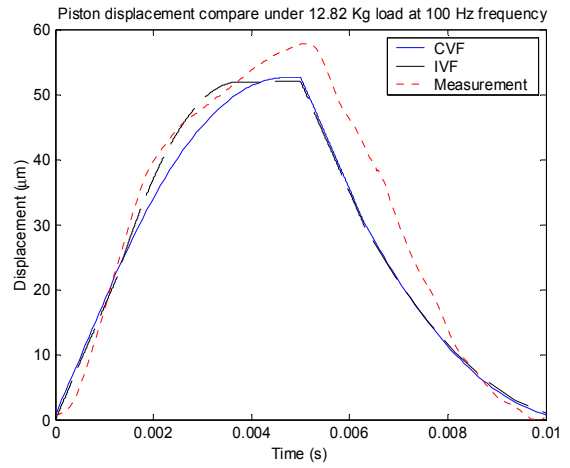


(b) Piston displacement

Figure 4.23: Measurements compare of the single-ended cylinder at 100 Hz under 6.84 Kg load

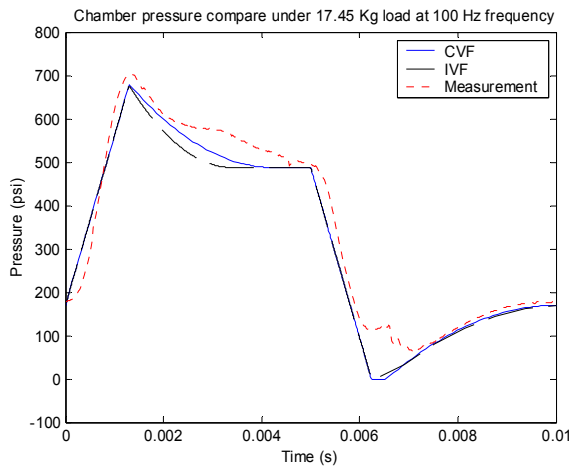


(a) Pressure

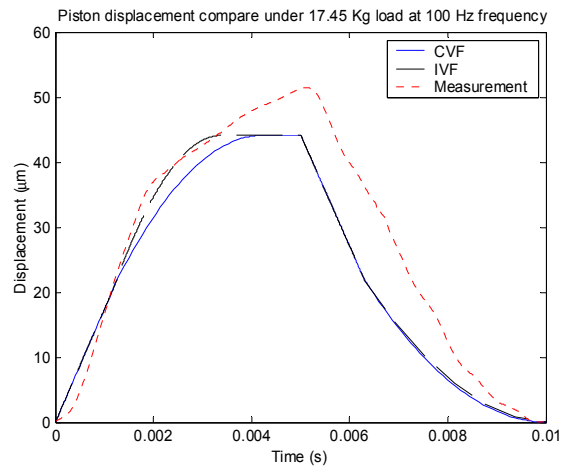


(b) Piston displacement

Figure 4.24: Measurements compare of the single-ended cylinder at 100 Hz under 12.82 Kg load



(a) Pressure



(b) Piston displacement

Figure 4.25: Measurements compare of the single-ended cylinder at 100 Hz under 17.45 Kg load

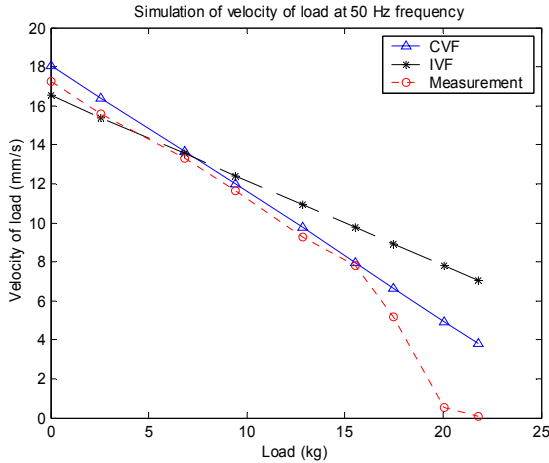


Figure 4.26: Velocity comparison at 50 Hz

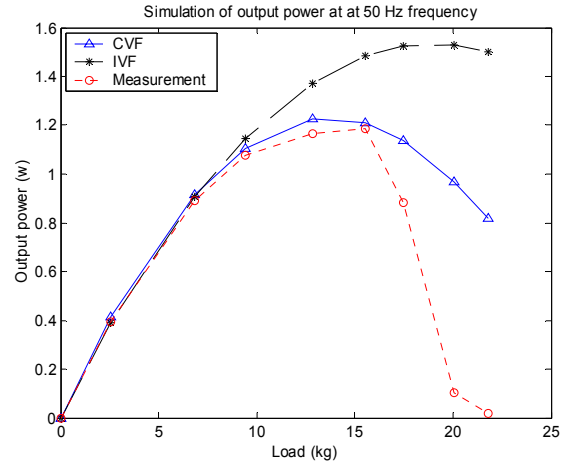


Figure 4.27: Power comparison at 50 Hz

to the compressibility of the load, additional decrease of load displacement is inevitable. When the high pressure fluid in the chamber flows into the low pressure cylinder, the volume will increase due to pressure drop. A heavy load results in higher pressure in the cylinder and thus lower pressure drop, the effect of the volume increase by the pressure drop is reduced. This additional decrease of load displacement is not taken into account for the IVF models because they assume an incompressible fluid. Hence, the simulation results of IVF model overestimates system performance under large loads.

It is also noted that for load heavier than 15Kg, the difference between the CVF model and experimental data increases. As the load increases over 15Kg, the measured velocity decreases very fast for each of the three frequencies. We believe this fast drop for heavy load is because the leakage problem of the valves, which we observed pressure drop in the pumping chamber with both valves closed. Figure 4.32 and 4.33 shows the displacement of load when operated under 20 Kg load at 50 Hz and 100 Hz respectively. At 50 Hz, the reverse movement is very obvious and almost cancels the stroke. At 100 Hz, the reverse movement still exists but much smaller. The reason is that at the expansion stage the pressure in the pumping chamber drops to as low as near zero pressure, the pressure drop through the valves make the fluid flow from the cylinder into the chamber reversely. The higher load, the higher pressure drop, which means larger reverse movement. And this stage lasts longer, the reverse movement becomes larger, which justifies the observation that reverse movement at 50 Hz is more obvious than at 100 Hz.

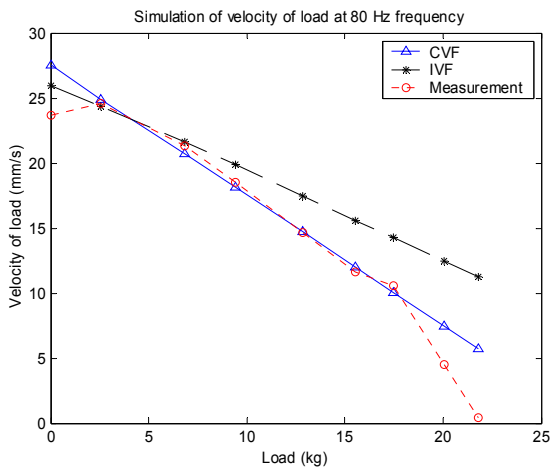


Figure 4.28: Velocity comparison at 80 Hz

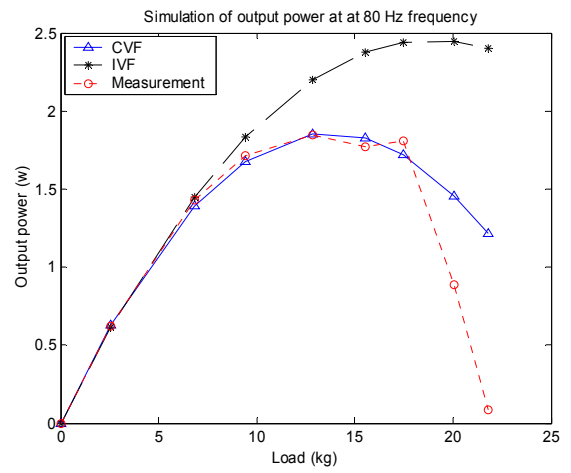


Figure 4.29: Power comparison at 80 Hz

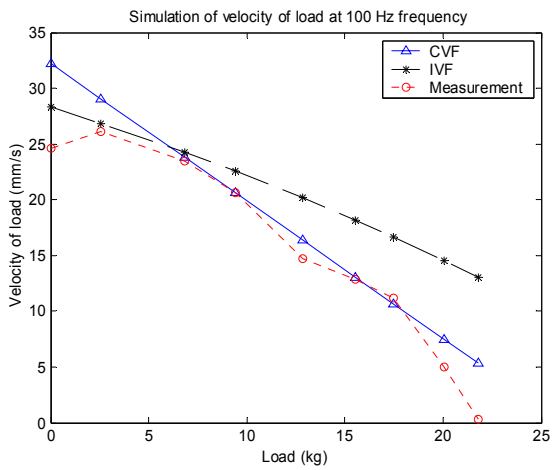


Figure 4.30: Velocity compare at 100 Hz

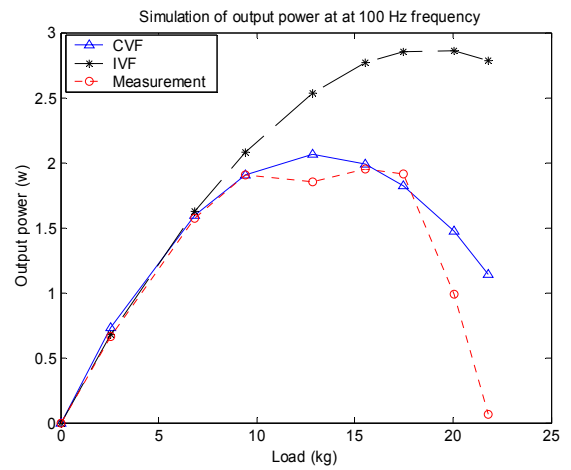


Figure 4.31: Power compare at 100 Hz

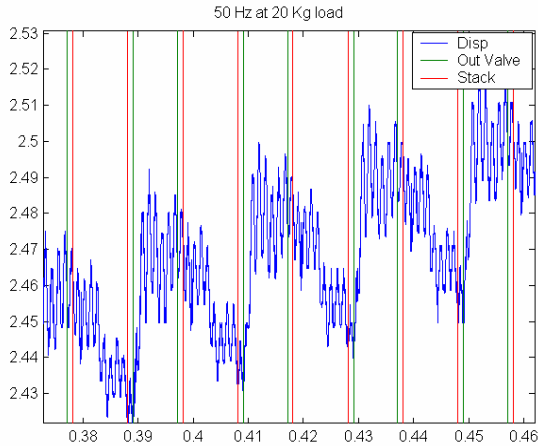


Figure 4.32: Load displacement at 50 Hz

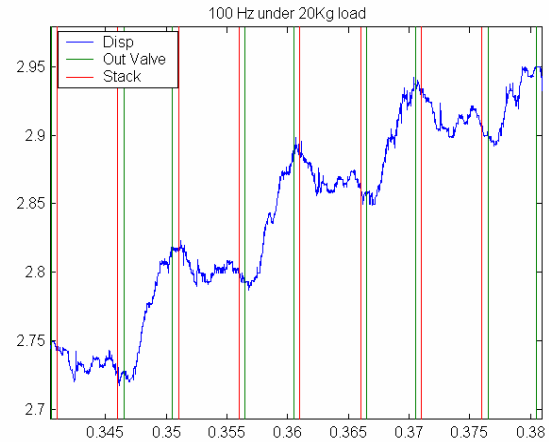


Figure 4.33: Load displacement at 100 Hz

4.6 Double-ended Cylinder

The double-ended cylinder test bench was built in order to achieve better performance and it was tested using a new amplifier that enables operation in the kilo-hertz range. A DSM 3 channel power amplifier with one 150 V low voltage and two 1500 V high voltage is used to power the system.

4.6.1 Characteristics of Power Amplifier

The advantage of the DSM 3 channel power amplifier is it can generate larger peak current which means shorter transient and higher operation frequency. The peak voltage of each channel can be adjusted manually. Figure 4.34 shows current output of amplifier under no load at 200 Hz operation frequency. It is noticed the peak current saturated at about 8.3 Amp.

4.6.2 Performance Measurements and Simulation

The system was tested at two level of excitation voltage of 100 V and 130 V. At each level of voltage, different loads were attached with the output cylinder when operated in a series of frequencies.

Figure 4.35, 4.36, 4.37 and 4.38 respectively shows the measurement of pressure and load displacement at 100 Hz and 200 Hz operation frequency. Comparing with Fig-

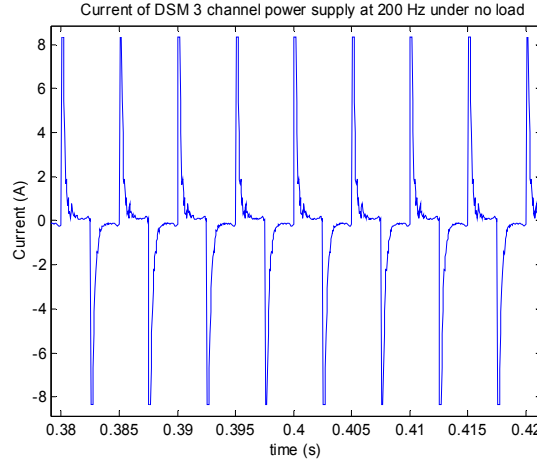
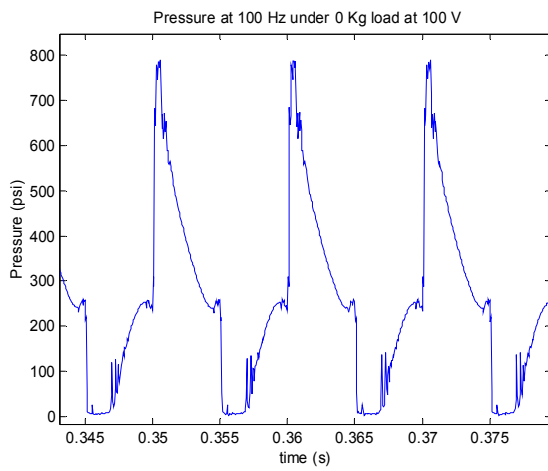


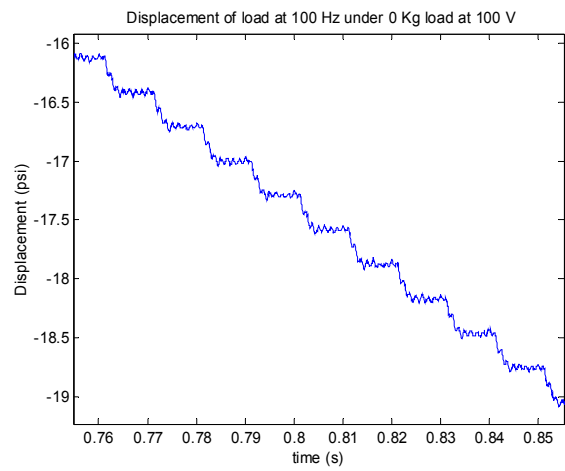
Figure 4.34: Measurements of stack current at 200 Hz under no load

ure 4.35(a) and Figure 4.36(a), we notice that the back pressure which dropped from the peak pressure is higher for heavier load, which is also true for other pairs. In Figure 4.35(a), we notice that the pressure almost drop to the pre-pressure from the peak in the intake stage in each cycle, while in Figure 4.37(a) the final pressure at the end of exhaustion stage is around 400 psi, which is far above the pre-pressure around 200 psi. It indicates the work stored in the stack can not be transferred to the load fast enough such that at the end of exhaustion stages there is still a considerable energy left. It is because of the friction resulted from viscosity of fluid. When operating at higher frequency, this phenomenon becomes more obvious. The displacement of load each cycle in Figure 4.37(b) is also much smaller than in Figure 4.35(b). It clearly demonstrate the fluid friction resulted from viscosity have become the major factor that limits the performance of the system.

Figure 4.39 shows the pressure and load displacement at 100 Hz under 130 V excitation without load. Comparing the pressure of the new DSM 3-channel amplifier to the pressure plots in Figure 4.14 of the DSM 2 Level amplifier, the peak pressure is 930 psi which is far above the peak pressure of around 600 psi of the old setup. In fact, the same peak voltages of 130 V are used and same pre-pressure is applied in both setups. The same procedure is used to remove the air inside of the chamber before the fluid is pressurized which means the same effective bulk modulus of the fluid. We think this difference might be contributed to the dynamics of the fluid itself. For the amplifier used in the single-ended setup, the output of the signal of is not fast enough to excite the dynamics of the fluid while for the DSM 3-channel power supply, it might be possible to excite the natural frequencies

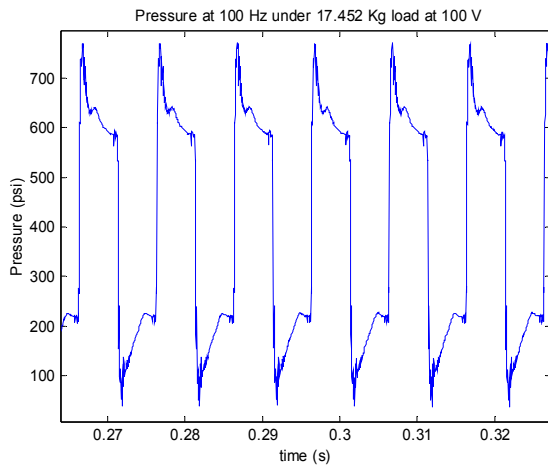


(a) Pressure

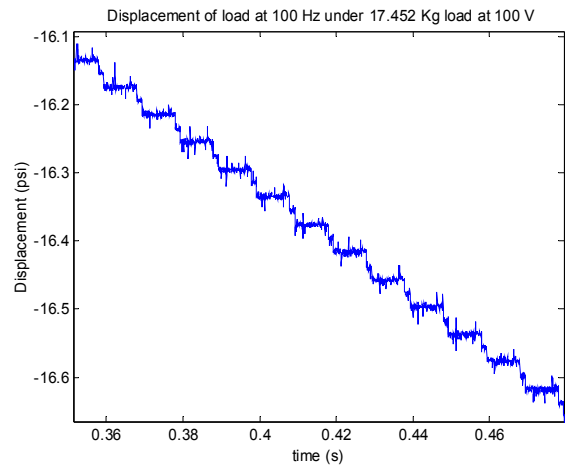


(b) Load displacement

Figure 4.35: Measurements at 100V peak voltage under no load at 100 Hz

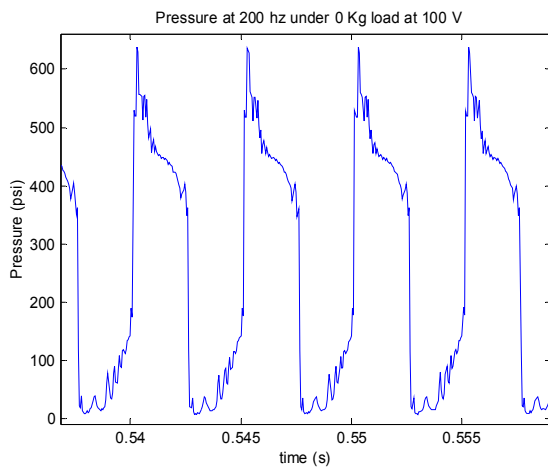


(a) Pressure

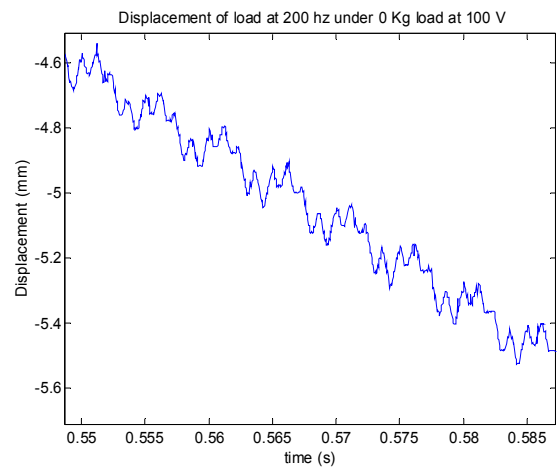


(b) Load displacement

Figure 4.36: Measurements at 100V peak voltage under 17.452 Kg load at 100 Hz

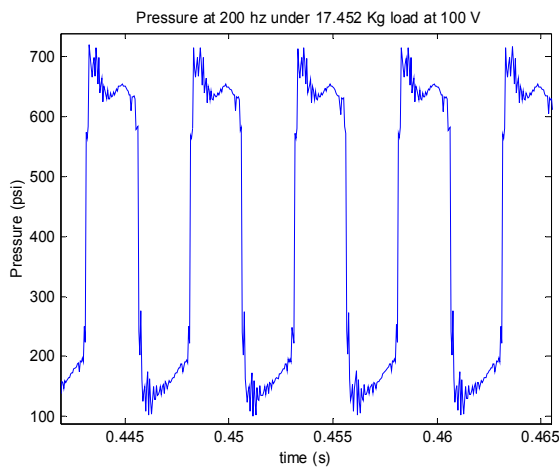


(a) Pressure

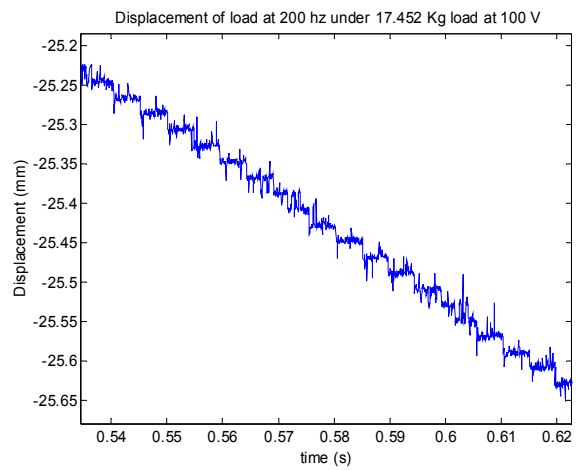


(b) Load displacement

Figure 4.37: Measurements at 100V peak voltage under no load at 200 Hz



(a) Pressure



(b) Load displacement

Figure 4.38: Measurements at 100V peak voltage under 17.452 Kg load at 200 Hz

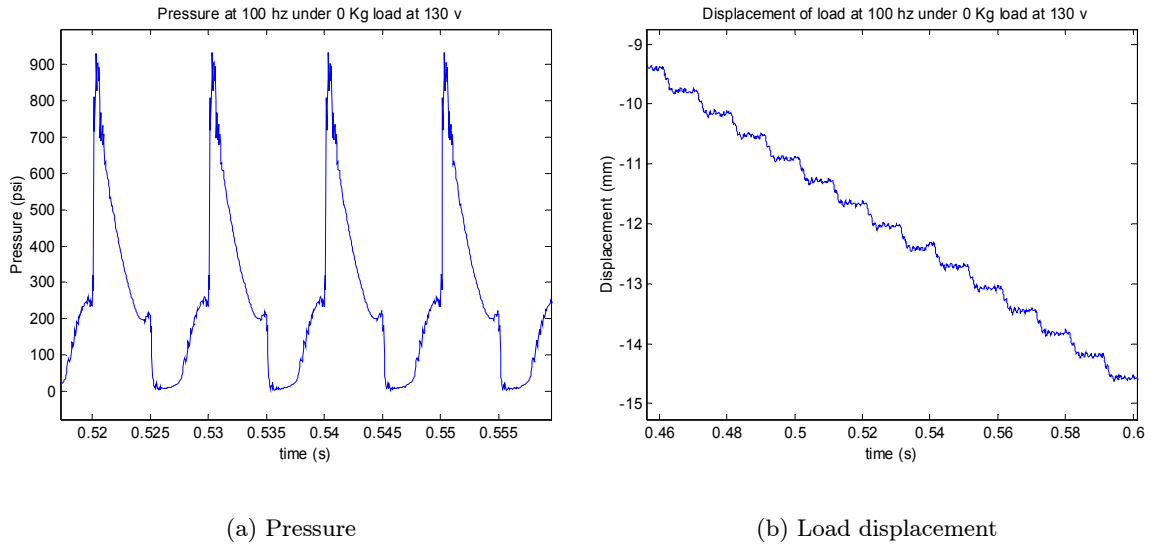


Figure 4.39: Measurements at 130V peak voltage under no load at 100 Hz

of the fluid system, and thus resulted in higher peak pressure than the results of the old slower power supply. Though from the above analysis, we know the response of the system shows some kind of dynamics, the operation frequency of 200 Hz is well below the critical frequency we computed in Chapter 3 at around 900 Hz. We will still use the steady state flow model to make simulations.

The simulation of velocity and power versus frequency at different loads are plotted in the following figures. Because the power output is equal to the velocity times with weight of load, thus the power has the same shape as the velocity curve under each load. Due to the hydraulic amplification mechanism of the active valves, we expect some delay might be introduced. In the simulations, a 0.4 ms valve transition is assumed. Figure 4.40 and Figure 4.41 compare respectively the velocities and power of the IVF, CVF models with experimental results at 100 V peak voltages. Figure 4.42 and Figure 4.43 compare respectively the velocities and power respectively the velocities and power of the IVF, CVF models with experimental results at 130 V peak voltages. In both cases, the CVF model consists with the experimental model better than IVF model. The performance of the system topped at about 140 Hz. Once again, we notice that under heavy load, the large difference exists between the model simulation and experimental results. We also attribute this discrepancy to the leakage problem that is not accounted in the model simulations.

We observed that as the load increases the IVF model overestimates the system

performance as it does in the single-ended cylinder setup, which can also be attributed to compressibility of fluid. Another observation is that the difference between the IVF and CVF becomes more obvious as frequency increases in each plot. The reason of this discrepancy is that CVF model assumes a linear bulk modulus to pressure model while the IVF model assumes an infinite modulus. As the frequency goes higher, because the fluid can not flow fast enough to fill the chamber to the pre-pressure, the stiffness of the fluid decreased due to reduce of bulk modulus. A lower stiffness of fluid results in lower dynamic pressure and smaller stroke of the load in one cycle. This effect ends up to a big difference between the IVF model and CVF model when the pump is operated at frequency near 200 Hz.

The maximum power of 130 V input voltage in Figure 4.43 is 3.6 W which is 1.63 times the maximum power of 100 V of 2.2 W shown in Figure 4.41. According to the IIF model, the power is proportional to the square stroke. In the case of 130 V, the stroke is about 1.3 times of the 100 V according to the constitutive equations of the piezoelectric stack. The ration of power of 1.63 is very close to the square of ratio of stroke 1.3, which indicate the IIF model is valid for basic performance estimations.

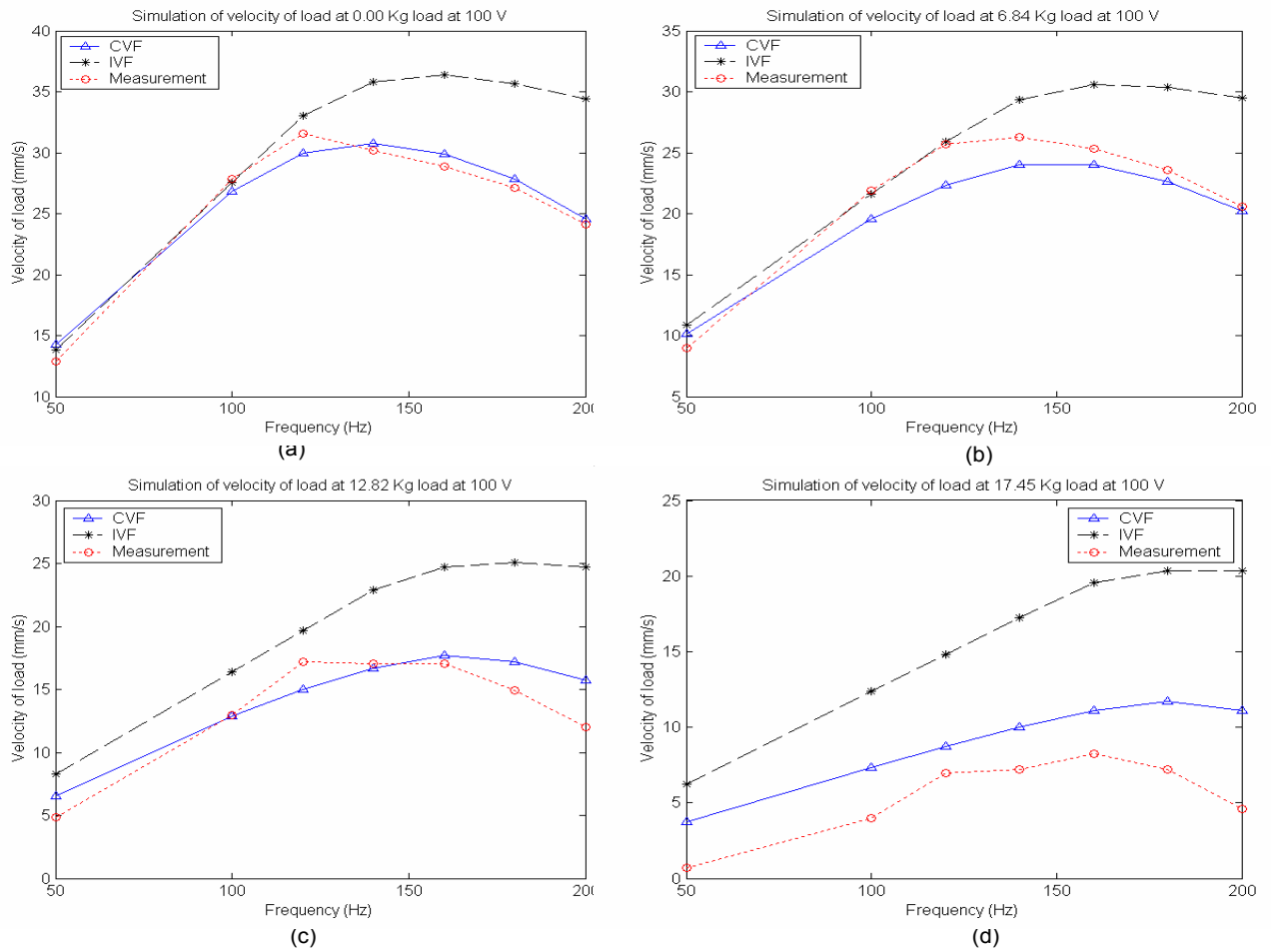
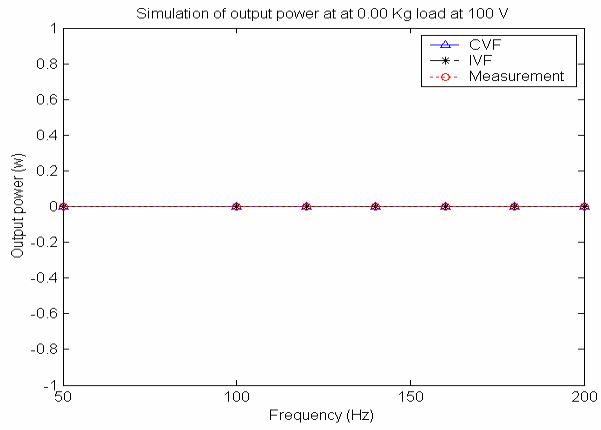
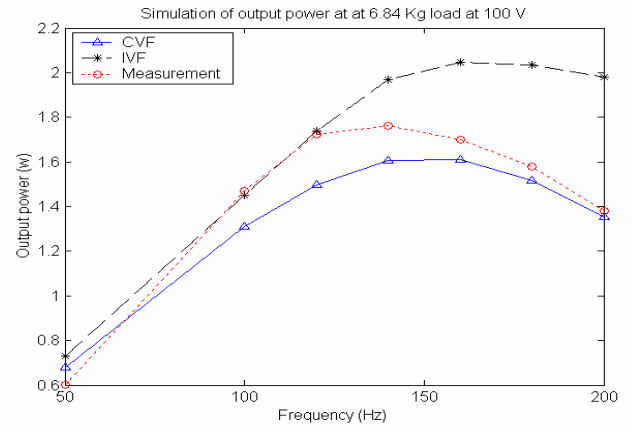


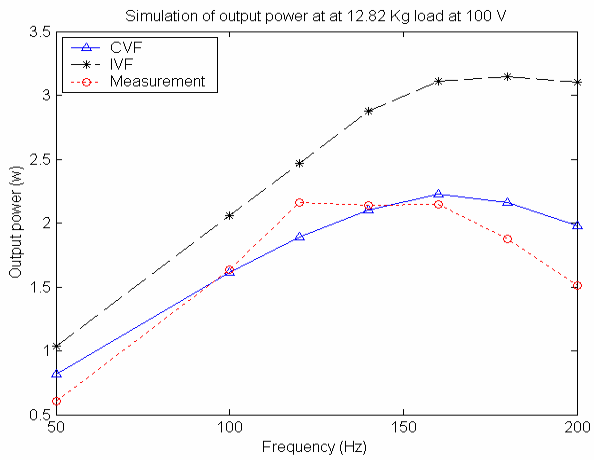
Figure 4.40: Velocity comparison at 100 V



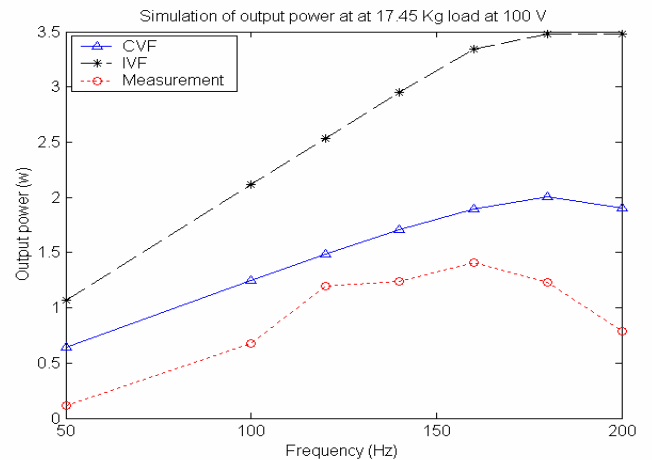
(a)



(b)



(c)



(d)

Figure 4.41: Power comparison at 100 V

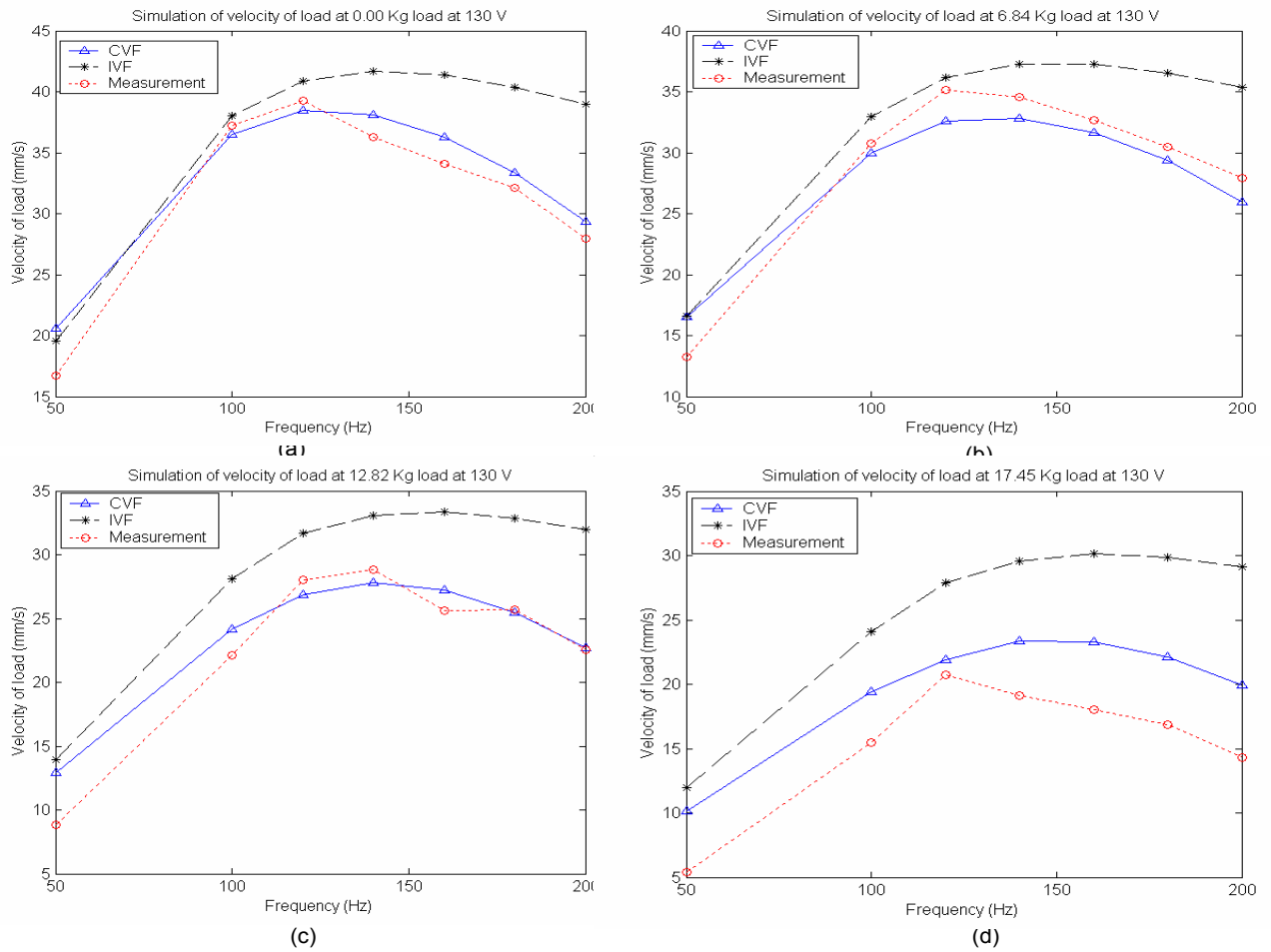


Figure 4.42: Velocity measurements at 130 V

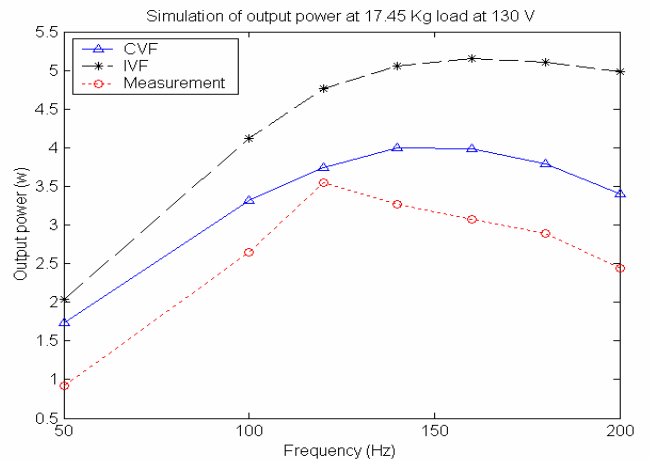
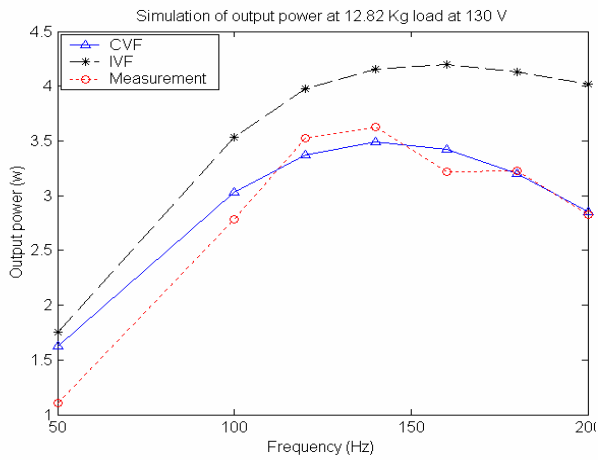
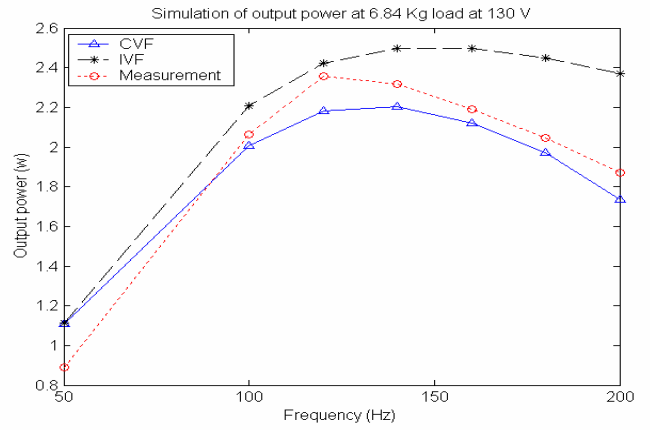
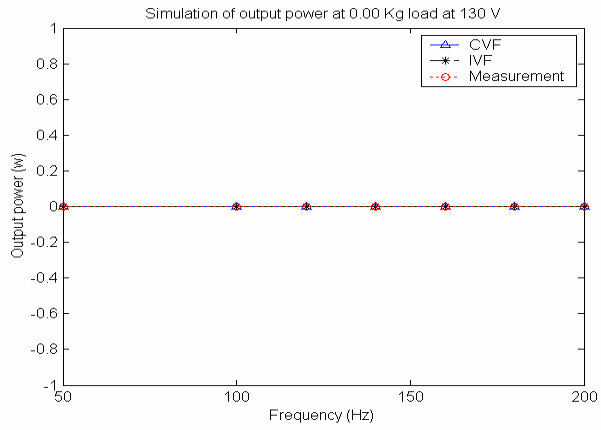


Figure 4.43: Power comparison at 130 V

4.7 Power Efficiency Analysis

4.7.1 Power Efficiency Measurements

Power of Single-ended Setup

The power efficiency tests are run in the single-ended cylinder setup. In order to explore the effect of load to the power and efficiency of the system, a lever which has an amplification factor of four is used to connect the load to the hydraulic cylinder. The use of lever enable us to measure the response of the system under heavy loads. The tests were run to up to 100 Hz due to the limit of the DSM 2 Level amplifier.

The output power of the system was obtained by measuring the velocity and weight of the load. We neglect the friction at the output cylinder and assume the load is zero if an external load was not added at the end of the cylinder. Figure 4.44 shows as load increases, the output mechanical power increases for each frequency.

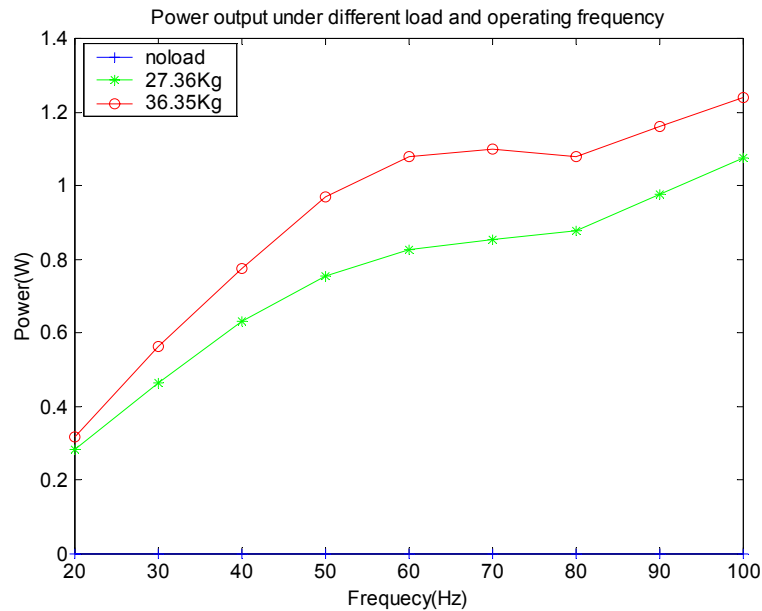
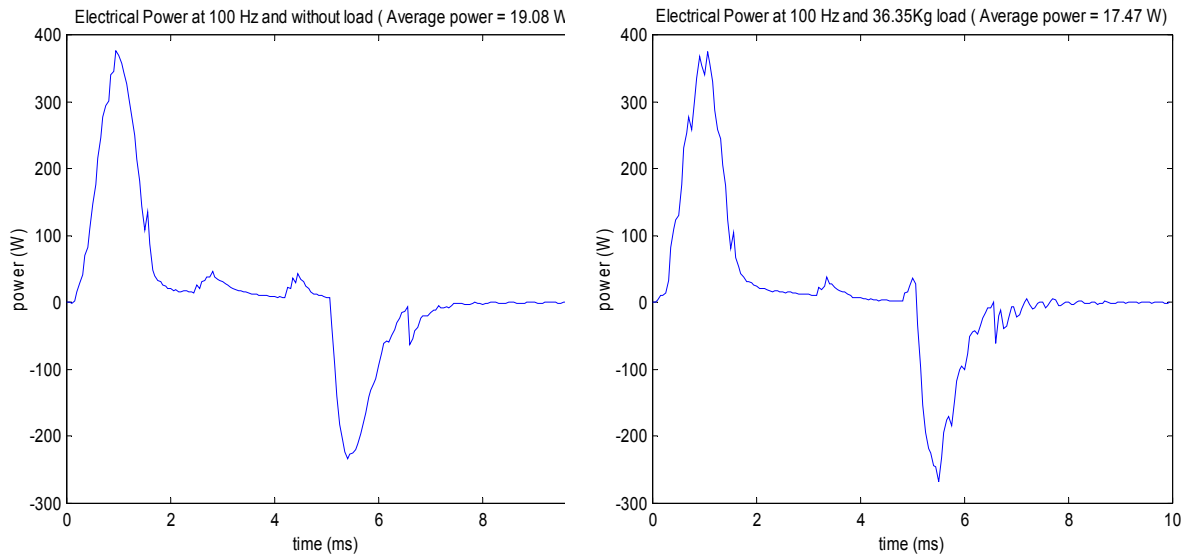


Figure 4.44: Output power at different operating frequency and load

Figure 4.45 shows the average electrical power in one period operated at 100 Hz. It is noticed there are two peaks at around 380 Watts. The positive one means the amplifier is providing power to piezoelectric materials while the other negative one indicates the electrical power is flowing back from piezoelectric materials to amplifier. The net power flowing into piezoceramics was 19.08 W without load and 17.47 W with 36.35 Kg load



(a) Electrical power without load

(b) Electrical power at load of 36.35 Kg

Figure 4.45: Electrical power under different load

respectively. The net power was only a small percentage of peak power.

Figure 4.46(a) shows the average voltage versus charge curve of piezoelectric materials in one cycle. By definition, the area encircled is the electrical work transferred to piezoelectric materials in each cycle. It is noticed that for the three different load, the voltage-charge curves are very similar, which indicate the output of the power amplifier is independent upon load. Figure 4.46(b) shows the filtered average resistance force acting against the piston versus the displacement of it in one cycle. The area encircled was the mechanical work transferred by the piston to hydraulic fluid in one cycle. It is noticed that as load increased, the peak force increased while the stroke of the piston decreased. Mechanical work done by the piston in one cycle decreased from 0.06514 J under no load to 0.046057 J under 36.35 Kg load. Based on the Figure 4.46(b), we believe there are two reasons. One is the maximum stroke decreased for heavy load, which resulted in less work. The other reason is that under heavy load, when the piston started to pull back, the force acting on the piston, which was proportional to the hydraulic pressure, was around 1100 N which is much higher than 400 N without load. It means that compared to the case of light load and no load, much more of the total work the piston transferred to the load was transferred back to the piston, which resulted in the net work the piezoelectric stack

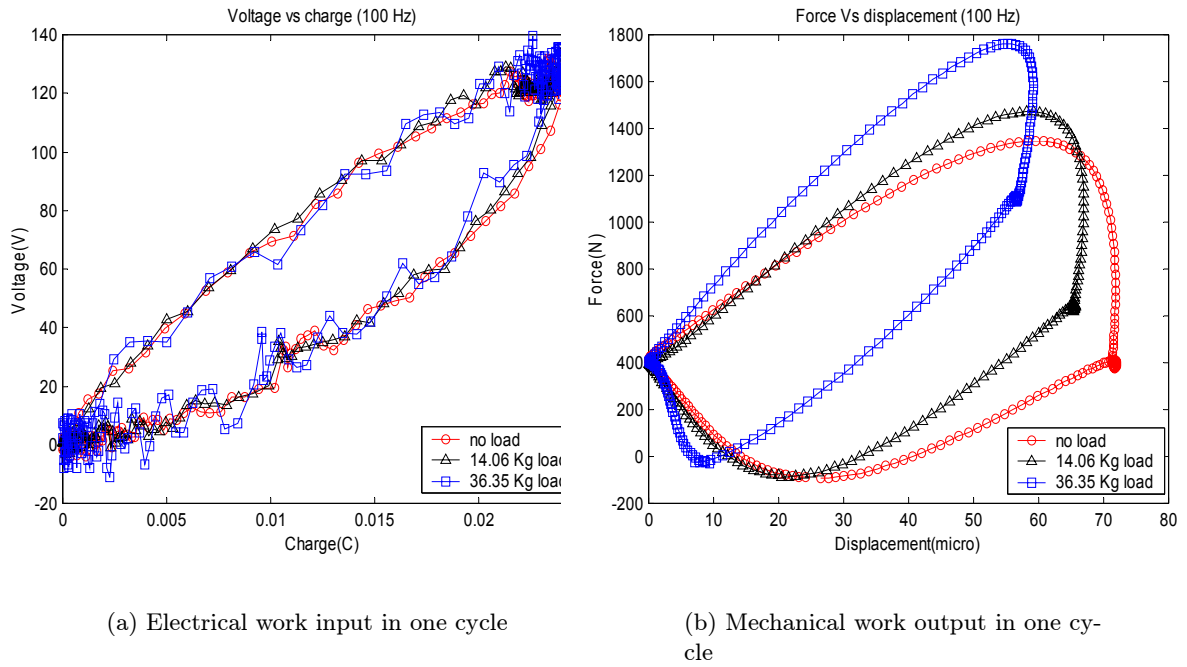


Figure 4.46: Electrical work and mechanical work without load and with light load

actuator transferred to the load decreased.

The efficiency of the piezoelectric materials was calculated by dividing the mechanical power done by piston, $Power_P$, by the electrical power, $Power_E$, into piezoelectric materials. The efficiency of hydraulic circuits was calculated by dividing the mechanical power of the piston, $Power_P$, by the mechanical power transferred to the load, $Power_L$. Table 4.1 shows the calculated efficiencies, where E_1 denotes the efficiency of piezoelectric materials, E_2 denotes the efficiency of the hydraulic circuits and E_{total} denotes the total efficiency of the actuation system, which is calculated by dividing the power transferred to the load with the electrical power. For zero load, the output power is zero and the resulted efficiencies E_2 and E_{total} are zero. It is noticed that the efficiency of the piezoelectric materials decreases from 34.1% under no load to 26.3% under 36.35 kg load. The efficiency of the hydraulic circuits increases from 11% under 14.06 kg load to 27.7% under 36.35 kg load. The increase of efficiency in the hydraulic circuits was more than decrease of efficiency at the piezoelectric stack actuator such that the total efficiency increased as load increased. We believe the improvement of the efficiency of the hydraulic circuits for the heavy load is because heavy load resulted in high pressure differential between the inlet and outlet of the

Table 4.1: Energy and actuation efficiency at 100 Hz operating frequency.

Load(Kg)	$Power_E$ (W)	$Power_P$ (W)	$Power_L$ (W)	E_1 (%)	E_2 (%)	E_{total} (%)
0	19.08	6.5134	0	34.1	0	0
14.06	19.19	5.8378	0.642	30.4	11.0	3.34
36.35	17.47	4.6057	1.274	26.4	27.7	7.31

hydraulic cylinder, which then would allow large flow rate through the hydraulic cylinder. On the other hand, a large pressure drop at the hydraulic cylinder will decrease the pressure differential at inlet and outlet active valves, which would result in flow rate decrease at valves. We expect an optimal load exists such that it maximizes the efficiency of the hydraulic circuits.

Power Measurements of Double-ended Setup

For the double-ended setup, the new DSM 3 channel power supply was used and it enabled to test above 100 Hz which was the limit of the old power supply. The tests were run up to 200 Hz under five different loads. Figure 4.47 and 4.48 respectively shows the output power at 100 V excitation and 130 V excitation. The maximum power is 2.2 W, which occurs at 120 Hz under 12.825 Kg load for 100 V and the maximum power is 3.65 W, which occurs at 140 Hz under 12.825 Kg load for 130 V excitation. We notice that increasing the frequency does not ensure increasing the performance. The explanation might be increasing the frequency might reduce the stroke of the load in each cycle and result in lower performance. We believe this reduce of the stroke may be contributed from the friction of the fluid, which keep the high pressure fluid from flowing from the chamber into the cylinder.

Figure 4.48 shows a maximum power at 100 Hz is 2.8W for double-ended cylinder at 130 V excitation, while for the single-ended one shown in Figure 4.44, the maximum power is 1.21 W at 100 Hz at 130 V excitation. It indicates the double-ended cylinder is superior to the single-ended one in terms of performance, which is predicted by the IIF model discussed in Chapter 3.

We also notice for the 130 V case, the performance under 20.153 Kg becomes irregular. In fact, we notice this happens some times under heavy load when the velocity becomes

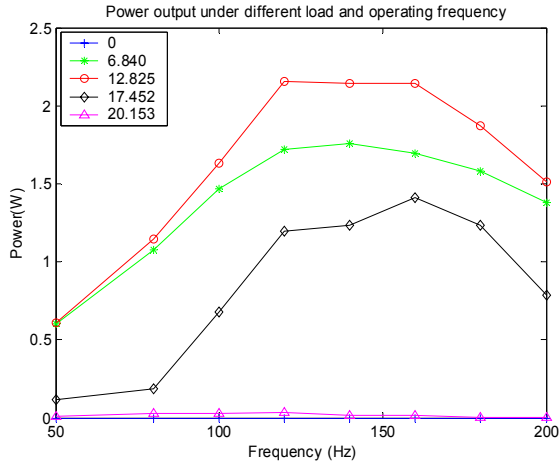


Figure 4.47: Power measurements at 100 V excitation

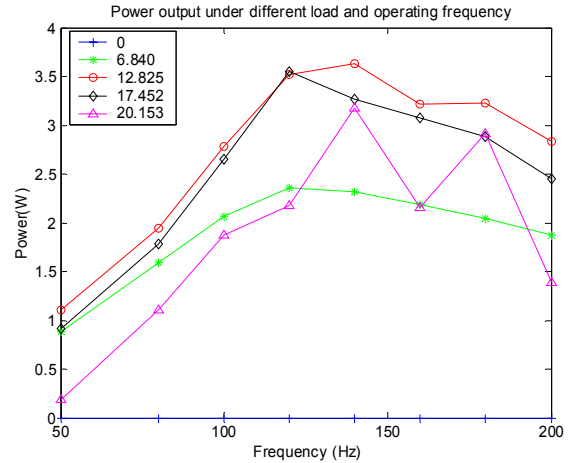


Figure 4.48: Power measurements at 130 V excitation

low. It indicates under heavy loads, the system performance is more sensitively dependent upon the initial conditions, such the pressure when we stop at the last test, the position of the piston in the hydraulic cylinder.

4.8 Summary

The experiment setup was presented. A linear bulk modulus model is presented and experimentally determined, which shows the bulk modulus is linearly dependent upon the pre-pressure of the fluid. The characteristics of both power supply are experimentally determined which will be incorporated into the model. The measurements and results are showed and compared with both the IVF and CVF models. The results indicate the CVF model is superior to the IVF model which assumes an incompressible fluid. The CVF model is consistent with experimental data for loads up to 15 Kg. Above that limit, the performance of system drops very sharply, which we believe can be contributed for leakage of the valves.

Chapter 5

Conclusions

Two setups with single-ended cylinder and double-ended cylinder are developed and tested. First a quasi-static model (IIF) that does not account for viscosity and compressibility is presented. Then a better model (IVF) assumes an incompressible viscous flow is presented. The CVF model that takes into account both the viscosity and compressibility is introduced. Finally the simulations of the IVF and CVF model are compared with the experimental results. From the analysis presented in this thesis, the following conclusions are made:

- The CVF model is more accurate than the IVF model, and it is a good approximation of the piezohydraulic actuation system.
- The compressibility of fluid is important to the system performance.
- The viscosity of the fluid which results in the friction loss is vital to the performance of the system. Less viscosity will allow faster fluid flow and will thus increase the power output at higher operation frequency.
- The system performance is also dependent on bulk modulus of the fluid, the transition of the valves and timing of the valves.
- The double-ended cylinder produces higher power than the single-ended cylinder.

Furthermore, in a brief summary of the most important aspects it can be stated :

- The electromechanical coupling of piezoceramics is modeled by two equations that consist of four variables: voltage, charge, force, and displacement. For a current con-

trolled stack, these two equations can be used to determine the force and displacement when voltage and current signals are given.

- For the hydraulic unit, the laminar flow characteristics is determined by computing the Reynolds number of the system. Energy equations for a control volume of viscous flow is derived and section velocity, head losses are determined for both laminar and turbulent flow.
- A four stage operation model is presented based on the timing of the stack actuator and inlet, outlet active valves. The status of valves and stack is defined in each stage, which will be used for simulation models.
- A quasi-static viscous flow model is presented. By assuming an inviscid and incompressible flow, it omits the complex numerical computation and can give simple analytical solution of the system performance. The results indicate that the pre-pressure reduce the maximum achievable power. It also indicates in terms of power and efficiency, the double-ended cylinder is superior to the single-ended cylinder.
- The CVF model which assumes an incompressible and viscous flow is developed based on the four stage operation model. The equations of each stage are derived separately. The equations of the model ends up to be two first order differential equations, which are simple for numerical simulations. Numerical simulations are then computed at each stages by setting the initial states to be the final states of the previous stage.
- The CVF model involves more computation effort by taking account into both compressibility and viscosity. Further assumptions and approximations are made to maintain simplicity. The acceleration of the load is neglected and the frictions in large volumes are also neglected. The CVF model involves two coupled first order differential equations which can be solved numerically.
- Simulation parameters are determined experimentally. A linear bulk modulus to pressure model is adopted and experimentally verified by conducting closed chamber tests. The results show that as pre-pressure increases, the stiffness of the fluid increases, which indicate a higher effective bulk modulus. Because the current and voltage is dependent on the specific power amplifier, both the DSM 2 Level power supply and DSM 3 Channel power supply are tested and characteristics of output are determined.

- The experimental results are compared with simulation results of both IVF and CVF model. The CVF model is a better of approximation than the IVF model under different loads. The experimental results show steep performance decreases and obvious reverse movement of load as load increases above 15 Kg, which we believe can be attributed to the leakage problem of the active valves. Under a certain frequency, the simulated velocity is very close to a line for different loads, but the slope of CVF is larger than the IVF model, which can be explained by the compressibility of the fluid.
- The power and efficiency measurements show the setup with the double-ended cylinder produces higher power than the single-ended one. The experimental results show the electrical efficiency decreases while the mechanical efficiency increases as the load increases. The total efficiency, though less than 10%, increases as load increases.

5.1 recommendation and Future Work

- The current system produces a maximum power of 3.6W at 140 Hz under 12.8 Kg load. Frictions should be minimized in order to produce more power at higher frequency. Larger size of piping, less connections and lower fluid viscosity may be options for the next generation of piezohydraulic pump.
- To avoid complex computations, we assume a steady fully-developed flow in the system. As the test frequency increases, this assumption may become inadequate for prediction of system performance. A lumped dynamic model or a finite element model might be favorable.
- The performance of the system is highly dependent upon the timing. Timing effect may be investigated and simulated in order to determine the optimal timing conditions.
- To achieve higher performance, a larger stack with longer stroke and larger stiffness may be incorporated in the design. Because operating in high frequency can generate larger heat which is harmful to the performance of piezoceramic materials, thermal analysis must be conducted before going to high frequency.

- The performance of system is also dependent upon the effective bulk modulus of the fluid. To increase the bulk modulus of fluid, which will improve for high frequency operation, other options that can generate better vacuum might be favorable.
- To increase the equivalent stiffness of system, the O-ring currently in the pumping chamber can be moved to seal at the interface of the piston and pumping chamber.

Appendix A

Partial Matlab .m File of the Model Simulation

The Matlab codes were developed in a modular fashion. Two major function, *simulate_IVF* and *simulate_CVF*, are the simulation of IVF model and CVF model respectively. The current and voltage characteristics of the power supply which determined experimentally are used as excitations to the stack. Then the problem begins to simulate in a four stage fashion under the know excitation. The chamber pressure denoted by P in the code, piston displacement by x and cylinder displacement by xL are simulated, upon which the velocity and power can be computed.

Code of CVF model:

```
%%%%%%%%%%%%%%%%%%%%%%%%%%%%%%%%%%%%%%%%%%%%%%%%%%%%%%%%%%%%%%%%%%%%%%%%%%
%% this function is the code for simulation of CVF model           %%
%% input:                                                         %%
%%          G---Load (N)                                           %%
%%          Freq---Frequency (Hz)                                  %%
%%          Sfree---strok under prepressure (m)                   %%
%% output:                                                         %%
%%          stroke---stroke of load in one cylce                 %%
%% important variables:                                           %%
%%          P---Pressure in chamber (Pa)                          %%
%%          x---Displacement of stack (m)                          %%
%%          xL---Displacement of load (m)                          %%
%%%%%%%%%%%%%%%%%%%%%%%%%%%%%%%%%%%%%%%%%%%%%%%%%%%%%%%%%%%%%%%%%%%%%%%%%%
function stroke = simulate_CVF(G, Freq, Sfree)

Ro = 900;                                                         %% density of fluid

Pacc = 210*6896;                                                 %% pressure of accumulator
beta0 = (Pacc*48.4+15356)*6896; %% the bulk modulus linear model
```



```

Ac = pi*0.0125^2;          %% Chamber Area
Ach = Ac;
VO = Ac * 0.002;          %% initial fluid volume

Ap = pi * 0.00075^2;      %% Area of pipe
Acy = pi * (0.0254/4)^2*3/4; %% Area of cylinder
Volt_max = 100;          %% maximum voltage output of amplifier (V)
I_max =8.2;              %% maximum current output of amplifier (A)

Cstack = 43e-6;          %% capacity of stack (F)
Xv = Sfree/Volt_max;
Kstack = 30e6;           %% stiffness of stack (N/m)
Ka = Kstack;
alfa = 1;                %% area ratio of single direction cylinder

Sfree = Sfree + Pacc * Ach / Kstack; %% compute the stroke at no prepressure

lamda = Ac/Acy * alfa;
ephpsilon = Ac/Ap;

valveOffset = 0.05;      %% inlet valve timing
stackDutyCycle = 0.5;    %% assume valve maintain open until
%% stack change direction

TotalPoints = 10000;     %% total simulation points in one period

t_rise = Volt_max/(I_max/Cstack);
Vt = Volt_max/t_rise;
t_period = 1/Freq,
tVector = linspace(0,t_period,TotalPoints);

%% begin iterations, initialization
P(1) = Pacc; x(1) = 0; T(1) = 0; xL(1) = 0;
Inum = 0;                %% number of iterations

Pstart = P(1);
Pend = 2*P(1);

```

```

%% loop of simulation until the pressure difference is less than 1%
while abs((Pend-Pstart)/Pstart) > 1e-2

    beta = beta0 + (P(length(P))-Pacc)*48.4;
    Inum = Inum + 1

%% compression

N1 = 10;          %% number of data points in this stage

P0 = P(length(P));
x0 = x(length(x));
xL0 = xL(length(xL));
xmax = Sfree - P0 * Ach / Kstack;
Xv = (Sfree - P0 * Ach / Kstack) / Volt_max;
deltat = Volt_max * Cstack / I_max;
t1 = linspace(0, deltat, 20);
V = t1 * I_max / Cstack;

P1 = P0 + beta * Ach / (V0-x0*Ach)*Xv * V /
    (1+ beta * Ach / (V0-x0*Ach) * Ach / Kstack);
x1 = (P1 - P0) / (beta * Ach / (V0-x0*Ach)) + x0;
Vcylinder1 = zeros(1,length(t1));
xL1 = xL(length(xL))*ones(1,length(t1));
t1 = T(length(T))+t1;

P = [P P1];
T = [T t1];
x = [x x1];
xL = [xL xL1];

%% reset loop conditions
Pstart = Pend
Pend = P1(length(P1))

%% exhaust stage

KLev = 1; KLv = 10; KLec = 1; KLp = 10; %% minor loss and major loss

```

```

KL = KLev + KLv + 2*KLec + KLp;    %% total losses factor
%%%%%%%%%%%%%%%%%%%%%%%%%%%%%%%%%%%%%%%%
t2b = T(length(T));
options = odeset('RelTol',1e-6,'AbsTol',[1e-9]);
V_max = Volt_max;
Ach = Ac;
GL = G;
L0 = V0/Ach;
rho = Ro;
Vdelay = 0.0005*Freq/100;
[T2,Y]=ode45(@Simdiff_loop_exhaustion,[0 (stackDutyCycle+Inum-1)/
    Freq-t2b-Vdelay], [x(length(x)) 0],options,Ka, Xv, V_max, Pacc,
    Ach, GL, lamda, alfa, rho, beta, L0, KL, ephsilon);
L2 = length(T2);
xP = real(Y(:,1));
xL2 = real(Y(:,2));
P2 = P(length(P)) - (xP - x(length(x)))*Ka/Ach;

stroke = max(xL2)-min(xL2);        %% stroke of load in one cycle
Velocity = stroke * Freq;          %% velocity for possible return
Power = Velocity *GL;              %% power for possible return

T2 = T2 + t2b + Vdelay;
T = [T T2'];
x = [x xP'];
P = [P P2'];
xL = [ xL xL(length(xL))+xL2'];

%%%%%%%%%%%%%%%%%%%%%%%%%%%%%%%%%%%%%%%% expansion stage

t3 = linspace(0, deltat, 100);
V = t3 * I_max /Cstack;
xe = real(x(length(x)));
Pe = real(P(length(P)));
beta = real(beta);
x = real (x);
P = real (P);
Xv = real (Xv);
x3 = xe- Xv*Vt/(1+Ach*beta/(Kstack*(V0/Ach-xe))) * t3 ;

```

```

P3 = Pe + beta * (x3 - xe)/(V0/Ach-xe);
Pmin = min(P3);

x = [ x x3];
P = [ P P3];
T = [T T(length(T))+t3];
xL = [xL xL(length(xL))*ones(1,length(x3))];

%%%%%% intake stage

x0 = x(length(x))
P0 = Pmin
options = odeset('RelTol',1e-5);
KL = 1e-5;
[T4,Y]=ode45(@Simdiff_loop_intake,[T(length(T)) Inum /Freq],
    P0,options,Ka, Xv, V_max, Pacc, Ach, GL, lamda, alfa, rho,
    beta, L0, KL, ephsilon);
P4 = Y(:,1);
x4 = -(P4-Pacc)*Ach/Ka ;
P = [P P4'];
x = [x x4'];
T = [T T4'];
xL = [xL ones(1,length(T4))*xL(length(xL))];
P = clear_negative(P);
Lastcycleat(Inum) = length(T);

end

```

Code of IVF model:

```

%%%%%%%%%%%%%%%%%%%%%%%%%%%%%%%%%%%%%%%%%%%%%%%%%%%%%%%%%%%%%%%%%%%%%%%%
%% this function is the code for simulation of CVF model           %%
%% input:                                                         %%
%%          G---Load (N)                                         %%
%%          Freq---Frequency (Hz)                               %%
%%          Sfree---strok under prepressure (m)                %%
%% output:                                                         %%
%%          stroke---stroke of load in one cylce               %%
%% important variables:                                           %%
%%          P---Pressure in chamber (Pa)                       %%
%%          x---Displacement of stack (m)                      %%
%%          xL---Displacement of load (m)                      %%
%%%%%%%%%%%%%%%%%%%%%%%%%%%%%%%%%%%%%%%%%%%%%%%%%%%%%%%%%%%%%%%%%%%%%%%%

```

```

function Stroke = simulate_IVF(G,Freq,Sfree)

Ro = 900    %% density of fluid
Kstack = 30e6; %% stack siffness
beta = (Pacc*48.4+15356)*6896; %% bulk modulus (psi)
Ac = pi*0.0125^2; %% Chamber Area
V0 = Ac * 0.002; %% initial fluid volume
Pacc = 210*6896    %% pressure of accumulator
Ap = pi * 0.00075^2 %% Area of pipe
Acy = pi * (0.0254/4)^2*3/4 %% Area of cylinder
Volt_max = 130; %% maximum voltage output of amplifier
I_max = 8.2; %% maximum current output of amplifier
Cstack = 43e-6; %% capacity of stack (F)
Xv = Sfree/Volt_max;
alfa = 1; %% area ratio of cylinder
valveOffset = 0.05; %% outlet valve timing
stackDutyCycle = 0.5; %% stack duty cylce

TotalPoints = 2000; %% total simulation points in one period
t_rise = Volt_max/(I_max/Cstack);
Vt = Volt_max/t_rise;
t_period = 1/Freq,
tVector = linspace(0,t_period>TotalPoints);
PRatio = 10; %% pressure ratio, no pressure control
Ptr = (Pacc+G/Acy) * alfa * PRatio; %% valve open at (Pacc+G/Acy)

%%%%%% compression

PointsNumber = floor(t_rise/t_period*TotalPoints);

t1 = tVector(1:PointsNumber);
P1 = Pacc + beta*Ac/V0*Xv*Vt*t1 / (1+beta*Ac^2/V0/Kstack);
SLope = beta*Ac/V0*Xv*Vt

x1 = Xv*Vt*t1 - Ac/Kstack*(P1 - Pacc);
NoPowerFlag = 0;

```

```

i=1; Flag = 0;NewNum = 0;
while i<length(P1)& Flag == 0
    if(P1(i)>Ptr)
        NewNum = i;
        Flag =1;
        disp('FOUND')
    end
    i=i+1;
end

if (Flag == 0)
    disp('mximum pressure exceeded');
    NewNum = length(P1);
    Ptr = max(P1);

    if max(P1) < (Pacc+G/Acy) * alfa
        NoPowerFlag = 1;
    end
end

disp('#####');

if (NoPowerFlag == 0)
P = P1(1:NewNum);
t = t1(1:NewNum);
x = x1(1:NewNum);
Vcylinder = zeros(1,NewNum);

%%%%%% exhaust

KLev = 1; KLv = 10; KLec = 1; KLp = 10; %% minor loss and major loss
KL = KLev + KLv + 2*KLec + KLp; %% total loss factor

VoltEnd = Volt_max;
C_ETA = (Pacc + G/Acy)*alfa
C_ZETA = Ap*Kstack*sqrt(2/(Ro*KL))/Ac^2
C_SIGMA = Xv*Kstack/(Cstack*Ac)
save DataFile C_ETA C_ZETA C_SIGMA

NFlag = 0;

```

```

if Ptr < max(P1)

t0 = t(length(t)); P0 = P(length(P)); x0 = x(length(x));
I = sqrt(P0-C_ETA)*C_ZETA/C_SIGMA
Volt_0 = I_max*t0/Cstack

t1 = min((Volt_max-Volt_0)*Cstack/I, stackDutyCycle/Freq-t0)
VoltEnd = Volt_0 + t1*I/Cstack; %% voltage at the end of exhaustion

if (Volt_max-Volt_0)*Cstack/I < stackDutyCycle/Freq-t0
    NFlag = 1; %% enough time
end

PointsNum = 1000;
tVector = linspace(t0,t0+t1,PointsNum );
PVector = P0*ones(1,PointsNum );
xVector = x0+Xv/Cstack*I*(tVector-t0) ;
Vcylinder2 = Xv*I/Cstack*Ac/(Acy/alfa)*ones(1, PointsNum );

P = [P PVector ];
t = [t tVector ];
x = [x xVector ];
Vcylinder = [Vcylinder Vcylinder2 ];

else
    NFlag = 1;
end

%% exhaust continue

if NFlag == 1
lt = length(t)
t0 = t(length(t)); P0 = P(length(P));
t1 = stackDutyCycle/Freq;

SimNum = 1000;
tVector = linspace(t0,t1,SimNum);
[PVector, PdotVector] = Heun_solver(tVector,P0,C_ZETA,C_ETA);

```

```

xVector = Xv*Volt_max-Ac/Kstack*(PVector -Pacc);

Vcylinder3 = -Ac/Kstack*PdotVector*Ac/Acy*alfa;

P = [P abs(PVector)];
t = [t tVector ];
x = [x abs(xVector) ];
Vcylinder = [Vcylinder Vcylinder3];
end

x3e = x(length(x));
t3e = t(length(t));
P3e = P(length(P));

if Flag == 1
    Volt_0 = Volt_max;
else
    Volt_0 = VoltEnd;
end

t4e = Volt_0/(I_max/Cstack)

PointsNumber4 = floor((t4e)*Freq*TotalPoints)

t4Vector = linspace(0,t4e,PointsNumber4 );
x4 = x3e - Xv*Vt/(1+Ac*beta/(Kstack*(V0/Ac-x3e))) * t4Vector ;
P4 = P3e + beta * (x4 - x3e)/(V0/Ac-x3e);

t4e = t4e + t3e;
t4Vector = t4Vector + t3e;
P4e = P4(length(P4));
x4e = x4(length(x4));

t = [t t4Vector ];
P = [P P4];

x = [x x4];
F = P * Ac;
Vcylinder4 = zeros(1,PointsNumber4 );

```



```

Vcylinder = [Vcylinder Vcylinder4 ];

%%%%%%%% intake

KLp = 20; KLv = 10;
KL = KLp + KLv;
KL = 10 * KL

C_ZETA = Ap*Kstack/Ac^2*sqrt(2/(Ro*KL));
txTr = 2*sqrt(Pacc-P4e)/C_ZETA

if txTr+t4e < 1/Freq

PointsNumber5 = floor((txTr)*Freq*TotalPoints)
t5Vector = linspace(0,txTr,PointsNumber5);
P5 = Pacc-(-C_ZETA*t5Vector/2+sqrt(Pacc-P4e)).^2;
x5 = Ac/Kstack*(P4e-P5)+x4e;
t5Vector = t5Vector + t4e;
t = [t t5Vector ];
P = [P P5];
x = [x x5];
F = P * Ac;

Vcylinder5 = zeros(1,PointsNumber5 );
Vcylinder = [Vcylinder Vcylinder5 ];

x5e = x(length(x));
P5e = P(length(P));
t5e = t(length(t))

PointsNumber6 = floor((1-t5e*Freq)*TotalPoints)
if (PointsNumber6 > 1)
t6Vector = linspace(t5e,1/Freq,PointsNumber6);

P6 = P5e*ones(1,PointsNumber6 );
x6 = x5e*ones(1,PointsNumber6 );

t = [t t6Vector ];
P = [P P6];

```

```

P = clear_negative(P);
x = [x x6];
F = P * Ac;

Vcylinder6 = zeros(1,PointsNumber6 );
Vcylinder = [Vcylinder Vcylinder6 ];
end

else
    PointsNumber5 = floor((1/Freq-t(length(t)))*TotalPoints)
t5Vector = linspace(0,1/Freq-t(length(t)),PointsNumber5);
P5 = Pacc-(-C_ZETA*t5Vector/2+sqrt(Pacc-P4e)).^2;
x5 = Ac/Kstack*(P4e-P5)+x4e;
t5Vector = t5Vector + t4e;
t = [t t5Vector ];
P = [P P5];
x = [x x5];
F = P * Ac;
    Vcylinder5 = zeros(1,PointsNumber5 );
    Vcylinder = [Vcylinder Vcylinder5 ];
end

Dcylinder = cumtrapz(t,Vcylinder );
TotalPointNum = length(t);

else
    N = length(P1);
    t = linspace(0,1/Freq,N);
    P = zeros(1,N);
    x = zeros(1,N);
    F = zeros(1,N);
    Dcylinder = zeros(1,N);
    TotalPointNum = length(t);
end

P = clear_negative(P);
F = clear_negative(F);

```

Functions that are called by the above *simulate_IVF* and *simulate_CVF* function:

```
%%% ODE solver called by function simulate_IVF
```

```

function [P,Pdot] = Heun_solver(t,P0,C_ZETA,C_ETA)
N = length(t);
h = (max(t)-min(t))/N;
P(1) = P0;
Pdot(1) = f(P0,C_ZETA,C_ETA);
for i = 1:N-1
    P(i+1)= P(i)+h/2*(f(P(i),C_ZETA,C_ETA)+f(P(i)+h*f(P(i),C_ZETA,C_ETA),C_ZETA,C_ETA));
    Pdot(i+1)= f(P(i+1),C_ZETA,C_ETA);
end

%%% Function called by function Heun_solver
function y = f(y0,C_ZETA,C_ETA)
y = -C_ZETA*sqrt(y0-C_ETA);
end

%%% Function that clear negative pressure
function ynew = clear_negative(y)
for i = 1: length(y)
    if y(i) < 0
        ynew(i) = -0.01;
    else
        ynew(i) = y(i);
    end
end
end

```

Bibliography

ANSI/IEEE Standard 176, *IEEE Standard on Piezoelectricity*, **Standards Committee of the IEEE Ultrasonics, Ferroelectrics, and Frequency Control Society**, 1987.

Bexell, M., Tiensuu, A. L., Schweitz, J. A., Soderkvist, J., and Johansson, S., *Characterization of an inchworm prototype motor.*, **Sensors and Actuators**, Vol. A, No. 43, pp. 322–329, 1994.

Doebelin, E., **System Dynamics Modeling and Response**, Bell & Howell Company, Columbus, Ohio, 1972.

Fox, R. and McDonald, A., **Introduction to Fluid Mechanics**, Second Edition, John Wiley & Sons, Inc., 1978.

Gerlach, T. and Wurmus, H., *Working principle and performance of the dynamic micropump*, *Sensors and Actuators.*, **Sensors and Actuators**, Vol. A, No. 60, pp. 135–140, 1995.

Gilles Robert, D. D. and Setter, N., *Separation of Nonlinear and Friction-like Contributions to the Piezoelectric Hysteresis.*, **IEEE Internatinal Symposium on Applications of Ferroelectrics**, Vol. 2, pp. 699–702, 2002.

Giurgiutiu, V., Chaudhry, Z., and Rog, C. A., *Stiffness Issues in the Design of ISA Displacement Amplification Devices: Case Study of a Hydraulic Displacement Amplifier.*, **SPIE**, Vol. 2443, pp. 844–852, 1994.

Giurgiutiu, V. and Rogers, C. A., *Power and Energy Characteristics of SolidoState Induced-Strain Actuators for Static and Dynamic Applicatioins.*, **Journal of Intelligent Material Systems and Structures**, Vol. 8, pp. 738–750, Sep. 1997.

- Kar, S., McWhorter, S., Ford, S. M., and Soper, S. A., *Piezoelectric mechanical pump with nanoliter per minute pulse-free flow delivery for pressure pumping in micro-channels.*, **Analyst**, Vol. 123, pp. 1435–1441, 1998.
- Manring, N. D., *The Effective Fluid Bulk-Modulus within a Hydrostatic Transmission.*, **ASME**, Vol. 119, pp. 462–466, 1997.
- Mauck, L. and Lynch, C. S., *Piezoelectric Hydraulic Pump.*, **SPIE**, Vol. 3668, pp. 844–852, 1999.
- Mitrovic, M., Carman, G. P., and Straub, F. K., *Electro-Mechanical Characterization of Piezoelectric Stack Actuators.*, **SPIE**, Vol. 3668, pp. 844–852, 1994.
- Munson, B. and Young, D., **Fundamentals of Fluid Mechanics**, Third Edition, John Wiley & Sons, Inc., 1998.
- Nasser, K. and Leo, D. J., *Compact Piezohydraulic Actuation System.*, **SPIE**, Vol. 3991, 2000a.
- Nasser, K. and Leo, D. J., *Efficiency of Frequency-Rectified Piezohydraulic and Piezopneumatic Actuation.*, **Journal of Intelligent Material Systems and Structures**, Vol. 11, No. 10, pp. 798–810, 2000b.
- Near, C. D., *Piezoelectric Actuator Technology.*, **SPIE**, Vol. 2717, pp. 246–258, 1996.
- Paine, J. S. and Chaudhry, Z., *The Impact of Amplification on Efficiency and Energy Density of Induced Strain Actuators.*, **ASME Aerospace Division**, Vol. AD, No. 52, pp. 511–516, 1996.
- R. H. Sabersky, A.J. Acosta, E. H. and Gates, E., **Fluid Flow**, Fourth Edition, Prentice-Hall, Inc., Upper Saddle River, New Jersey, 1999.
- Sirohi, J. and Chopra, I., *Design and Testing of a High Pumping Frequency Piezoelectric-Hydraulic Hybrid Actuator.*, **SPIE**, Vol. 4327, 2002.
- Smits, J. G., *Piezoelectric Micropump with Three Valves Working Peristaltically.*, **Sensors and Actuators**, Vol. A, No. 21-23, pp. 203–206, 1990.
- Tullis, J., **Hydraulics of Pipelines**, John Wiley & Sons, Inc., 1989.

White, F. M., **Fluid Mechanics**, Third Edition, McGRAW-HILL, Inc., 1994.

Wise, S. A., *Displacement properties of RAINBOW and THUNDER piezoelectric actuators.*, **Sensors and Actuators**, Vol. A, No. 69, pp. 33–38, 1998.

Vita

Honghui Tan, was born in October 18, 1975, in Pingxiang, China. He graduated from Pingxiang High School in July 1992. He enrolled in Tsinghua University later that August, and graduated in July 1997 with B.S. in Automotive Engineering. After graduation, he worked for the Sixth Institute of Electronic Department of China and Gaohong Telecommunications for a total of three years. He then enrolled in the MS program of Mechanical Engineering Department of Virginia Tech and work as graduate research assistant in CIMSS from August 2000, concentrating on piezoelectrics, hydraulics and controls.

Permanent Address: USA

This thesis was typeset with $\text{\LaTeX} 2_{\epsilon}$ ¹ by the author.

¹ $\text{\LaTeX} 2_{\epsilon}$ is an extension of \LaTeX . \LaTeX is a collection of macros for \TeX . \TeX is a trademark of the American Mathematical Society. The macros used in formatting this thesis were written by Greg Walker, Department of Mechanical Engineering, Virginia Tech.